2014-09-16

Kinematic forward modeling and interpretation of faults in 3D seismic reflection data

Alarfaj, Mohammed

UNIVERSITY OF CALGARY

Kinematic forward modeling and interpretation of faults in 3D seismic reflection data

by

Mohammed Alarfaj

A THESIS

SUBMITTED TO THE FACULTY OF GRADUATE STUDIES

IN PARTIAL FULFILMENT OF THE REQUIREMENTS FOR THE

DEGREE OF MASTER OF SCIENCE

GRADUATE PROGRAM IN GEOLOGY AND GEOPHYSICS

CALGARY, ALBERTA

MAY, 2014

Abstract

The geometry of an active fault onshore Taranaki Peninsula, New Zealand was evaluated from a 3D seismic reflection volume. The geologic history of Taranaki Basin explains the complex tectonic-related deformation in the subsurface. Interpretation of the studied 3D seismic volume shows clearly imaged normal faults dominating the shallow structure, faults at deep reflections are poorly imaged. Interpretation of the seismic data also reveals possible gas flow associated with permeable normal faults. Analysis of seismic attributes helps in detecting the gas presence along faults in the subsurface. Kinematic forward models were constructed in this study to predict the active fault geometry at depth where it may not be very visible. The models are based on concepts of extensional fault-bend folding and were constructed to resolve geometric ambiguities in the interpreted volume. The modeled major fault in this study has a flat-ramp-flat geometry which cuts through the basement at depth.

Acknowledgements

I would like to acknowledge my thesis advisor Dr. Don Lawton for his time, knowledge and support. I thank him for his guidance, encouragement and help. I greatly appreciate the opportunity of working with him on this research.

I would like to thank Saudi Aramco for the support provided during my work on this thesis. I also thank CREWES sponsors, professors, faculty staff and students for supporting this research. I appreciate Dr. Alan Nunn's help and consultation in using the modeling software provided to the University of Calgary by Nunns and Rogan LLC.

Most importantly, I thank my parents, family, and friends for their incredible love and support.

Dedication

To the loved ones: my parents, family and friends.

Table of Contents

List of Tables

List of Figures and Illustrations

Chapter One: Introduction

1.1 Overview

Exploration and development of hydrocarbons trapped in Earth require knowledge of the subsurface structure and stratigraphy. Interpretations of the 'unseen' subsurface are based on direct and indirect methods at different scales of investigation. Interpreters must then integrate different types of data (geophysical, geological, and petrophysical) to achieve a better model that estimates the subsurface geology. In geophysical prospecting, reflection seismology remains a primary tool for imaging and predicting the subsurface geology.

One of the main objectives of this thesis is to analyze and model faulting patterns from a seismic reflection volume in an extensional regime. This chapter introduces basic concepts of the seismic response of acoustic waves propagating through the subsurface as well as covers the outlines and objectives of this thesis.

1.2 Seismic Interpretation

Interpretation of seismic reflection data is a fundamental tool for finding and developing oil and gas prospects. Reflection seismology is an indirect measurement tool which provides meaningful information used to construct reliable models of the subsurface. Seismic interpretation is subject to the data quality which is significantly affected by the acquisition and processing parameters of the seismic survey.

Advancements and efforts in seismic data acquisition and processing are aimed to improve the quality and interpretability of seismic data. While seismic acquisition and processing are based on mathematical principles and handled mainly digitally, seismic interpretation remains primarily a visual process (e.g. based on intellectual correlation, pattern

recognition… etc), used to describe the subsurface geology and define the size and position of hydrocarbon targets (Herron, 2011).

Unlike acquisition and processing which are considered a forward process, seismic interpretation is considered an inverse process that can provide different explanations to a particular dataset (i.e. non-unique solutions) (Yilmaz, 2001; Herron, 2011). Therefore, seismic interpretation must be a model-driven process based on sound geologic principles.

A fundamental fact that has to be kept in an interpreter's mind is that seismic reflection data is an estimation of the subsurface, measured in two way travel time (TWT), and is not an exact representation of the true subsurface geology. The seismic response to the earth's layers and structure is constrained with limitations that should be addressed during the interpretation process.

1.2.1 Seismic Response

Seismic data is acquired when sensors detect the reflected sound waves (or echoes) generated from a seismic source (e.g. explosives or vibroseis). Sound waves propagate and spread out though the subsurface causing vibrations along rocks and fluids they pass through. When seismic waves encounter a geological boundary between two different earth's layers, some of the waves are reflected (i.e. travel back to the surface) and some are transmitted (i.e. continue to propagate further in earth).

Vibrations arriving to the sensors at the surface are detected and recorded as a function of time. The output result is the seismic trace, which typically consists of the time break at the initiation of the seismic source, then the first arrival or first break which is caused by waves propagating along the earth surface (e.g. not reflected), followed by reflections caused by the

11

acoustic waves bouncing off boundaries between different earth layers. The primary reflections in the seismic trace would ideally represent the Earth's layers in the subsurface. The strength of a reflected wave typically decreases with increasing time.

Geoscientists generally employ variables extracted from seismic data to describe different Earth properties. These variables are velocity (compressional Vp and shear Vs), density (ρ) and absorption (Q) (Yilmaz, 2001). Wave velocities determine the propagation paths and travel times. Velocities along with densities define the acoustic impedance in seismic data.

1.2.2 Seismic Attenuation

Frequencies in seismic data are subject to absorption due to the natural attenuation property of earth's materials (Yilmaz, 2001). This attenuation is frequency-dependent and mostly affects the high-frequency portion of the induced signal. The frequency absorption results in amplitude decay and decrease in the seismic signal strength with increasing depth (Yilmaz, 2001). With increasing travel-time (or depth), the absorption results in a decrease in the strength of the source signal and also in amplitude decay. This explains the time-variant nature of the seismic source wavelet, as its shape and bandwidth vary with time. In addition, acoustic velocities increase with depth and cause further amplitude decay as waves propagate through deeper earth layers. The frequency attenuation and amplitude decay significantly deteriorate seismic resolution of at depth.

1.2.3 Seismic Resolution

Resolution of seismic reflection data determines the ability to resolve or detect two separate reflecting points on a reflector (i.e. recognizing the two reflecting points as two instead of one). The minimum distance necessary to image two separate points defines seismic

resolution. This is related to the sampling rate of seismic data and affect both temporal and spatial limits.

The temporal resolution of seismic reflection data determines the minimum thickness required for a subsurface feature to be adequately imaged in the seismic data (Widess, 1973). The temporal resolution is controlled by the dominant wavelength (λ), which is determined by the wave velocity and dominant frequency (e.g. Yilmaz, 2001; Lines and Newrick, 2004):

$$\lambda = \frac{v}{f} \tag{1.1}$$

where v is wave velocity and f is the dominant frequency.

The dominant frequency is variable both vertically and laterally in seismic data. The minimum distance necessary for two reflecting points to be recognized in seismic imaging is about one-fourth of the dominant wavelength (λ/4) (e.g. Yilmaz, 2001; Lines and Newrick, 2004). This resolution limit means that an imaged fault (e.g. a reflector discontinuity) is only recognized when the fault's throw is equal to or greater than a quarter of the dominant wavelength (λ/4). The dominant frequency of acoustic waves traveling through the subsurface ranges from 20 to 50 Hz and typically decreases with increasing depth. In contrast, seismic velocities range from 2000 to 5000 m/s and generally increase as acoustic waves propagate deeper in the subsurface. Subsequently, the typical values of frequencies and velocities can be used to estimate the possible values of seismic wavelengths which range from 40 to 250 m. The dominant wavelength generally increases with depth and therefore the resolution and quality of seismic images typically decreases with increasing depth.

The spatial resolution of seismic reflection data determines how close two points can be located laterally on a reflector and still be recognized as two separate reflecting points (Lindsey,

13

1989). Spatial resolution can be described by an area known as the Fresnel zone (Figure 1-1) (Sheriff, 1980). Reflections points located within the Fresnel zone are beyond the lateral resolution limit and therefore are not distinguishable in the seismic image. The Fresnel Zone can be a measure for seismic spatial resolution. The smaller the Fresnel zone, the smaller the distance between two differentiable reflecting points and therefore the higher the spatial resolution of the seismic data. The area of the Fresnel zone is dependent on the seismic wavelength and increases with depth:

$$ r = \sqrt{\frac{Z\,\lambda}{2}} \tag{1.2} $$

where Z is the depth to the reflector in meters. The Fresnel zone increases with higher wave velocities and can be expressed in terms of the dominant frequency (f):

$$ r = \frac{v}{2}\sqrt{\frac{TWT}{f}} \tag{1.3} $$

where TWT is two-way travel time of propagating waves (Herron, 2011). This previous equation indicates that the higher the frequency content, the smaller the size of the Fresnel zone, and therefore the higher the spatial resolution of seismic data. The size of Fresnel zone is one of the field parameters considered in seismic acquisition design since it is related to focusing seismic reflections at targeted depths (Lines and Newrick, 2004).
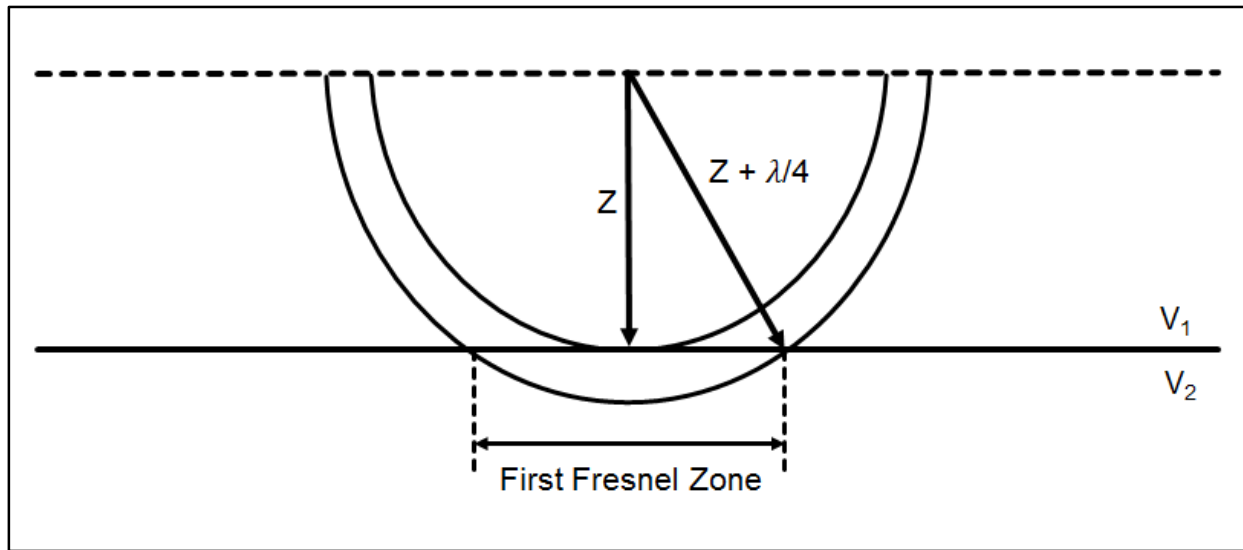
Figure 1-1: Spatial resolution of seismic data can be described by the Fresnel zone. Z is the depth to the reflector, λ is the dominant wavelength, V_1 and V_2 are velocities above and below the reflector.

Different methods of seismic acquisition and processing are implemented for the purpose of improving the quality and resolution of seismic imaging. Efforts in designing acquisition surveys typically aim to preserve high frequency contents while attenuating noise (e.g. by a sufficient energy source, and adequate sampling rate and antialiasing filters). Similarly, in seismic processing, deconvolution, stacking and migration are three fundamental steps routinely implemented for the purpose of improving the acquired seismic data (Yilmaz, 2001).

Improving seismic resolution has always been an essential component of imaging the subsurface. A significant amount of geophysical research is devoted to the topic of reducing ambiguity in seismic data and improving the resolution of seismic imaging. Nevertheless, imaging structural features at depth can still be problematic (discussed in Chapter three). It is then necessary to implement other interpretational tools such as kinematic forward modeling to predict structures at depth (discussed in Chapter four).

Interpretation of the subsurface from clear seismic images should be based on sound geological principles. Therefore, knowledge of tectonic settings and geologic history of an area is necessary prior to undertaking any seismic interpretation project. The studied region in this thesis, Taranaki Basin, is currently undergoing extension (King and Thrasher, 1996) and therefore is expected to exhibit extensional structural features in the subsurface.

1.3 Extensional structural styles

Extension in Earth causes crustal stretching that results in normal faulting (i.e. downward movement of hanging-wall beds along a fault surface relative to the foot-wall beds). Faulting is one of the most important structural deformations in rocks since it influences the regional setup and petroleum distribution in fault-related traps (Davis et al., 2012). Examples of structures caused by extension are full graben, half graben above a listric fault, domino half grabens and ramp and flat geometry (Figure 1-2).

Ramp-flat-ramp geometries are formed usually along large-scale extensional faults. This geometry is typically associated with extensive deformations in the hanging-wall caused by hanging-wall rocks moving along the curved fault surface (Fossen, 2010). Extensional listric faults tend to flatten along weak zones such as evaporate layers or overpressured shape sequences (Fossen, 2010). Analogue models performed in labs (e.g. Ellis and McClay, 1988) have shown that faulting along ramp-flat-ramp geometry can result in folding and reverse faulting.

A special type of folding known as extensional fault-bend fold, or rollover, can occur above a normal fault surface due to hanging-wall movement along the fault surface during extension. Folding occur as a result of hanging wall collapse along inclined axial shear surfaces

at fault bends. Xiao and Suppe (1992) and other researchers have shown how the geometry of a normal fault surface can be predicted in the subsurface based on the shape of the hanging wall of that normal fault. The application of this geometrical relationship between a normal fault and its deformed hanging-wall layers can serve as powerful prediction tool for structural interpretation in extensional settings.
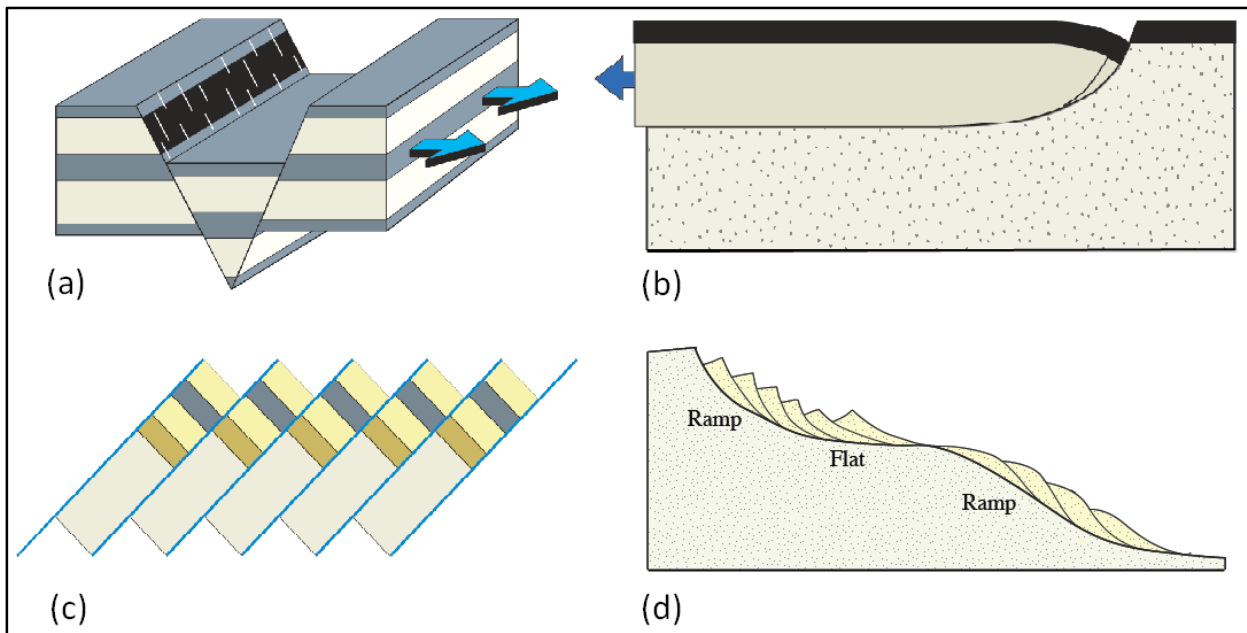
Figure 1-2: Examples of extensional structural styles (a) Full graben (b) Independent half graben above listric major fault (c) Domino half grabens (d) Ramp-flat-ramp geometry (modified after Fossen, 2010)

1.4 Dataset

The dataset used in this study is provided by the New Zealand Petroleum and Minerals (NZP&M), which manages the New Zealand Crown Mineral Estate (oil, gas, coal and mineral resources). A compiled open-file report system along with an extensive exploration and production data are provided by the New Zealand's oil and gas industry for public accessible under the Crown Minerals Act 1991 Section 90 of the New Zealand's Ministry of Economic

17

Development. This includes seismic and well data along with compiled open-file reports database (data.nzpam.govt.nz).

1.4.1 Seismic data

The seismic reflection survey used in this study is Te Kiri 3D. This seismic reflection survey is located southwest Mountain Taranaki, onshore Taranaki Peninsula. Te Kiri 3D survey was acquired after predictions of commercial prospectivity in the area after drilling the exploration well, Te Kiri-1, which shows presence of oil and gas in the Miocene- and Eocene-aged reservoir sequences (Todd Energy, 2006).

1.4.2 Well data

The main well data used in this study are from two exploration wells, Te Kiri-1 and Te Kiri-2. Both wells are located within the Te Kiri 3D seismic survey. Well data (e.g. checkshot survey, reference depths, wireline logs, and deviation survey) were used to load the data on the workstation and tie the seismic reflection data to the well data. Both seismic and well data were loaded into the KINGDOM Suite for quality check and interpretation.

1.5 Thesis Objectives

The main objective of this thesis is to interpret the geometry of a major fault in a 3D seismic volume. Interpretations are then related to the geological history and tectonic settings of the region to assure that results are validated based on geologic principles. A particular interest is given to interpretation of the major fault and seismic horizons at shallow reflections which are required for the second objective of this thesis.

The second objective of this thesis is to construct kinematic structural forward models for the major fault in the 3D seismic volume to predict the fault's trajectory at deep reflections where the fault trace is not clearly visible. The kinematic forward models are based on principles related to the extensional fault-bend fold theory. Modeling the major fault in the interpreted seismic volume reveals the geometry of the fault surface, which cuts through the proven gas reservoir in the subsurface and possibly contributes to the gas presence observed along the interpreted fault.

The third objective of this thesis is to analyze the possible gas presence associated with normal faults in the seismic volume. The interpretation of the fault-related gas leakage in the survey is undertaken using different volumetric seismic attributes.

1.6 Thesis Outline

Chapter two covers the geologic background of The basin's history. It discusses the tectonic kinematics and explains the evolution of Taranaki Basin through geologic times. The chapter links the deformation mechanisms in the subsurface to potential hydrocarbon traps. This chapter discusses the contribution of tectonic activities to the faulting patterns and subsurface structure since the initiation of Taranaki Basin in the mid-Cretaceous.

Chapter three shows interpretation of the major fault in the seismic volume and relate it to two active faults previously studied on Taranaki Peninsula. The chapter discusses the quality of the seismic images and shows horizons interpretation from the 3D seismic reflection survey. This chapter also addresses the possible gas presence along normal faults predicted in the seismic images. The chapter explains the gas effect on the seismic reflections, and defines different seismic attributes used for predicting the possible gas presence along normal faults.

19

Chapter four shows the created kinematic forward models and explains the main concepts behind the created models. The chapter describes how the geometry of a normal fault is related to strain in its hanging wall and show the use of the models to predict fault geometries at poorly imaged deep reflections.

Chapter five summarizes the results and discusses the conclusions of this thesis.

1.7 Software

The following software was used for my work on this research project:

- KINGDOM® Suite: for geological and geophysical interpretation of seismic and well data
- Rock Solid Attributes™: for computation of geometric attributes from seismic data
- StructureSolver™: for balanced forward models of deformation associated with faults
- Microsoft® Office: for spreadsheet, word processing and image editing

Chapter Two: Geological Background of Taranaki Basin

2.1 Introduction

The primary objective of this chapter is to provide a background for the geologic history of Taranaki Basin, New Zealand. Deformation in the subsurface of Taranaki Basin is linked to the tectonic kinematics, which explains the basin's evolution through geologic time. Understanding these deformation mechanisms is essential for targeting potential structures trapping hydrocarbon in the subsurface. This chapter provides an overview of the tectonic setting since the initiation of the basin in the mid-Cretaceous. Subsequently, the chapter discusses the contribution of these tectonic activities to the faulting patterns and subsurface structure in the basin.

2.2 Background

Taranaki Basin is a rift complex basin covering approximately 330,000 km^2 both onshore and offshore of western North Island, New Zealand (Figure 2-1). Taranaki Basin is the only producing oil and gas province in New Zealand, with majority of exploration wells drilled in anticlinal or four-way dip closures. The basin is considered relatively under-explored with potential petroleum plays in many thrust and inversion structures, half-graben fill and extensional structures (NZP&M report, 2013).
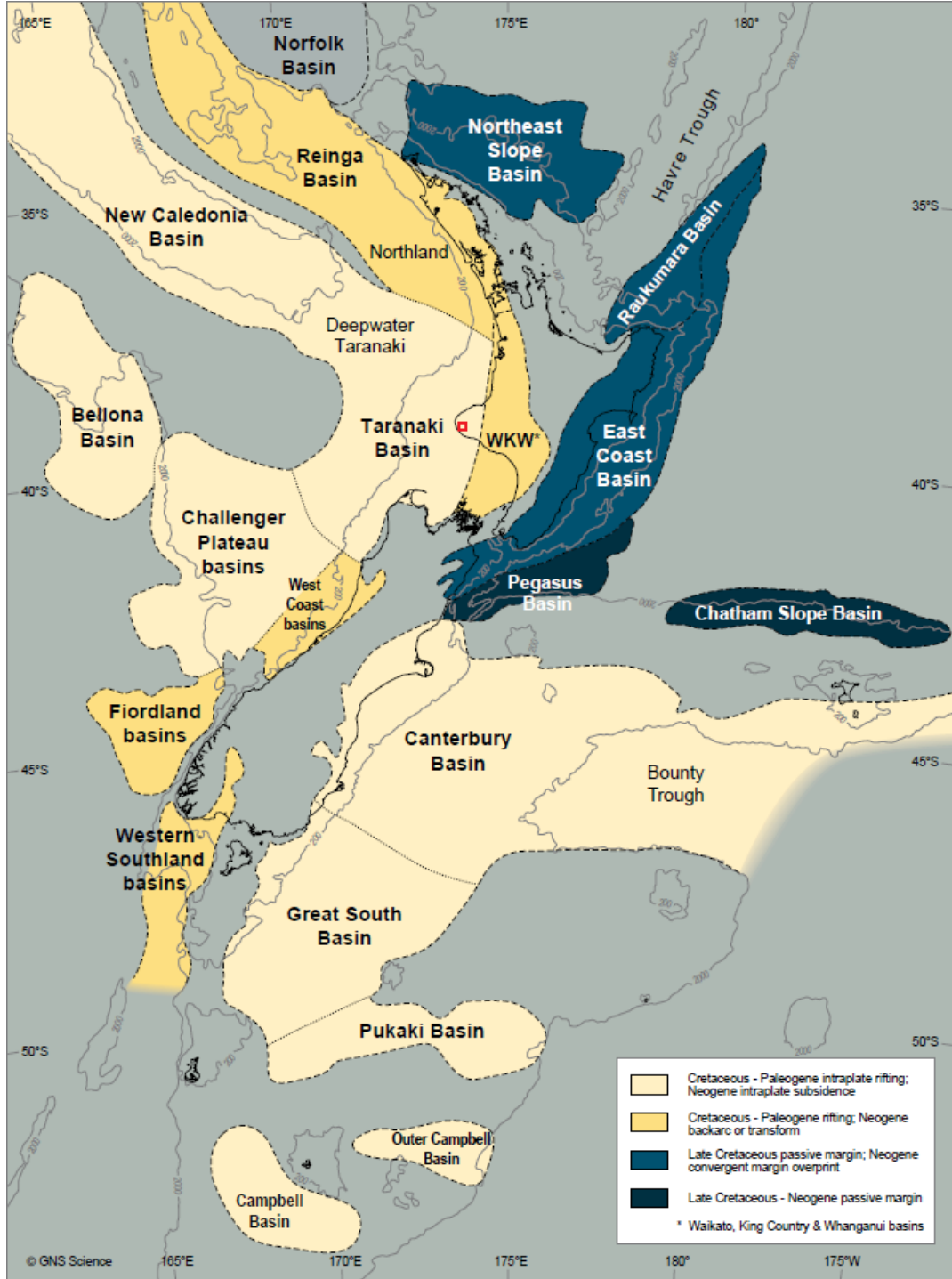
Figure 2-1: Taranaki Basin location among adjacent basins in western North Island, New Zealand (from NZP&M, 2013). Studied location indicated in red.

2.3 Tectonic Settings

Taranaki Basin is located on the active boundary of the Australian and Pacific tectonic plates and has undergone different phases of deformation. The Taranaki Basin was part of the Pacific Plate during the basin's early evolution. Mid-Cretaceous comprises a pre-rift/break-up phase followed by extension and left-lateral shear, contributing to the initiation of the basin and marking a phase of syn-rift and drift during the Late Cretaceous to Paleocene (Figure 2-2).

The basin then has undergone a passive margin phase during post-rift/drift Paleocene-Early Oligocene times, which involved a subsidence in the eastern part of the basin. A renewed episode of subsidence started in mid-Oligocene in central areas of the basin and an overall subsidence influenced the basin during Oligocene to Early Miocene times (ranges from about 500-2000 m) (King and Thrasher, 1996). Subsidence during Oligocene was associated with westward downthrow of Taranaki Fault in the eastern limit of the basin (King and Thrasher, 1996).

Taranaki Basin evolved as an east active and west passive margins, separated by the western limit of the Australian-pacific boundary. The active part is referred to as the Eastern Mobile Belt (or the "Taranaki Graben") and the inactive margin is referred to as the Western Stable Platform (Figure 2-3). Even though areas such as the Taranaki Peninsula experienced uplift at some period during the Neogene, rapid subsidence beginning mid-Oligocene contributed to an overall net subsidence in the Eastern Mobile Belt. The overall subsidence in the east exceeded the relatively undeformed Western Stable Platform which remained mostly inactive since the Cretaceous.

The basin also experienced a deformation phase of contraction in late Eocene to Miocene, involving a major horizontal compression during early Miocene in the eastern part of the basin.

23

In the Early Miocene, the Taranaki basin was subject to the changing converging plate boundary during which the Taranaki Fault overthrust westwardly, resulting in a reverse upward movement of the basement by up to 6 km in the eastern limit of the basin.

During Pliocene to Pleistocene, the basin deformed along the plate boundary in the eastern part of the basin and resulted in major areas of extension. This Plio-Pleistocene extension has contributed to an overall net subsidence in the basin, except for the eastern uplifted and tilted areas, and the southern inversion region.

2.4 Subsurface Structure

The basin's subsurface structure is significantly influenced by the tectonic history of the basin and directly related to deformations along the Australian-Pacific plate boundary. As previously mentioned, the structure of the Basin consists of two main regions, the Western Stable Platform (passive margin) and the Eastern Mobile Belt (active margin) (King, 1991; King et al., 1991; King and Thrasher 1996). Deformation is mainly characterized by extension and compression, which are both evident in the Eastern Mobile Belt. The border between these two regions is marked by the western limit of the current Australian-pacific plate boundary. The complex tectonic activities resulted in various structural styles in Taranaki Basin, including normal and reverse faulting along with structural inversion, contained within superimposed sub-basins, depocentres, and uplifted regions.
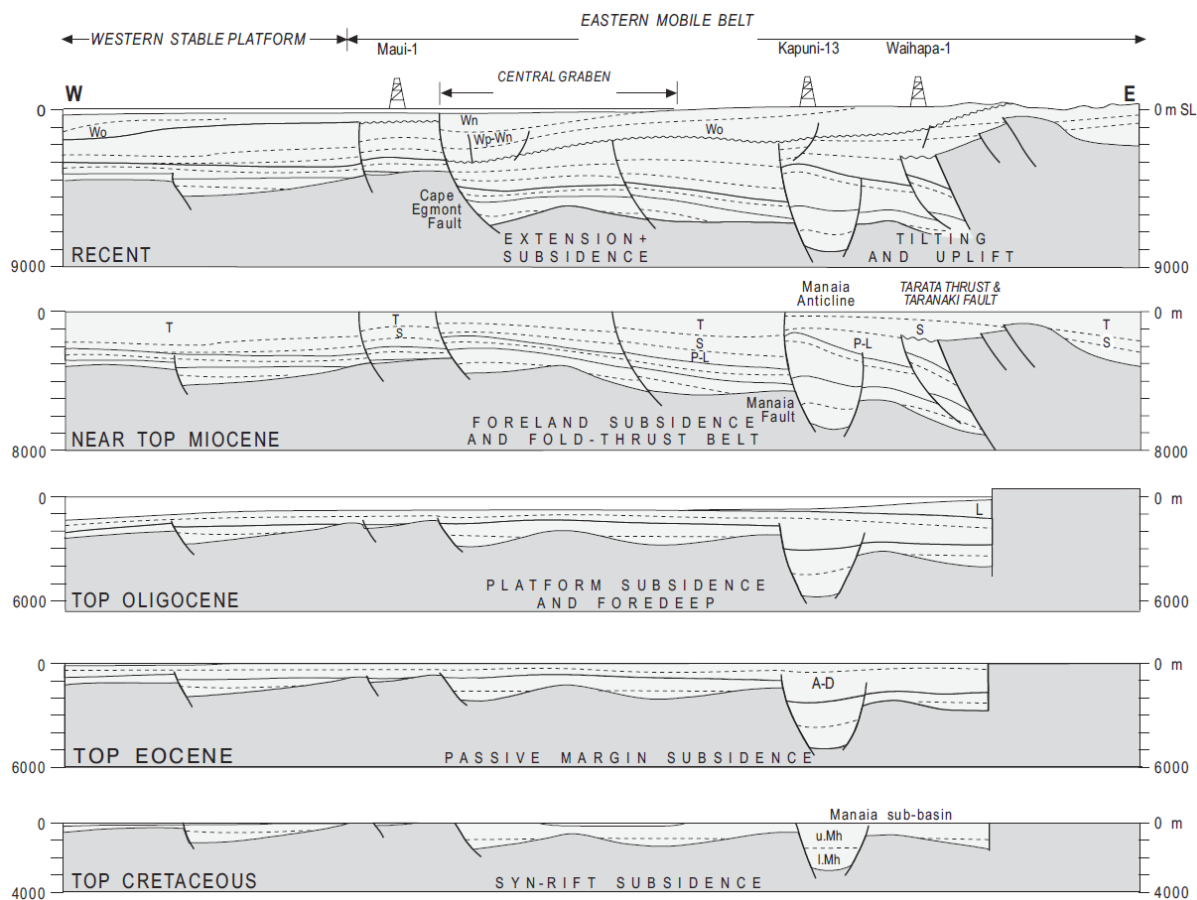
Figure 2-2: Taranaki Basin development from Late Cretaceous to Recent (from King & Thrasher, 1996). Location on map is shown in Figure 2-3

2.4.1 Western Stable Platform

The Western Stable Platform resembles a region with no tectonically-related deformations. It generally exhibits Cretaceous-Paleocene rift-related half-grabens overlain by unfaulted flat-laying Eocene-Recent depositions, indicating regional subsiding progradational strata. The platform reflects the inactivity of the area since the Cretaceous.

2.4.2 Eastern Mobile Belt

The Eastern Mobile Belt contains several sub-basins and provinces, including the Central and Northern grabens, Southern Inversion Zone, Tarata Thrust Zone, Mohakatino Volcanic

Centre and the Toru Trough. The studied area is located at western Taranaki Peninsula which is part of the Central Graben. The subsurface structure in the Eastern Mobile Belt resembles the complex history of the basin's evolution and deformations related to the Kaikoura Orogeny (e.g. Suggate et al. 1978 and King & Thrasher, 1996).

Different types of deformation occurred in the Eastern Mobile Belt throughout different geologic times resulting in complex faulting patterns. Even though strike-slip deformations may have affected areas in the basin, most offsets are due to dip-slip faults striking mainly to the north and northeast (e.g. Voggenreiter, 1993; King and Thrasher, 1996). Many of these north-trending originated during the rifting phase in Late Cretaceous and were then reactivated during the Cenozoic. The northeast faults were mainly active during the late Cenozoic time, whereas northeast-trending normal faults in the southwest part of the basin were the result of the Late Cretaceous rifting. The Late Cretaceous structure consists of fault-controlled sub-basins resembling an oblique extension zone during the Taranaki Rift (Thrasher 1990b, 1992a).

The Eastern Mobile Belt is bounded in the eastern-most limit by the Miocene age Taranaki Fault, extending for more than 250 km and truncating younger Miocene layers (King and Thrasher, 1996). The Taranaki Fault is a major reverse fault dipping eastward and has contributed to the basin's structure, vertically shifting the basement by up to 6 km (King and Thrasher, 1996). The Taranaki Fault along with adjacent subparallel reverse faults to the east form the Taranaki Fault zone, have increasingly uplifted the basement on the east side of the fault.

Paleogene structure shows evidence of normal faulting in Paleocene representing the final stage of early basin rift and generally undisrupted strata during the Eocene. Structure during Oligocene indicates rapid subsidence, mostly east of the basin.

During Neogene, the Eastern Mobile Belt was part of the deformational processes related to the converging Australian-Pacific plate boundary. In the central part of the Eastern Mobile Belt, deformation was the result of compression during Miocene followed by extension overlap. The subsurface structure of the Eastern Mobile Belt indicates an overall net subsidence, including uplifted areas such as the Taranaki peninsula which experienced reverse faulting during Miocene along with normal faulting during Pliocene to Recent times. In the northern part of the basin, the subsurface is deformed mainly by Late Miocene-Recent normal faulting which represents the western limit of the plate-boundary deformation (i.e. the Cape Egmont Fault Zone). In the south of Taranaki Basin, the subsurface structure of the Eastern Mobile Belt hosts Miocene-Recent reverse faults along with structural inversion. King and Thrasher (1994) classified deformation during Neogene in the Eastern Mobile Belt based on two different stress regimes:

1. The northern sector (currently under extension), including the Northern and Central Grabens.

2. The southern sector (have undergone compression): the Tarata Thrust Zone and the Southern Inversion Zone (southern part still is still under compression).
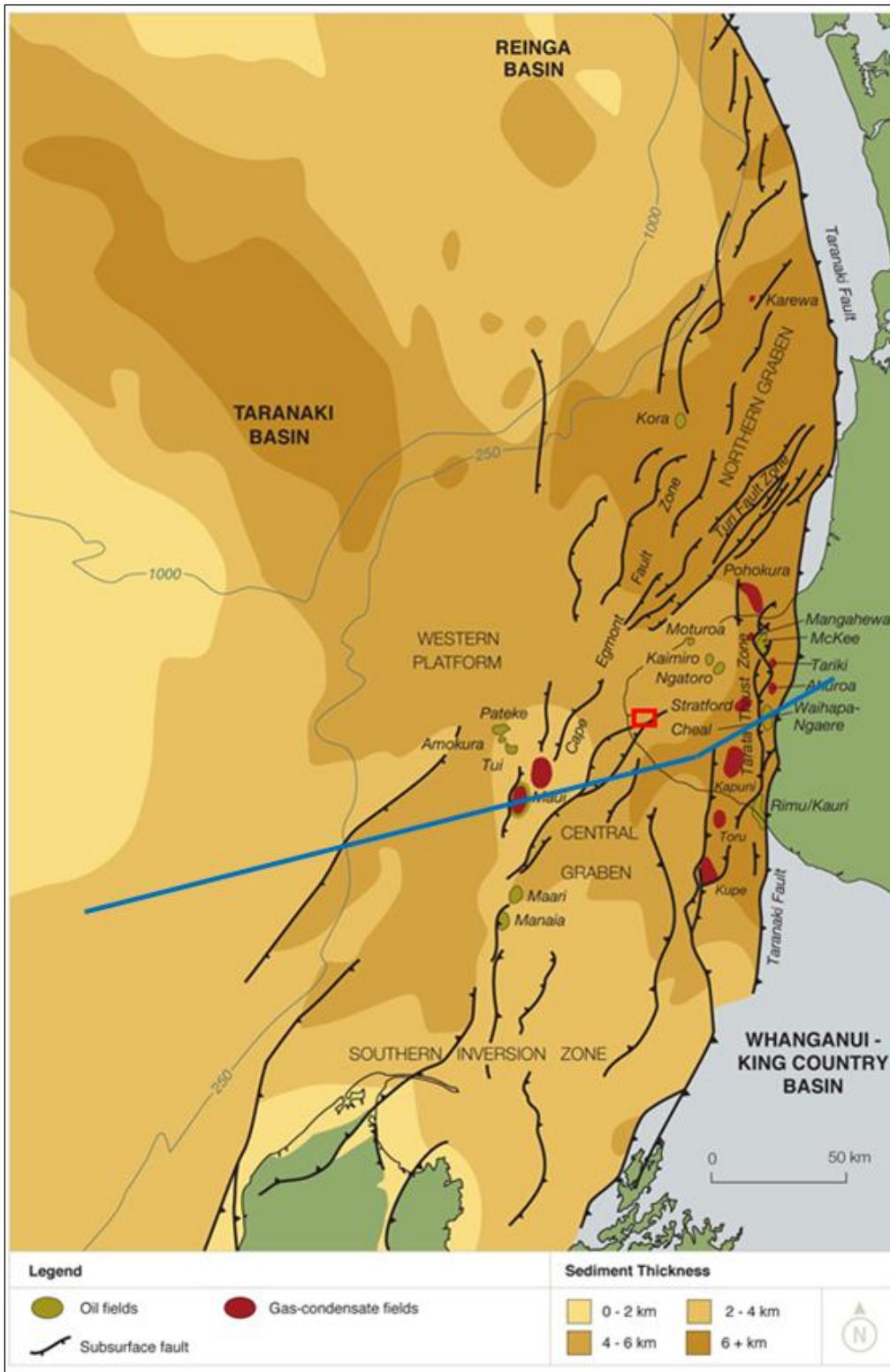
Figure 2-3: Taranaki Basin sub-provinces. Studied area is labeled by the red box. Blue line shows the cross-section location in Figure 2-2 (after NZP&M, 2013)

2.4.3 Active Faults

Active faults in New Zealand are linked to earthquake activities, including the recent large-scale ones in 2010 (e.g. Dissen et al., 2011) and 2011 (e.g. Lawton et al., 2013) near Christchurch in the Canterbury region, caused by a previously unknown active fault (Quigley et al., 2010). Within the Taranaki Basin, areas of active faulting in the Eastern Mobile Belt seem to be mainly within the onshore Taranaki Peninsula and spread south to the offshore part. Fault displacements in the Late Quaternary indicate active deformation in the basin (e.g. Nodder 1993, Nicol et al. 2005, Townsend et al. 2010). Active faults on the Taranaki Peninsula are of a particular interest, specifically in the western part of the peninsula, southwest of Mt Taranaki, where the study was conducted.

Active faults southwest of Mt Taranaki (Figure 2-4) consist of six northeast-southwest striking faults, named Rahotu Oaonui, Kina, Ihaia, Kiri and Pihama Faults. Studies of theses six active faults were conducted, including short-term (high-quality trench) and long-term data (seismic reflection surveys), and some of the results are shown in Table 2.1 (Townsend et al., 2010) and Table 2.2 (Mouslopoulou et al., 2012). Results from Townsend et al. (2010) show that these low-throw active faults can generate M_w 6.1-6.6 earthquakes, whereas Mouslopoulou et al. (2012) show that the variable displacement rates are related to the changing intervals of the earthquake recurrence. Two of these active faults will be discussed in later chapters: the Oaonui and Kina Faults.

Table 2.1: Estimated parameters for active faults SW Mt Taranaki (Townsend et al., 2010)

Fault	No. of events (over time period)	Single event displacement (m)	Recurrence interval (ka)	Max. rupture length (km)	Magnitude (Mw)
Rahotu	2 (14 ka)	0.3-1.2 (0.75)	6.7^4	20	6.5
Oaonui	4 (24 ka)	0.4-0.7 (0.48)	$5.2\text{-}8.6^4$ (6)	25	6.7
Kina	3 (7.8 ka)	0.4-0.8 (0.6)	2.6	30	6.8
Ihaia	$3\text{-}10^2$ (5 ka)	0.3-1 (0.67)	$0.5\text{-}1.7^2$ (1.14)	28	6.7
Kiri	$5\text{-}17^2$ (7.8 ka)	0.3-1 (0.67)	$0.5\text{-}1.7^2$ (1.06)	30	6.8
Pihama	4 (27 ka)	0.3-1.5 (0.8)	$3\text{-}15^4$ (4.9)	25	6.7

Table 2.2: Attributes for active faults SW Mt Taranaki (Mouslopoulou et al., 2012)

Fault	Dip (°)	Active-fault trace (km)	Subsurface fault trace (km)	Holcene displacement rate (~10 kyr)	Long-term displacement rate (3.6 Ma)
Rahotu	85 SE	1.4	20	0.16	0.11
Oaonui	80-90 NW	13.2	25	0.11	0.08
Kina	80-85 NW	4	30	0.40	0.18
Ihaia	60-80 NW	5	28	0.35	0.10
Kiri	80-90 NW	6	30	1.67	0.03
Pihama	80-85 NW	4	25	0.21	0.10
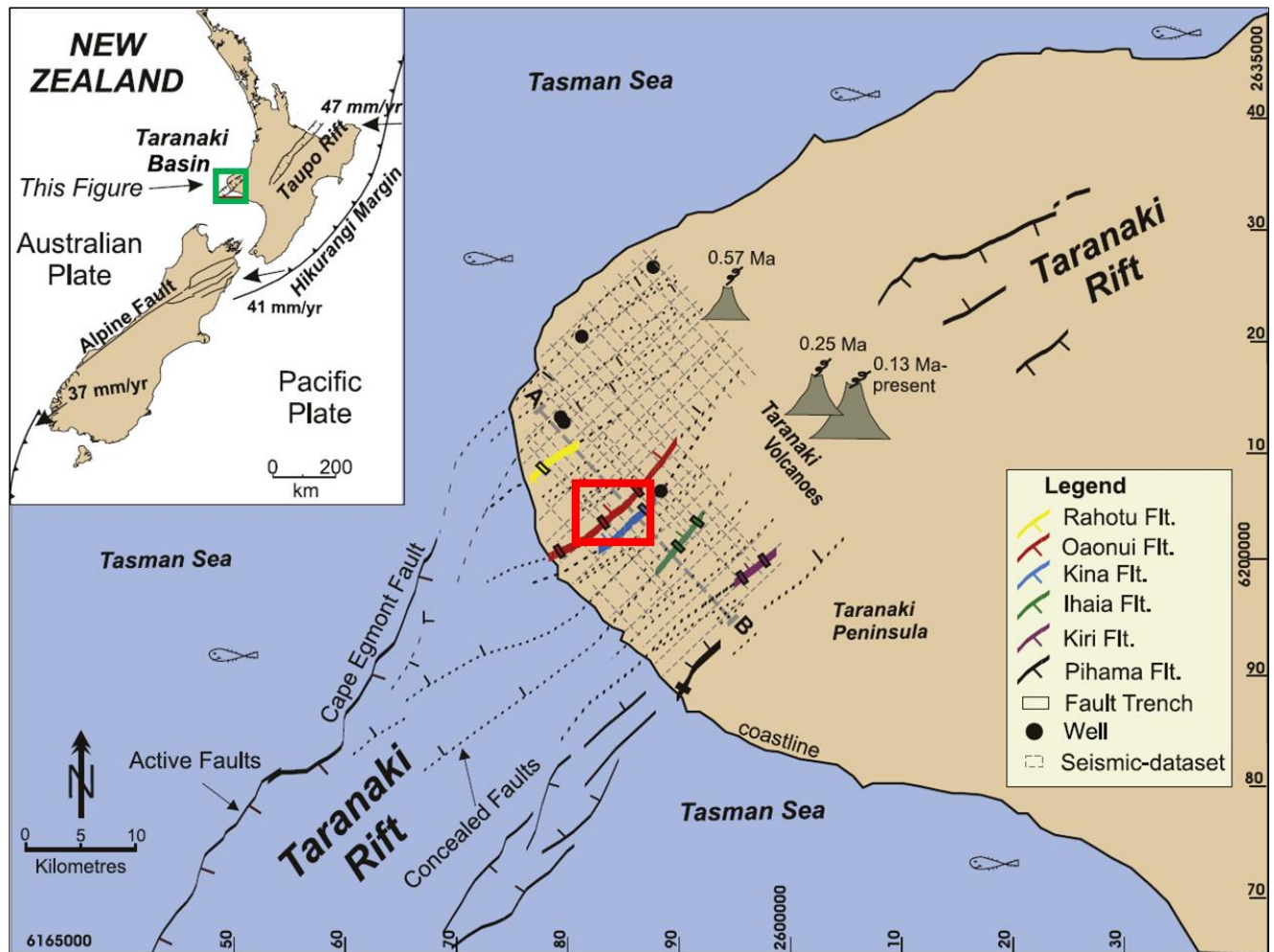
Figure 2-4: Six active faults onshore Taranaki Basin. Studied area is labeled by the red box (after Mouslopoulou et al., 2012)

2.5 Summary

Taranaki Basin consists of complex subsurface structure resulting from various tectonic activities from mid-Cretaceous to Recent. Different types of deformation characterize the basin's structure, specifically in the eastern region. Most faults in the basin are north- or northeast-trending. Many of these extensional faults are associated with the Late Cretaceous rifting and were reactivated during Cenozoic. The basin experienced post-rift contraction and regional subsidence during Eocene to Early Oligocene.

31

The basin has evolved within two tectonic settings: active eastern margin and passive western margin. These two tectonic settings resulted in two structural regions: the Eastern Mobile Belt (active margin) and the Western Stable Platform (passive margin). The Eastern Mobile Belt experienced a net subsidence during Neogene where as the Western Stable Platform has been relatively inactive since the Cretaceous.

The Eastern Mobile Belt can be classified into a northern sector, including the Northern and Central Grabens, and southern sector, including Tarata Thrust Zone and the Southern Inversion Zone. Within the Central Graben, six north-east trending active faults are known southwest of Taranaki peninsula: Rahotu Oaonui, Kina, Ihaia, Kiri and Pihama.

Chapter Three: Interpretation of Major Faults and Possible Gas Leakage in Southwest Taranaki Peninsula

3.1 Introduction

This chapter focuses on interpreting and recognizing a major fault (hereafter referred to as the "major fault") from a three dimensional seismic reflection survey in southwest Taranaki Peninsula. This major fault is related to two active faults in Taranaki Peninsula, named the Oanui and Kina Faults.

The major fault geometry can be clearly visible at the shallow reflections of the interpreted seismic volume (e.g. above hree seconds TWT). The major fault's geometry at deep reflections is not clearly visible due to limitations in seismic imaging. The geometry of this major fault, at the deep poorly imaged seismic reflections, is predicted by kinematic balanced-forward models discussed subsequently in Chapter four. This model-based prediction is based on the relationship between a fault geometry and deformations in its hanging wall. Constructions of these kinematic forward models for fault deep trajectory predication require knowledge of shallow stratal deformation (e.g. a seismic horizon as a reference bed) and the fault shape at that shallow level (e.g. interpreted horizon cutoffs at the fault) (e.g. Xiao and Suppe, 1992 and Groshong, 2006). Therefore, a primary objective of this chapter is to interpret the major fault geometry as well as the stratal deformation at shallow reflections

This chapter also addresses possible gas presence observed along some faults in the subsurface. Faults in extensional regimes can [generally] act as gas migration pathways when in contact with a hydrocarbon source. Gas migrating upsequence along conduit faults can be detected in seismic volumes (e.g. Ilg et al., 2012). The seismic response of waves traveling through low velocity intervals within a gas zone shows incoherent reflections characterized by

vertical chaotic patterns. Seismic attributes such as semblance and curvature can assist in detecting gas presence and highlighting locations of the associated permeable faults.

Interpretation of the studied 3D seismic survey was performed using different display orientations, picking modes and computed seismic attributes.

3.2 Seismic Survey: Te Kiri 3D

3.2.1 Background

The 3D seismic volume used in this study is the Te Kiri 3D which is located onshore, southwest Mt. Taranaki on the Taranaki Peninsula, New Zealand (Figure 3-1a). Sediments in the area, similar to other parts of the Taranaki Basin, are of late Cretaceous age and younger (Figure 3-1b). The main objective of this survey, when it was undertaken, was to achieve a high resolution image of the targeted reservoir level while maintaining the relative amplitude and long offset data. Another objective of this survey was to image faulting clearly within and above the targeted reservoir zone, which was estimated to be at 2.5s TWT.

Te Kiri 3D survey was acquired after predictions of commercial prospectivity in the area after drilling the exploration well, Te Kiri-1 (Todd Energy, 2006). This well showed indications of oil and gas presence in the Miocene- and Eocene-aged reservoir sequences.
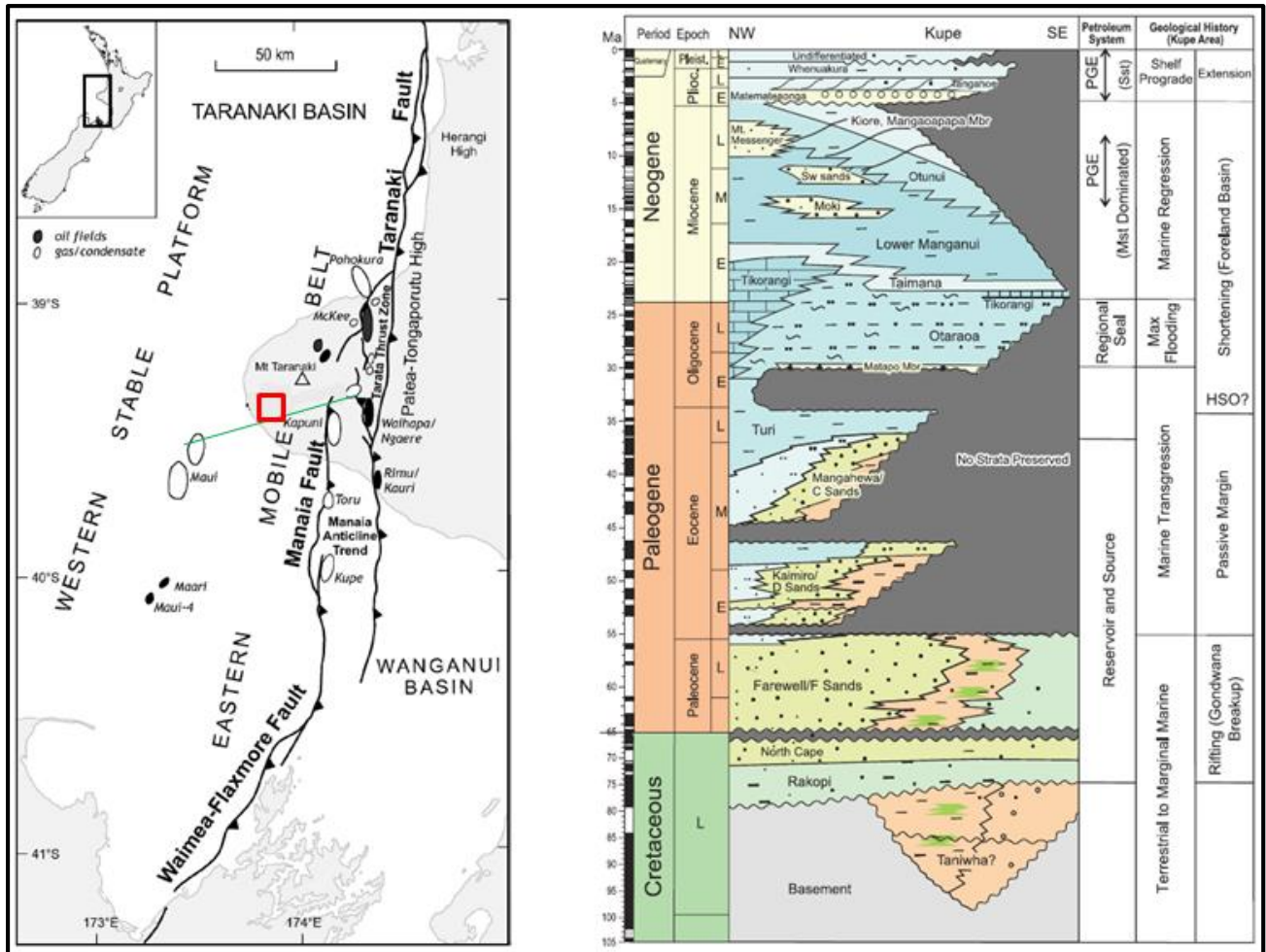
Figure 3-1: (a) Te Kiri 3D survey area in red box, cross-section in Figure 3-2 by green, (b) Stratigraphic column (after Ilg et al., 2012)

3.2.2 Data Acquisition

The acquisition parameters for Te Kiri 3D are summarized in Table 3-1 (Todd Energy, 2005). The survey was acquired over an onshore area of 90 sq km. Dynamite was used as the energy source with a 400 m line spacing. Sensors were aligned orthogonally (322.6° line-bearing) with 400 m line spacing. The resultant was approximately 4550 shotpoints on 24 source-lines and 4570 sensor points on 32 receiver-lines. A source interval of 50 m and receiver interval of 50 m were used resulting in a bin size of 25m x 25m (inline x cross-line).

35

Table 3.1: Acquisition parameters summary of Te Kiri 3D Survey (Todd Energy, 2006)

TE KIRI 3D ACQUISITION PARAMETERS	
Source Type	Explosive
Charge Size	1.5 / 2 kg
Shot Depth	5 / 10 m
Source interval	50 m
Source Line Spacing	400 m
Receiver Interval	50 m
Receiver Line Spacing	400 m
Recording Patch	12 x 128
Max Number of Channels	1536
Bin Size	25 m inline x 25 m crossline
Maximum Offset	3785 m
Nominal Fold	48
Correlation Type	Zero Phase
Sample Period	2 ms

3.2.3 Data Processing

The processing sequence of this seismic survey is show in Table 3-2 (Todd Energy, 2005). Te Kiri 3D was processed by Fugro Seismic Imaging in 2005 (Todd Energy, 2005). The processing flow involved applying FK filtering, radial trace filtering, deconvolution, residual statics, PSTM, mute, post-stack spectral whitening, FXY deconvolution, bandpass filter and scaling (Todd Energy, 2005). Some remarks from data processing are worth mentioning to emphasize the data quality and limitations.

Interpreted data of this survey is a pre-stack time migrated volume (PSTM, two way travel time in seconds). The refraction statics were applied to sea level datum and a two-layer model was applied to resolve some artifacts caused by the weathering layer. Static corrections were applied to the final datum and the time origin was shifted -300 ms. Velocity analyses were performed in 4 phases (1x1 km intervals, then 0.5x0.5 km interval for denser velocity field). The

migration algorithm used was 3D pre-stack Kirchhoff migration, applied in common offset and

azimuth order, with 100% smoothed velocity and maximum aperture of 5.0 km.

Table 3.2: Te Kiri 3D Processing Flow (Todd Energy, 2005)

GAIN RECOVERY
GEOMETRY
3D REFRACTION STATICS
SWELL NOISE ATTENUATION AND DESPIKE
RADIAL FILTER
3D SURFACE CONSISTENT DECONVOLUTION
VELOCITY ANALYSIS I (1.0 km x 1.0 km)
3D SURFACE CONSISTENT RESIDUAL STATICS I
VELOCITY ANALYSIS II (0.5 km x 05 km)
3D SURFACE CONSISTENT RESIDUAL STATICS II
3D SURFACE CONSISTENT AMPLITUDE CORRECTION
DESPIKE
3D BINNING
3D KIRCHHOFF PSTM (VELOCITY LINES)
VELOCITY ANALYSIS III (0.5 km x 05 km)
3D KIRCHHOFF PSTM
VELOCITY ANALYSIS IV (0.5 km x 05 km)
SPHERICAL DIVERGENCE AND DB GAIN
NMO CORRECTION
OUTER TRACE MUTE
RESIDUAL NMO (GATHER FLATTENING)
FLOATING DATUM TO FINAL DATUM MSL=0 m
COMMON MIDPOINT STACK
FXY DECONVOLUTION
BAND PASS FILTER
SCALING

3.3 Data Interpretation Methodology

3.3.1 Horizons interpretation

Interpretation of Te Kiri 3D volume was performed on a workstation using seismic interpretation software, KINGDOM® Suite SMT. After loading the seismic and well data on the workstation, a synthetic seismogram was created from Te Kiri-1 well data and tied to the seismic volume at the well location. The seismic synthetic trace was generated by convolving an extracted wavelet from the seismic data with the reflection coefficient created by sonic and density logs. Synthetic seismograms along with formation tops from the well data provide a good correlation between seismic and well data which help identify the geologic horizons of interest.

Seismic interpretations of the subsurface structure were based on picking horizons along coherent reflections of the same phase. This usually translates to picks on a peak or trough in seismic surveys, such as Te Kiri 3D, with zero phase correlation type. These seismic responses (e.g. peak and troughs) resemble differences in acoustic impedance between different earth materials. The continuous same-phase reflections are interpreted as horizons representing stratal surfaces, whereas discontinuities are interpreted to represent fault displacements or unconformities.

Horizon interpretations of the 3D seismic volume began on vertical sections at the well-tie location and extended outward. Observations of the seismic images were made on different display orientations, including horizontal slices, vertical sections of inlines, crosslines and arbitrary lines.

Horizons were mainly interpreted from seismic reflection amplitudes on vertical sections. Selected inline and crossline sections were initially analyzed to gain a regional perspective of the subsurface structure related to the geological history of the area (discussed previously in Chapter

two). Alternating between inlines and crosslines served as a validation tool for checking the consistency of horizons picks along their associated reflectors.

3.3.2 Fault interpretation

Faults can be interpreted in seismic volumes from both vertical and horizontal sections. Inlines in the studied seismic volume show images along the dominant dip direction and were interpreted to determine the faulting patterns in the seismic volume. Horizontal sections (i.e. time or depth slices) were also an integral tool in interpreting the structure in the studied seismic volume. The horizontal time slices reveal the general orientation of most faults' strikes. Unlike vertical sections, the frequency content of horizontal sections is the same as the trace interval in the data (i.e. spatial sampling) (Yilmaz, 2001). Faults can be observed and interpreted on horizontal sections. Steeper dipping beds in horizontal slices generally appear as narrower reflections than shallower dipping beds (Figure 3-2). In addition, reflections of steeper dipping beds on consecutive time slices appear to change location and move with increasing time (or depth) faster than shallower dipping beds (Figure 3-3).
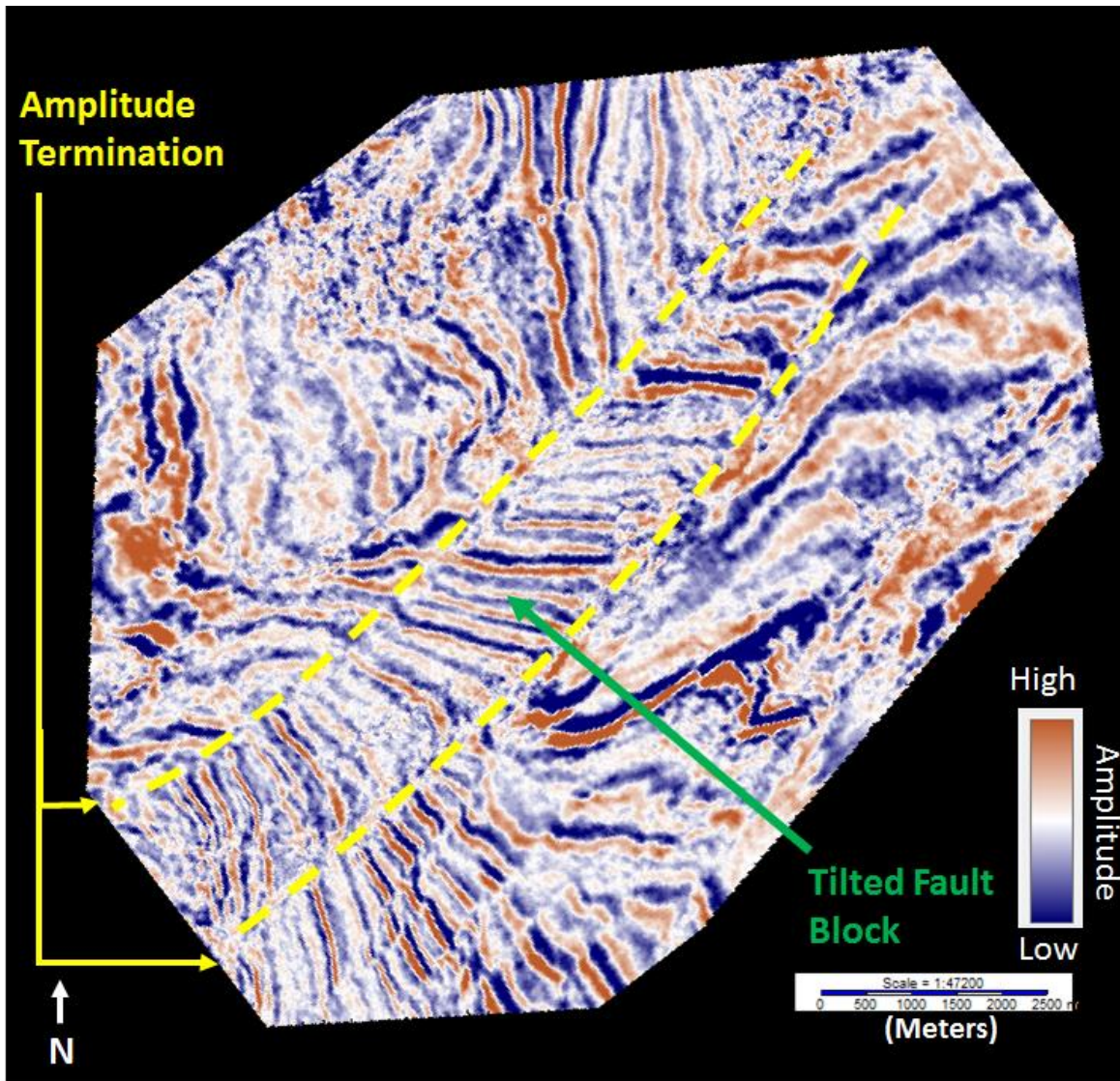
Figure 3-2: Time slice at 810 ms. Steeper dipping tilted fault blocks appear as narrower reflections than shallower dipping beds (green). Amplitude termination at reflection discontinuities indicates fault locations on a horizontal slice (yellow).

Faults appear on horizontal sections as event terminations when they strike at different angle than structural strike (Brown, 2011). Faults in the studied seismic volume were therefore traced at reflection terminations on horizontal slices (Figure 3-2). Figure 3-4 shows amplitude terminations of two faults on a sequence of horizontal slices.

When observing reflections on consecutive horizontal sections, beds reflections appear to change location and shift across the horizontal sections, whereas faults typically remain relatively at their same location (Figure 3-4). Implementing horizontal sections for faults interpretations was generally helpful in identifying and interpreting the geometries of faults in shallower reflections in Te Kiri 3D. Implementation of fault interpretation from horizontal and vertical sections also served as an effective tool for small-scale faults identification.
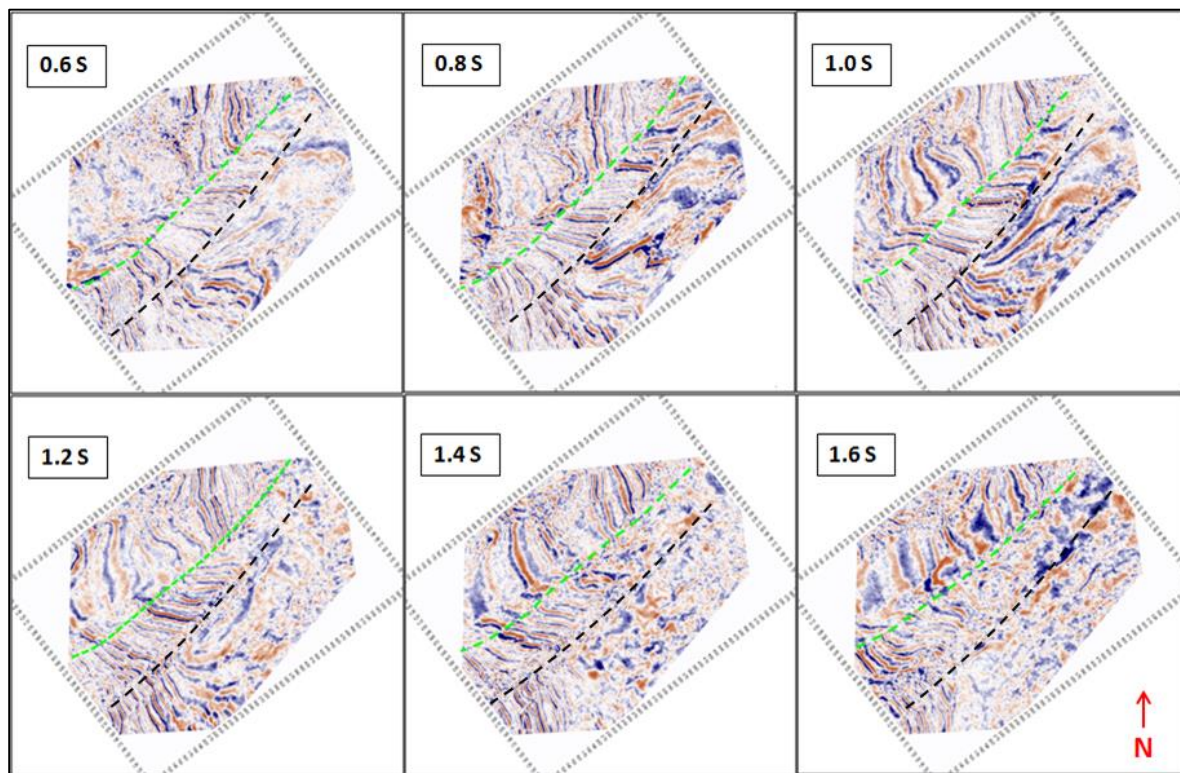
Figure 3-4: A sequence of consecutive horizontal TWT sections. The NE-trending major fault (black dashed line) and its associated secondary synthetic fault (green dashed line).

Initial interpretations of faults in the data were useful in correlating horizons across faults and defining the general structure of the subsurface. In the case of the major fault, deformation in hanging-wall strata are the result of movements along the non-planar fault surface (as discussed

later in Chapter four). Interpretation of a fault is therefore helpful in defining the relationship between the geometry of a fault and the shape of horizons in the hanging wall of that fault.

3.3.3 Fault and Horizon Picking

Seismic interpretation software, KINGDOM® Suite SMT, provides different picking modes for faults and horizons. These picking modes can be manual, automated, or semi-automated. Both manual and automated picking were used in interpreting the studied survey.

Manual picking allows for picking data along reflectors regardless of the phase. Fault surfaces were primarily digitized using manual picking since it provides more control than the other picking methods. Manual picking was also the basis for horizon picking near faults' intersections and in complex areas such as narrow fault blocks. Picking closer line spacing was performed for higher level of details in more complex areas. In areas characterized with good quality and high amplitude continuity in the shallower reflections, horizon autopicking was performed for using manual picks as seed points to infill uninterpreted.

When autopicking is performed for a horizon, poor data areas and fault zones were isolated in map views by polygons. Fault polygons were also used to exclude fault gaps during the horizon autopicking process. In general, horizon autopicking in Te Kiri 3D volume was reasonable for shallow reflectors above three seconds.

Interpreted faults in the shallow sections were easily detected and tracked on horizontal slices using composite sections. Fault picks were then quality controlled to verify that correlated faults are of the same type, age, and of compatible throw.

Faults are generally indicated by observations of discontinuities or breaks in reflections (i.e. hanging-wall and footwall cut-offs). Fault picks are then extended upwards and downward

until the fault trace is near flexure or invisible. Fault picks were mainly made on inlines (dip

lines) and horizontal sections.

On some interpreted vertical sections, irregular amplitude disturbances were observed at

certain locations where major faults intersect with the interpreted top reservoir. These amplitude

disturbances possibly indicate the presence of gas migrating upward along the interpreted faults.

3.3.4 Gas presence along permeable faults

The presence of gas flowing from faults or fractures might be detected by the acoustic

response in a 3D seismic volume (Ilg et al., 2012). This response can be interpreted qualitatively

in conventional horizontal and vertical sections (Løseth et al., 2009). Gas presence along

permeable faults shows acoustic changes in vertical sections appearing as vertical chaotic

disturbances with amplitude anomalies associated with irregular distribution of low-velocity

zones. This vertical incoherence is a result of scattering, attenuation, and decrease in

compressional velocity (Vp) of waves passing through gas saturated pores (Anderson and

Hampton, 1980). The gas leakage often appears in vertical sections as a cone-shaped distortion

when associated with faults Figure 3-5 (Ilg et al., 2012). When fluids flow upward through

permeable faults, gas molecules are typically released due to the drop in pressure (Bjørkum et. al,

1998). When gas replaces formation water, the contrast of impedance increases and causes the

amplitude variations to show as dim and bright spots. This phenomenon is well-illustrated in

time-lapse studies (e.g. Lawton et. al., 2006 and Alshuhail and Lawton, 2007). The decrease of

P-wave velocity due to gas presence explains the seismic push down often observed within the

leakage zone (Figure 3-6). The velocity drop is due to changes in density and bulk modulus

caused by the gas presence. Mathematically, this is explained in a simplified medium (i.e. elastic,

homogeneous, and isotropic) by Mavko et al. (2003):

$$Vp = \sqrt{\frac{K + \left(\frac{4}{3}\right)\mu}{\rho}} \qquad (2.1)$$

where K is bulk modulus, μ is shear modulus, and ρ is density. Pore pressure and temperature

affect the bulk modulus and density values. However, even at increased pore pressure values,

bulk modulus remains the main parameter affecting the change in P-wave velocity due to the

high compressibility of gas which reduces bulk modulus K (Anderson and Hampton, 1980). This

explains the drop in compressional velocity due to the gas presence, regardless of the decrease in

density. It also explains the reason for shear wave velocity (Vs) to remain insensitive to the gas

presence since Vs is not affected by the compressibility of gas and can be described

mathematically in a simplied medium by:

$$Vs = \sqrt{\frac{\mu}{\rho}} \qquad (2.2)$$

Computed seismic attributes such as semblance and curvature were useful in detecting

what was interpreted as gas presence along permeable faults in conventional seismic volumes.

The following section discusses seismic attributes and some of their applications.
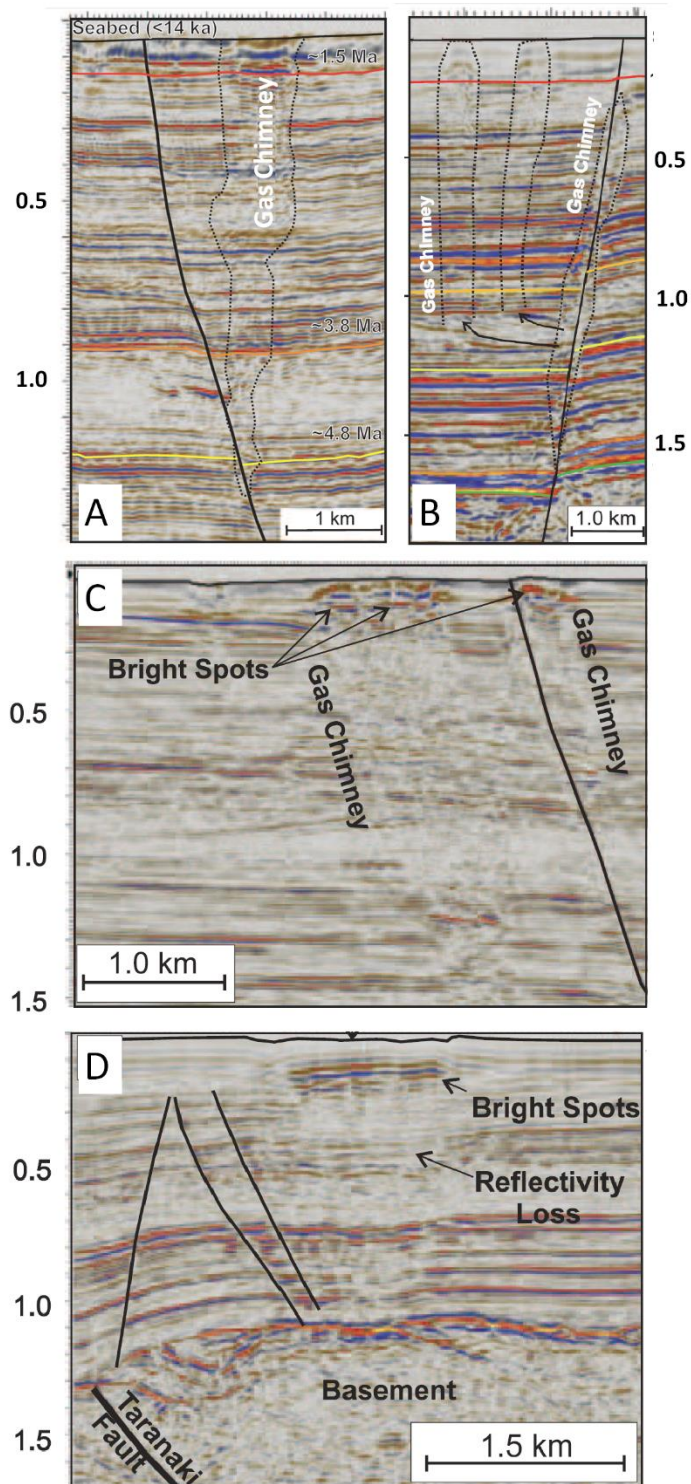
Figure 3-5: Examples of gas flow along normal faults in the southern Taranaki Basin (after Ilg et al., 2012). Vertical scale is in seconds TWT. A) and B) Cone-shape amplitude distortions along normal faults C) and D) Bright spots and reflectivity loss
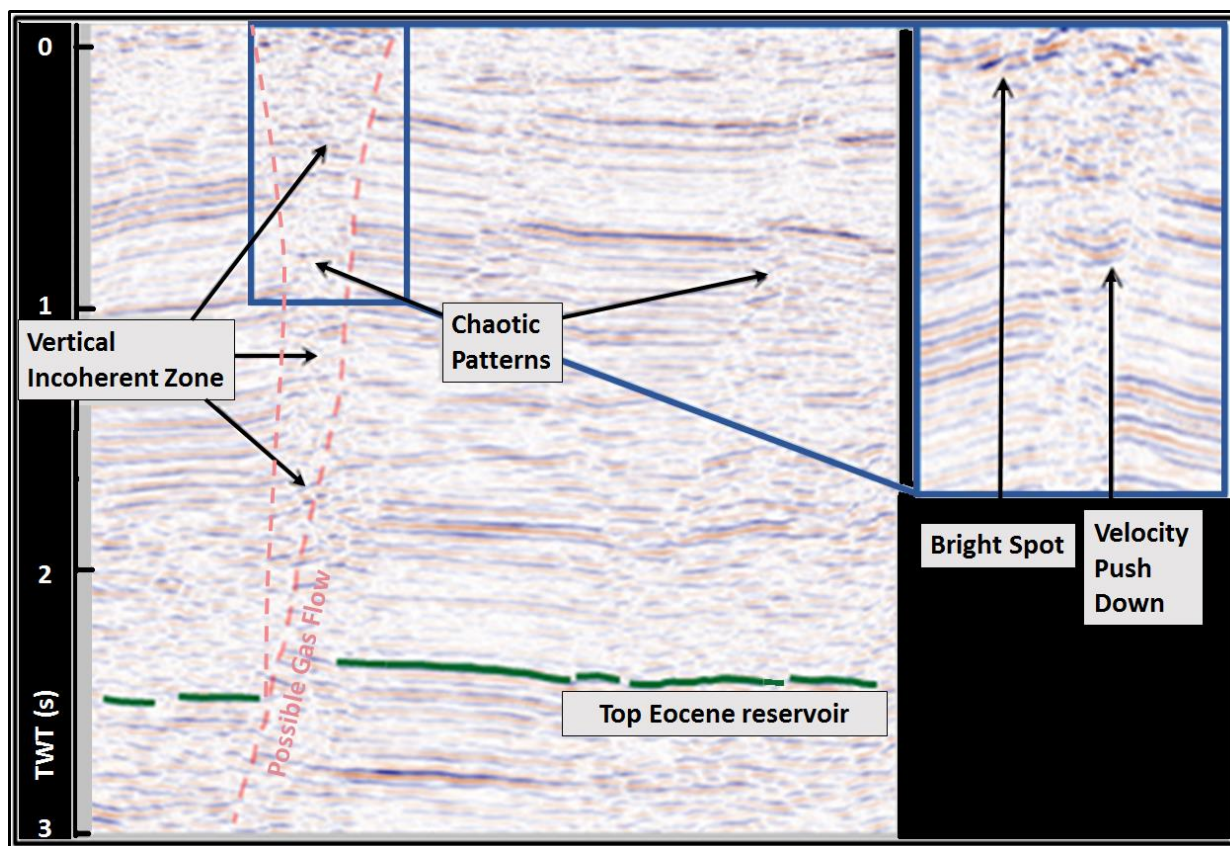
Figure 3-6: Interpretation of gas reflections on a vertical section. Possible gas flow pathway is indicated in bright red (appears as cone-shape incoherence). In green, estimated top Eocene sandstone reservoir which had hydrocarbon shows in Te Kiri-1 well. (modified after Alarfaj and Lawton, 2012)

3.3.5 Seismic Attributes

Seismic attributes are defined as information extracted from seismic data (Sheriff, 2002). Attributes can be directly measured or can be derived from a seismic volume and can serve as an interpretational tool for subsurface structure, stratigraphy, and reservoir properties. Brown (2011) classifies seismic attributes based on time, amplitude, frequency and attenuation.

Seismic attributes in this study were computed using *Rock Solid Attributes*™. Analysis of seismic attributes in the studied 3D volume were helpful for delineating some faults and

detecting possible gas presence. The most effective attributes are the ones that amplify the contrast between seismic responses caused by gas reflections and other non-gas related reflections.

Several useful attributes applied in this study were categorized by Taner (2001) as geometrical attributes. These attributes scan adjacent traces for each computed trace and describe the spatial and temporal relationships based on character such as phase, frequency, amplitude, etc. (Taner, 2001). Examples of these attributes are semblance, curvature, chaotic reflection, dip variance, dip of maximum similarity, and instantaneous lateral continuity. These attributes are referred to as "reflective attributes" which correspond to characteristics of interfaces between two beds. By understanding the characteristic response of acoustic waves passing through gas zones, leaky faults could be predicted by the output of seismic attributes. Two of seismic attributes are briefly discussed in the following two sections: semblance and curvature.

3.3.5.1 Semblance

Semblance measures how similar the energy from a number of stacked traces compared to the total energy of all traces in that stack. This is computed mathematically by (Taner, 2002):

$$\boldsymbol{Semb(t)} = \frac{\sum_{\tau=-N/2}^{\tau=N/2}\{\sum_{m=1}^{M}\boldsymbol{f_m(t+\tau)}\}^2 - \sum_{\tau=-N/2}^{\tau=N/2}\sum_{m=1}^{M}\boldsymbol{f_m^2(t+\tau)}}{\sum_{\tau=-N/2}^{\tau=N/2}\sum_{m=1}^{M}\boldsymbol{f_m^2(t+\tau)}} \qquad (2.3)$$

where $f_m(t)$ is the mth trace of the gather and N is the window length. This attribute allows for detection of lateral changes (i.e. discontinuities in a reflector's waveform) caused by structural, stratigraphic or chaotic features. It is a very effective tool in locating vertical faults offsetting coherent reflectors in seismic data. Faults are typically visualized better on horizontal attributes

sections. Figure 3-7 shows a horizontal section of semblance at the same time for the horizontal time slice shown in Figure 3-3. In stratal deformation where continuity of a reflector is maintained (e.g. fault drag or rollover), no major anomalies are usually shown in computed semblance.
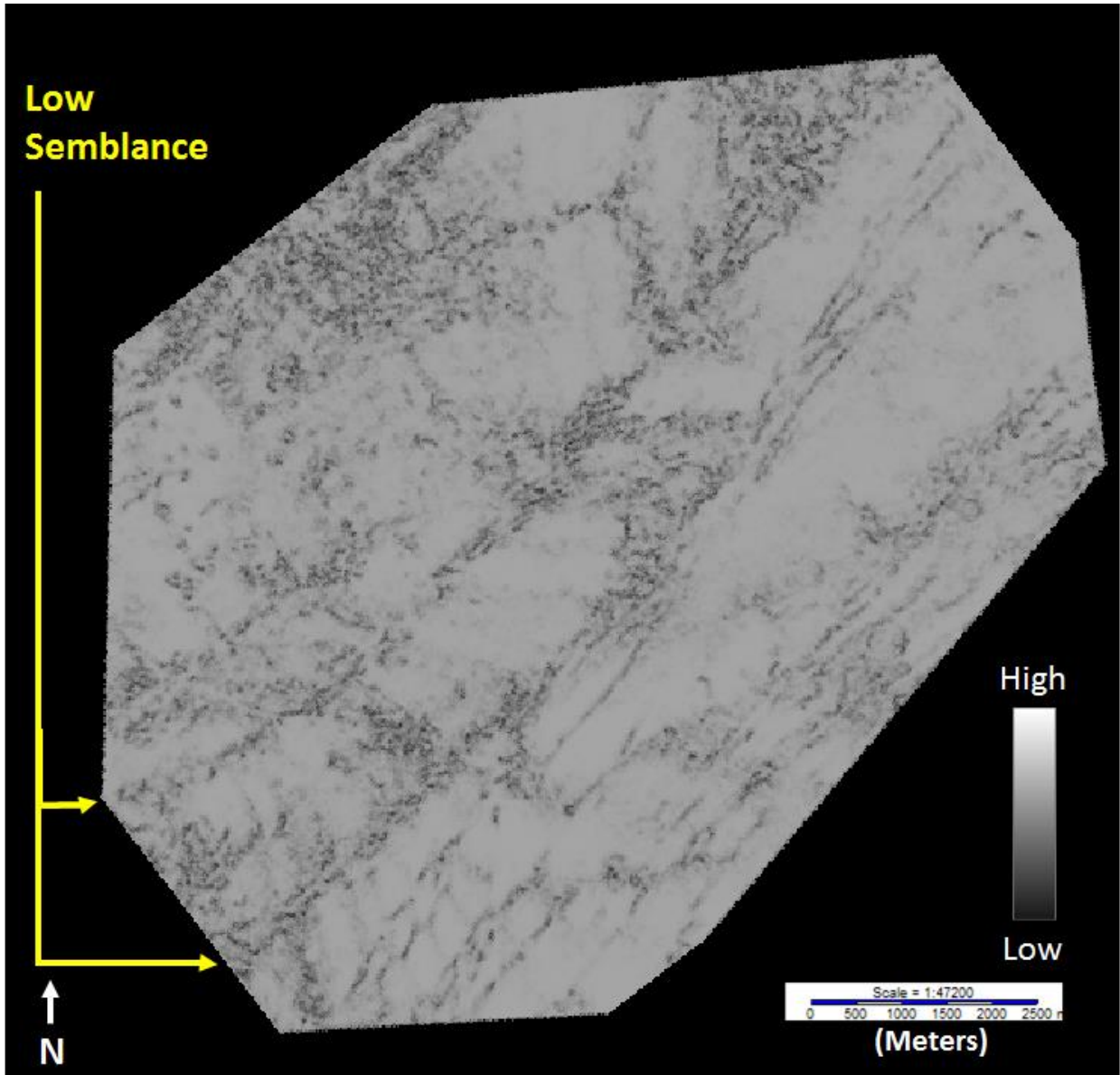

Figure 3-7: Horizontal section of semblance attribute at 810 ms TWT. Low semblance clearly delineate fault locations shown as amplitude terminations on Figure 3-3.

3.3.5.2 Curvature

Volumetric curvature is a second derivative of surface-derived attribute. It is a measure of deviation at a certain point from a straight line (Roberts 2001). Curvature is computed based on estimations of reflector dip and azimuth (Al-Dossary and Marfurt, 2006). A plane with a constant dip, for example, has zero curvature value. When dip is variable, curvature is non-zero. To compute curvature from a grid of measurements, an approximation method such as the least-squares fitting is used. Chopra and Marfurt (2007) and Roberts (2001) show more details of using the approximation method to fit a quadratic surface in the form of:

$$z(x, y) = ax^2 + cxy + by^2 + dx + ey + f \qquad (2.4)$$

where a, b, c, d, e, and f are coefficients computed from the values of grid nodes and the distance between these nodes.

Based on this approximation, computations are made to derive different curvature values such as maximum, minimum, mean, Gaussian, most positive and most negative curvatures. The latter two always show the same polarity for geologic events such as faults, folds and fractures (Chopra and Marfurt, 2007). Most-positive and most-negative curvature were used to detect the gas leakage along faults in this study. The most-positive curvature is calculated from the previous quadratic surface equation by:

$$K_{pos} = (a + b) + \sqrt{(a - b)^2 + c^2} \qquad (2.5)$$

and the most-negative curvature is calculated by:

$$K_{neg} = (a + b) - \sqrt{(a - b)^2 + c^2}$$ (2.6)

Figure 3-9 shows the most-postive curvature at 810 ms TWT. Note that the most positive values do not necessarly align with the fault location since curvature is a measurement of bends caused by and near the fault (rather than a displacement caused by the fault).
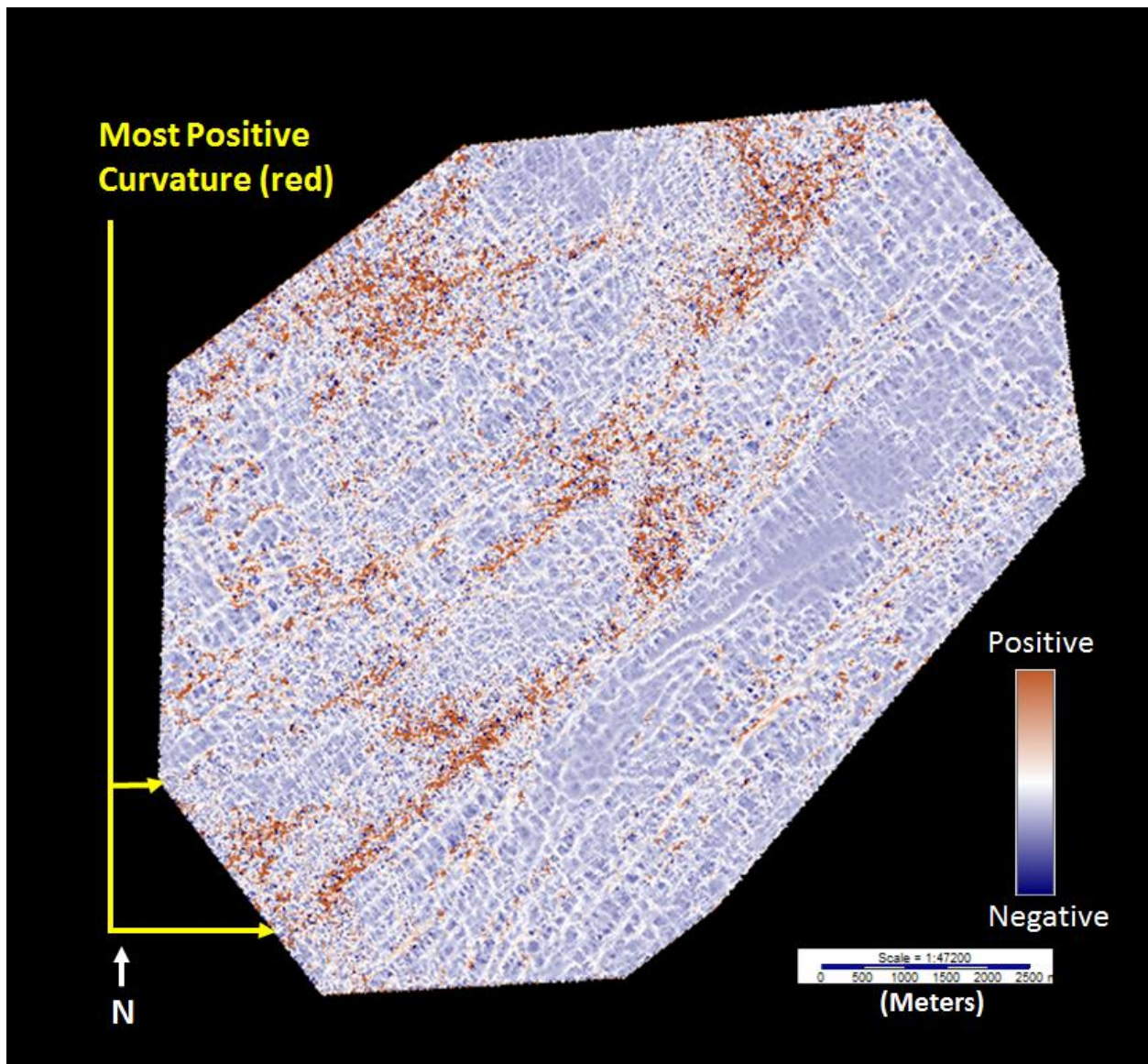
Figure 3-8: Horizontal section of most-positive curvature at 810 ms TWT.

3.4 Results and Discussion

Te Kiri 3D adequately image the shallow events in the subsurface. Figure 3-9 is a map of the seismic survey indicating the location of dip lines that are presented as an example to show some shallow faults along with the major fault in the area (Figure 3-10).

In general, Shallow events in the seismic volume, above three seconds, were clearly imaged with good signal to noise ratio. Interpretation of seismic images shows normal faulting dominating the shallow subsurface structure and corresponds to the geologic history of the region (previously discussed in Chapter two). The quality of data decreases with depth to the point where faults and horizons are untraceable. During the interpretation process, picks of both faults and horizons were made based on a geologic model in mind related to the geologic history of the region (discussed previously in Chapter two).

Figure 3-10 shows three of the interpreted horizons. The shallower horizons were interpreted to resemble the complex structure at their level and for modeling the major fault (discussed in chapter four). A deeper horizon was then interpreted to indicate the top of a proven gas reservoir (productive in Maui gas field) (King and Thrasher, 1996).
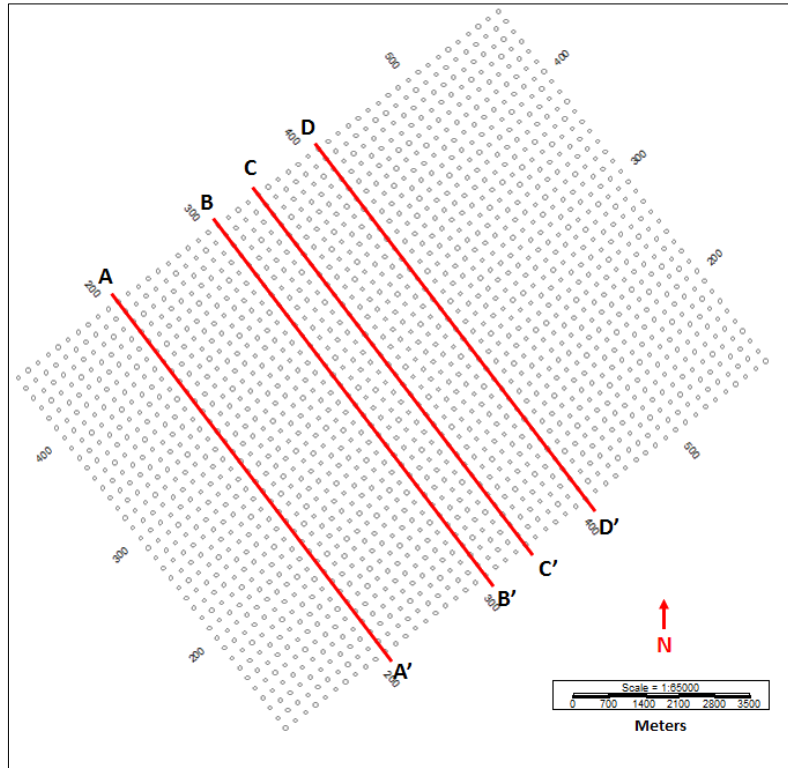
Figure 3-9: Map of the the 3D seismic survey showing locations of dip lines on Figure 3-10.

Major faults in this survey (e.g. Oanui and Kina faults) were interpreted to strike northeast-southwest. Structure maps indicate that some of the major faults cut through the two shallower horizons as well as the deeper one at the top reservoir level.
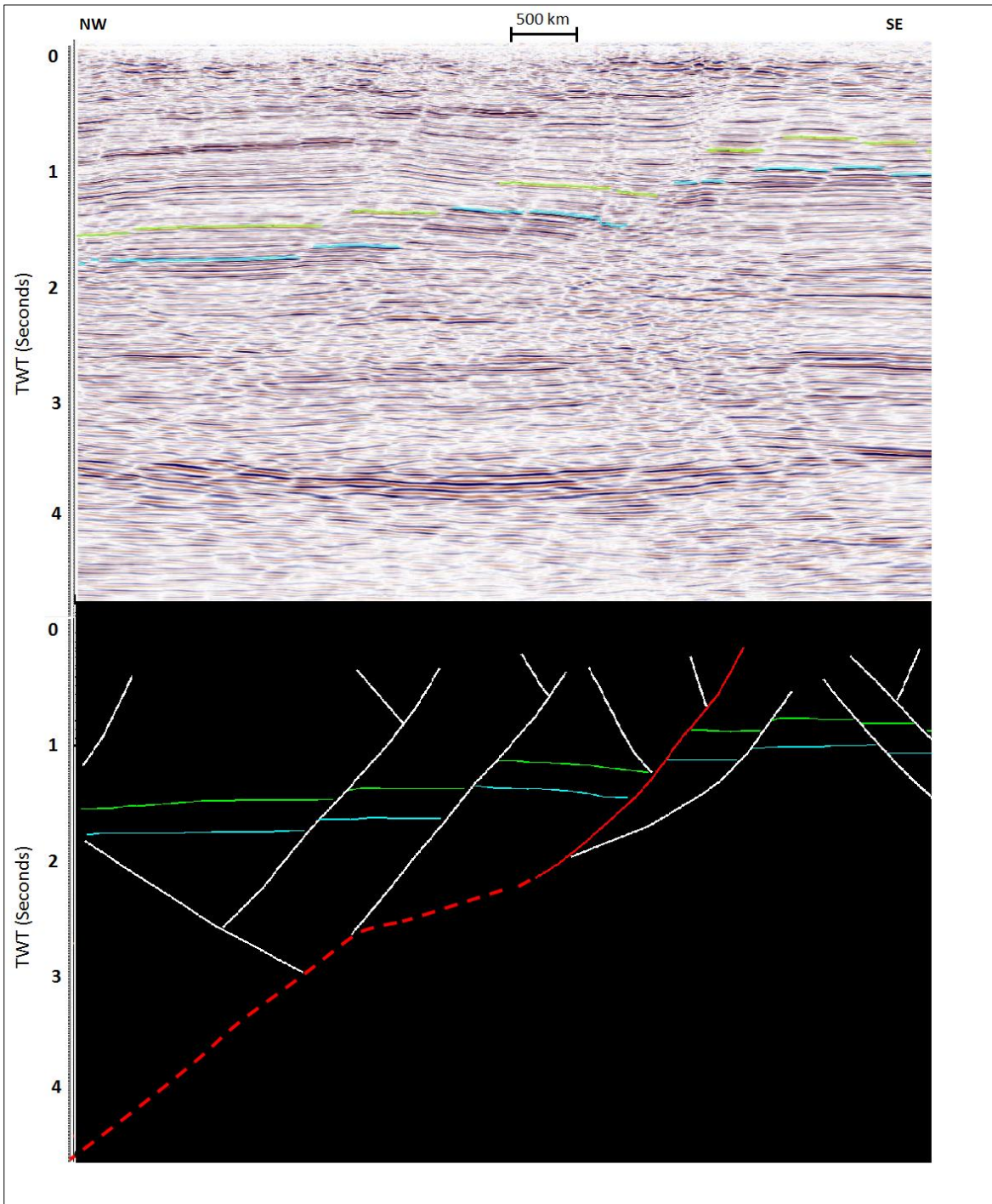
Figure 3-10a: Examples of dip lines showing some shallow faults along with the major fault in the area. Above is a seismic vertical section of line A-A' showing two observed shallow reflectors used for fault modeling in the following chapter. Below is an interpretation of the above section showing shallow faults (white) and the major fault (red). The dashed red line indicates the predict fault geometry by forward models.
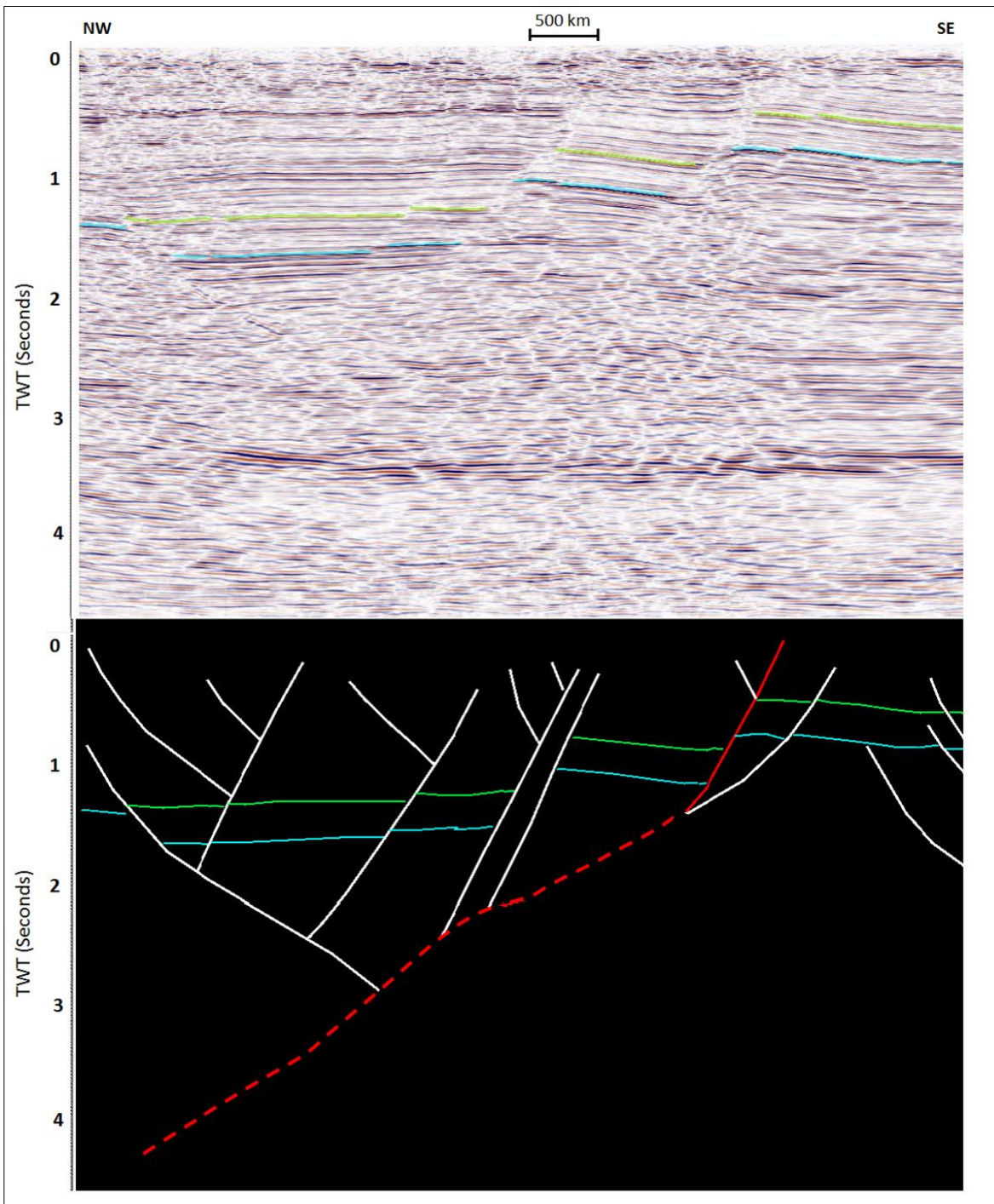
Figure 3-10b: Inline B-B' in Figure 3-9.

54
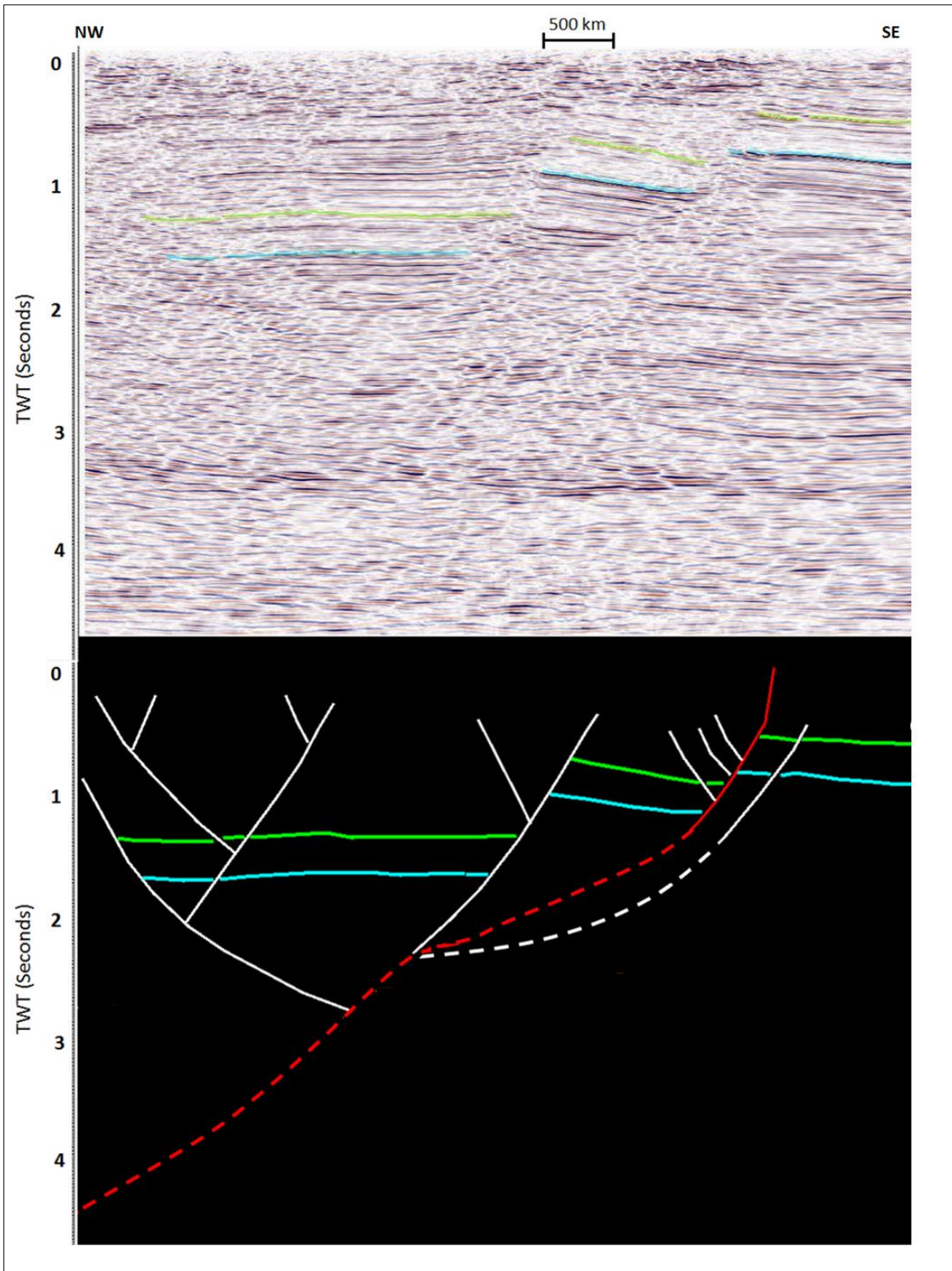
Figure 3-10c: Inline C-C' in Figure 3-9.
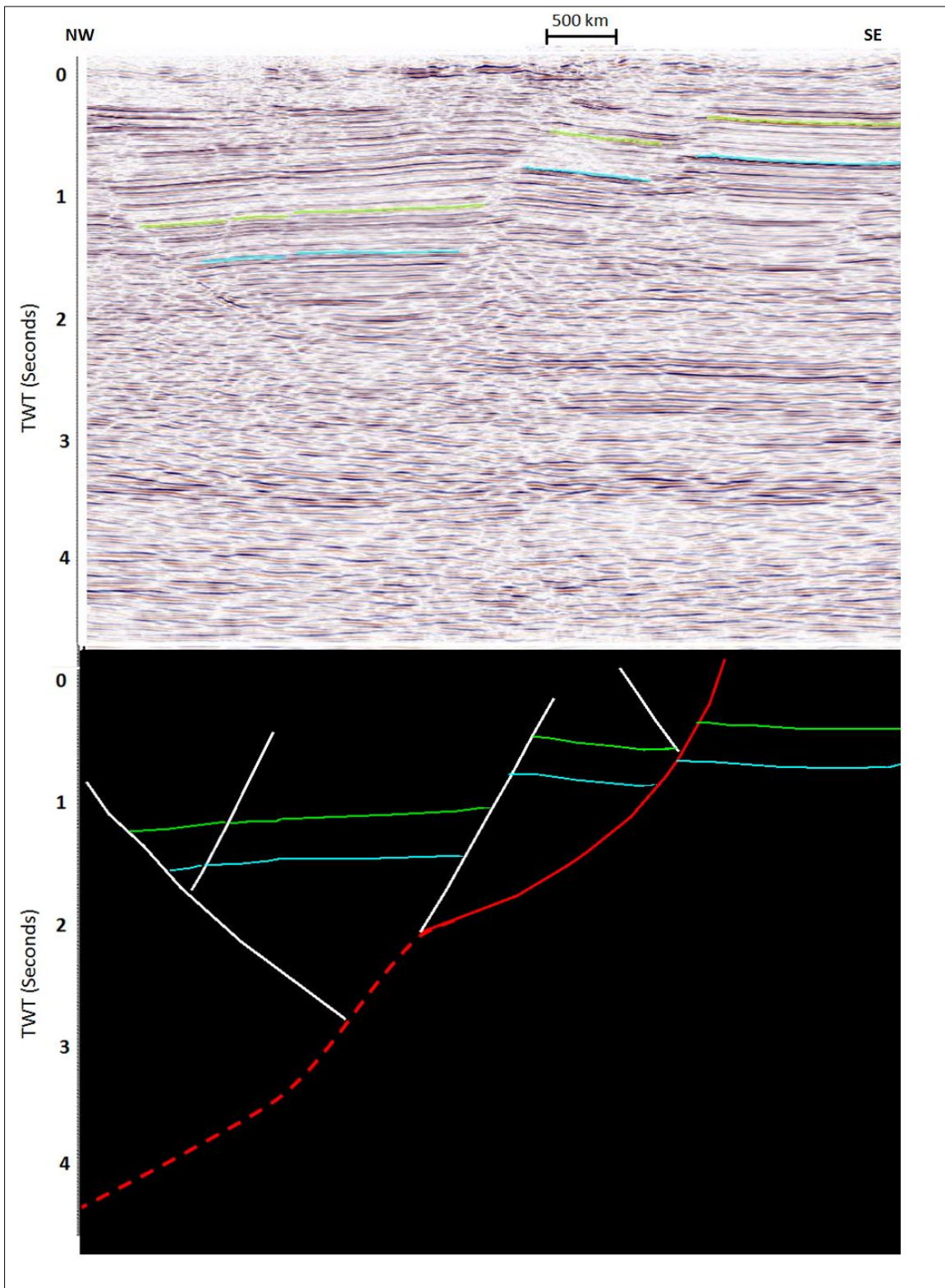
Figure 3-10d: Inline D-D' in Figure 3-9.

The faults appearing in the southern part of the survey in the shallower horizons are not shown in the deeper horizon map. This indicates that these faults are relatively younger in age occurred at a later geologic time. These younger faults are also striking northeast-southwest, but slightly more toward the north. This was interpreted to be caused by stresses applied later in geologic time. The forces exerted by these later stresses are at different direction than the previous stresses that created the older trend.

Another observation made in this survey is the evidence of erosion appearing in shallower events (~0.5 seconds) where faults seem to terminate. Reflections above faults terminations appear to be different than the surrounding events. Layers near this zone seem to truncate at that erosion level revealing what appears to be an unconformity. Bright spots are generally observed at different locations above the unconformity level. These bright spots could be caused by gas that traveled from deeper sediments through permeable faults in contact with the unconformity.

Interpretations of the seismic volume indicates lack of flower structures in the seismic volume. This can indicate the lack of major strike-slip movement which usually generates these flower structures (Suppe, 1985; Davis et al., 2012).

The tilted fault blocks observed in the seismic images can be the result of extension followed by stable subsidence in the area. Tilted half-graben in the hanging wall of the major fault indicate a listric behavior for the interpreted fault. Secondary faults (i.e. antithetic and synthetic faults) and their conjugates are also evident above the major fault in the seismic image. Secondary faults are typically observed above listric faults and they are associated with fault

bends (i.e. fault curvature) of an underlying major fault (more details are discussed in Chapter four).

Poor data quality at depth caused uncertainties in faults interpretation. Figure 3-9b shows where the faults are not easily traceable at deep reflections. The listric behavior exhibited by the major fault and its associated hanging-wall deformation leads to questioning whether the major fault's dip continues to decrease and flatten out somewhere above the basement, or if it actually continues to dip steeply and eventually cut through and offset the basement.

Published studies of this studied area show faults interpretation mostly above 3 to 4 seconds TWT. The geometry of the major fault, estimated from the structural kinematic forward models discussed in Chapter four, shows that the major fault actually continues to dip steeply at depth. We therefore propose that the major fault in this study is a basement-involved fault and does not flatten out at a shallower level above the basement (i.e. the major fault cut through the basement and the overlaying proven reservoir and source rock).

Faults can generally act as part of a hydrocarbon trapping mechanism when in contact with a hydrocarbon-filled formation. They can act as a migration path when permeable or as a seal when impermeable. Indications of gas presence along some of the interpreted faults, including the major fault, are evident in this studied seismic volume.

The presence of fault-related gas leakage is observed on vertical sections. Figure 3-9 shows an example view of the major normal fault cutting through the Eocene reservoir sequences. Associated with this fault is a zone of disrupted seismic reflections showing the gas leakage characteristics discussed previously. The root of this leakage zone seems to be originated

58

beneath the Eocene reservoir level. The leakage zone resembles a cone-shape chaotic response which appears as a zone of vertical incoherence extending almost to the surface. The gas leakage zone in general appears to exhibit relatively lower amplitude, whereas the top of the zone shows bright spots. Bright spots are high amplitudes caused by a strong drop in acoustic impedance and are often considered a direct indicator of gas presence.

The seismic response of the gas leakage zone appear to be distinguished on seismic attributes (Figure 3-10). The effects of acoustic waves traveling through low velocity gas zones are shown as disruptions in coherency of the data. This translates to very low semblance values along the gas leakage zone. Disrupted signals also result in high values of the curvature attribute (Figure 3-11). This can be due to changes in geometric local dips as a result of scattering within the gas leakage zone. The dip changes can be evident on dip variance attributes (Figure 3-12).

The gas presence in the seismic volume is observed to fall generally within the extreme ends of certain attributes' spectrum. For example, the leakage zone was represented by the lowest semblance (Figure 3-10) and highest curvature values (Figure 3-11). This can be particularly useful when it comes to observations for the distribution of possible gas presence along faults in the survey. When attribute values are analyzed, they can be filtered based on a certain threshold value by opacity removal. This allows for showing only the seismic attribute values interpreted to be caused by gas presence along the interpreted faults.

Figure 3-12 show an example of filtered values of overlaid on conventional amplitude sections. The opacity removal should be determined by analysis of several sections at leakage zones from different locations and can be overlaid on a horizontal slices to indicate the

distribution of potential gas leakage in the survey. It is important to check the quality of the results since the displayed values depends on the interpreter's observation and judgment.   For example, a too high cutoff choice for opacity removal of the semblance attribute can possibly result in including values caused by low similarity values across a fault displacement rather than values caused by the gas presence.
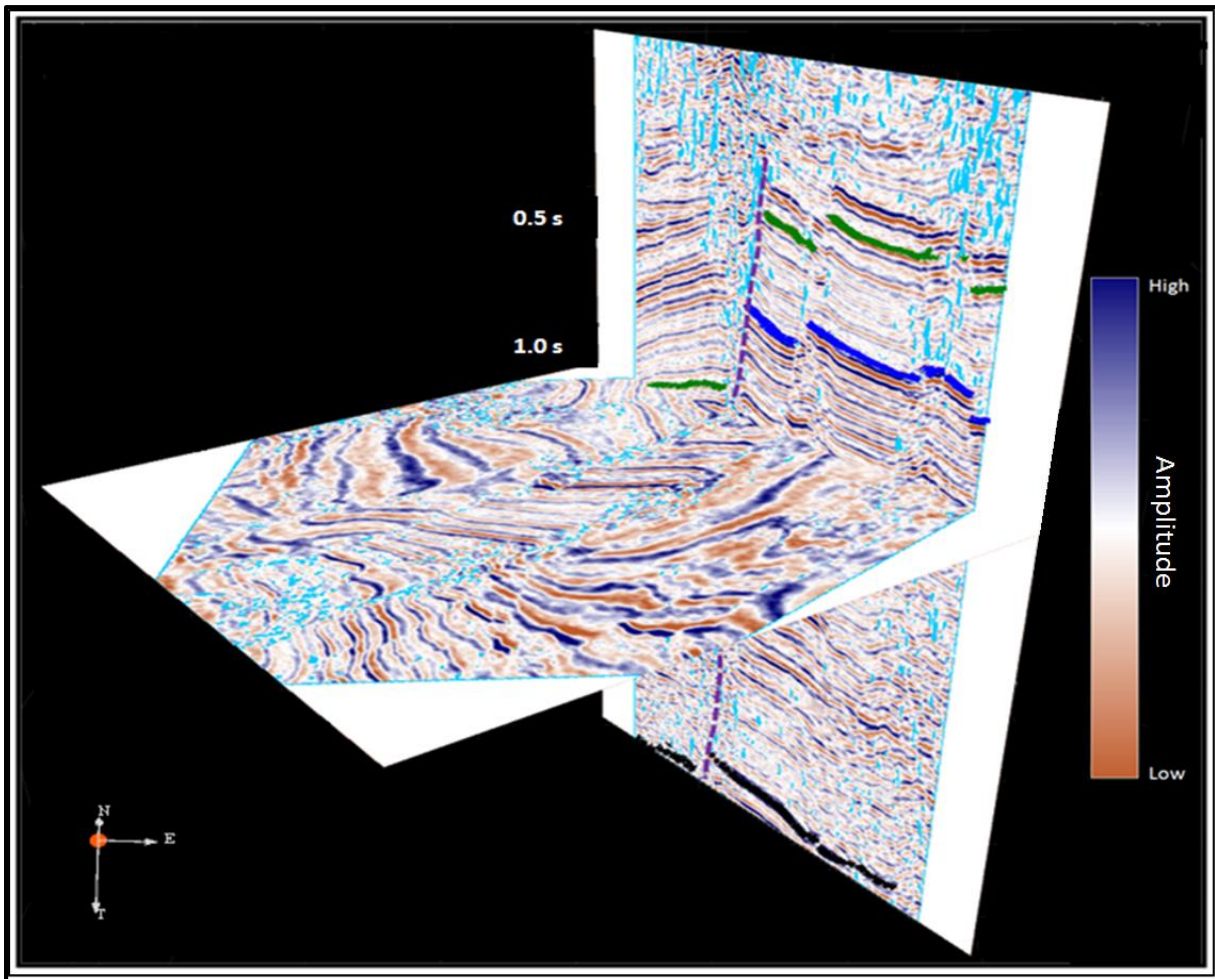
Figure: 3-10: Distribution of low semblance (light blue) superimposed on amplitude sections. These values predict the location of leakage-like response. Higher semblance values were filtered (transparent). Leaking normal fault (purple) was interpreted to cut through the top of reservoir (black) and two other interpreted horizons (blue and green).
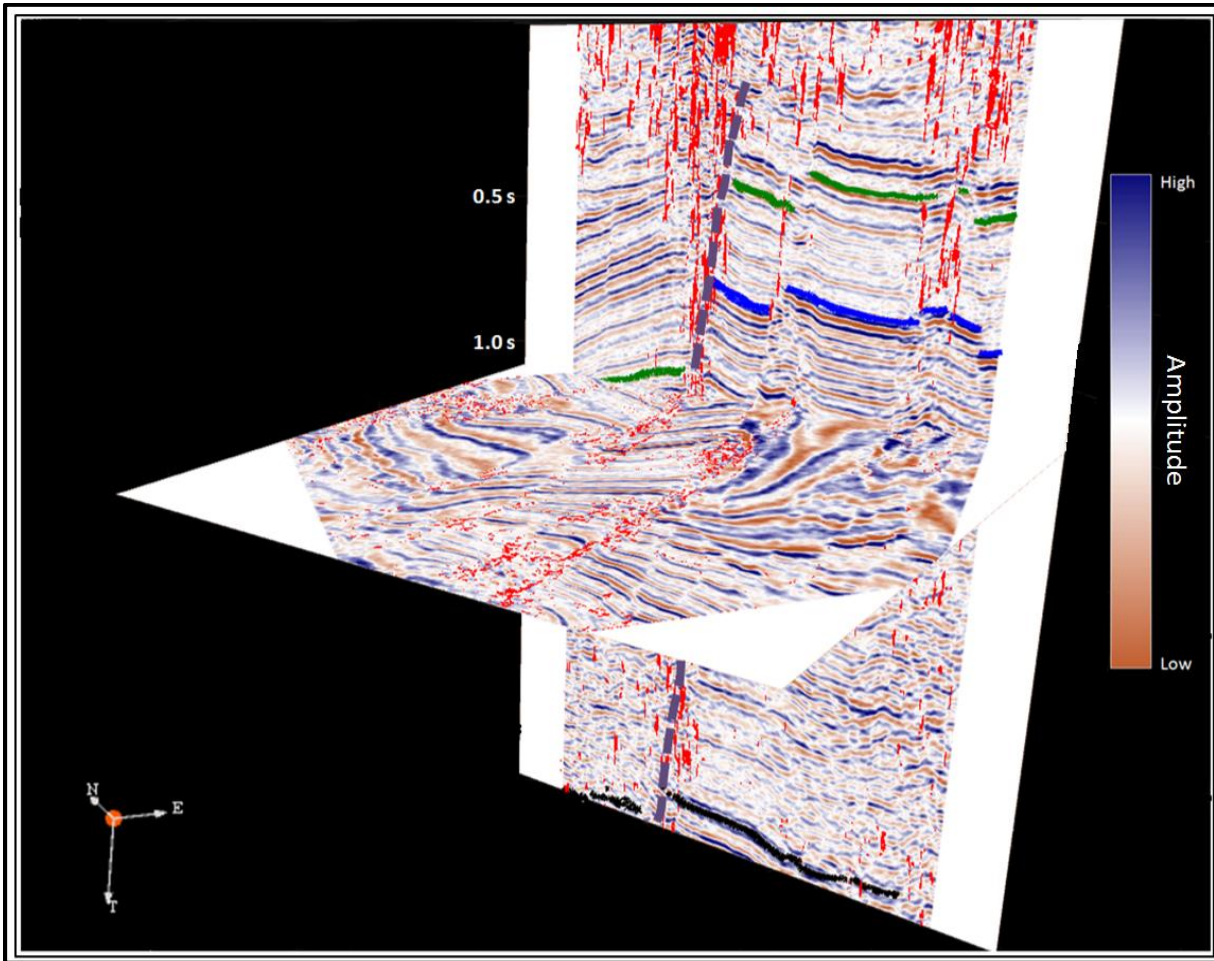
Figure 3-11: High values of most-positive curvature (red) overlaid on amplitude sections. These values predict the location of leakage-like response. Lower curvature values were filtered (transparent). Leaking normal fault (purple) was interpreted to cut through the top of reservoir (black) and two other interpreted horizons (blue and green).
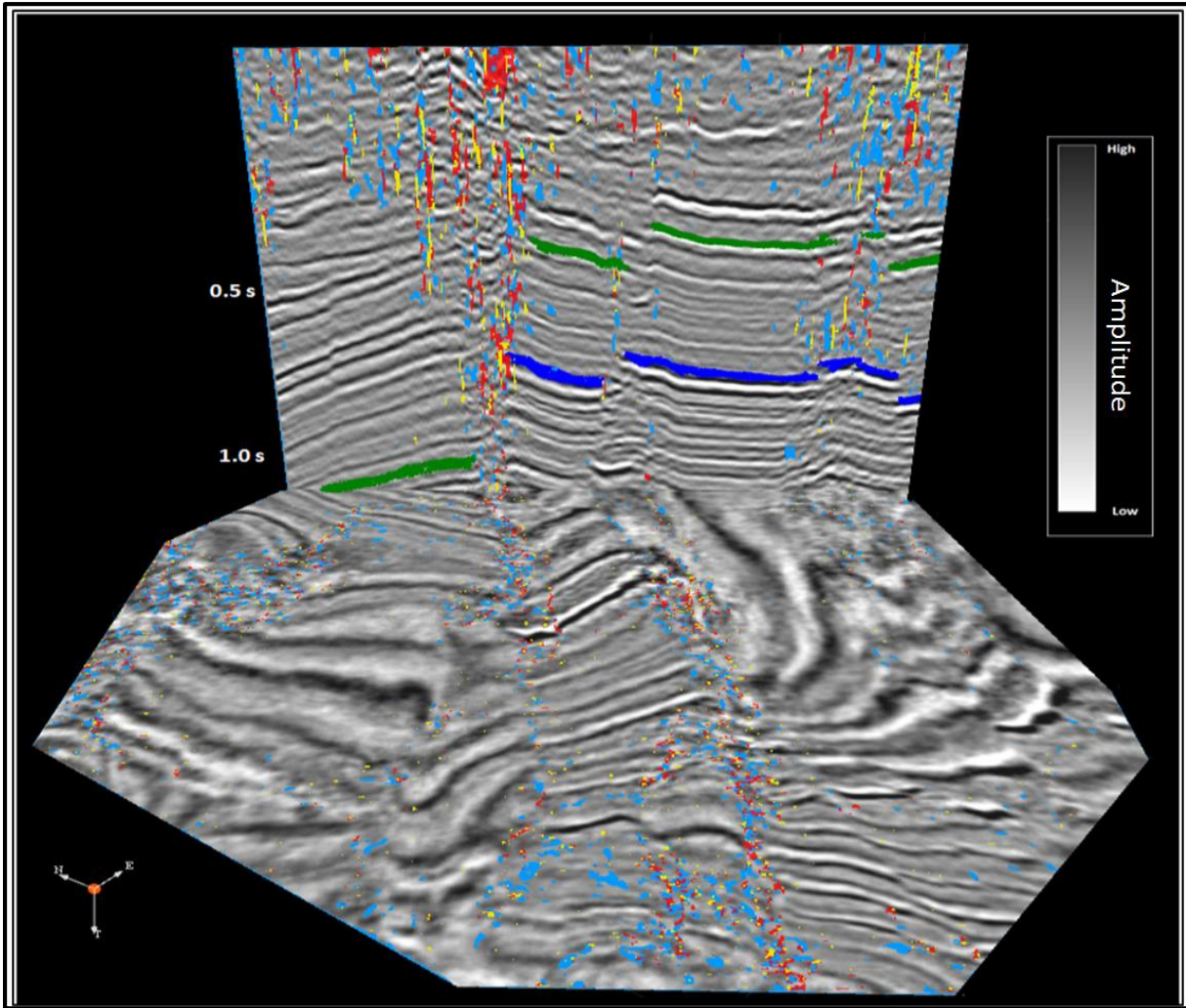
Figure 3-12: multi-attributes overlaid on vertical and horizontal amplitude sections to predict leakage locations. Filtered values are shown for semblance (light blue), most positive curvature (red) and most negative curvature (yellow). The more attributes shown within the same locality, the higher is the chance for gas presence.

Since computations of different attributes follow different algorithms, it is possible that non-leakage related response showing in one attribute is avoided by another. Therefore, we observed that when opacity removal of multiple seismic attributes are applied and overlaid on each other, a better estimate of the leakage distribution can possibly be presented (Figure 3-12).

More values of different computed attributes shown at a given location can indicate a higher chance of gas presence at that location.

Utalizing different seisimc attributes can be integrated using neural networks to detect gas presence in a seismic volume. Meldahl et al, (1998) and Aminzadeh et al (2001) describe a developed multi-attributes approach for pattern recognition though neural networks. The use of multi-attributes has proven to be effective in detecting geologic features such as gas chimneys. This method require several picks for chimney and non-chimney samples. If interpreters have access to a neural network software, a better estimate is possible for detecting the locations of gas presence (e.g. seismic gas chimneys).

Deformations associated with faults in the interpreted seismic volume are mainly due to dip-slip movements rather than strike-slip movements (indicated by the lack of flower structures in the interpreted seismic volume and from the geologic history of the region previously discussed in Chapter two). We therefore propose the loss of image across a fault's cutoffs in the interpreted seismic volume to be caused by the presence of gas rather than distributed strain caused by strike-slip movement.

3.5 Summary and Conclusions

Te Kiri 3D reveals a complex structure dominated by normal faults. Major faults are mapped and shown to be generally striking northeast-southwest. Interpretations of this survey show evidences of the diverging history of the subsurface. Possible gas leakage is identified along some of the interpreted faults in Te Kiri 3D. The interpretation of gas presence is supported by observations of amplitude anomalies and incoherent reflections within the leakage zone. Attributes such as semblance and curvature are helpful in detecting unique responses

63

caused by gas presence. The opacity removal is a helpful visualization tool that can assist in detecting and delineating the gas-leakage distribution in the survey.

The evidence of possible gas migrating up-sequence in the seismic image is linked to the interpreted faults that might cut through a hydrocarbon-filled formation. These faults are typically not visible at the deeper poorly imaged reflections in the survey. It is therefore essential to predict a fault's geometry at depth and determine whether or not that fault is in contact with the deep proven reservoir.

The geologic history of the region along with the lack of flower structures in the interpreted seismic volume indicate that deformations associated with faults are mainly due to dip-slip rather than strike-slip movements. The lost of seismic image across faults' cutoffs, is therefore due to the presence of gas rather than distributed strain caused by strike-slip movement.

Chapter Four: Kinematic Structural Forward Modeling for Fault Trajectory Prediction in Seismic Interpretation

4.1 Introduction

One of the main objectives of this dissertation is to examine the geometry of normal faults from seismic images where these faults may not be very visible. In this chapter, we create kinematic forward models based on the rollover theory of Xiao and Suppe (1992) and extensional balancing concepts of inclined shear deformation. Implementation and model development were undertaken using recently released structural modelling software, STRUCTURESOLVER, made available to this project. All the created models are balanced (i.e. cross sectional area is preserved). The kinematic forward models describe how the geometry of a normal fault is related to its hanging-wall strain. Deformation resulting from movement of hanging-wall block along non-planar normal faults (e.g. listric growth faults) can be analyzed by generated rollover structures in the downthrown of that non-planar fault.

In this chapter, we address controlling variables affecting hanging-wall deformation, including the fault geometry, amount of sedimentation, slip ratio and shear angles. We then create kinematic forward models to estimate the trajectory of the Oaonui Fault at depth where seismic reflections are poorly imaged.

4.2 Background

Rocks, when undergoing deformation, flow, bend or, in the case of faults, slip. Mapping faults is crucial in hydrocarbon exploration and production as faults can act as a sealing mechanism for a potential trap, or a conduit for fluids in tight formations. Faults are inferred in the subsurface by seismic imaging which is an indirect representation of the subsurface measured

in two-way time. Seismic imaging is often associated with signal distortion and limitations in temporal and spatial resolution. Seismic data may be subject to misinterpretation since it is an approximation of the subsurface and is at best, only a representation of the true geology.

Interpreted seismic reflections are based on the acoustic seismic response which resembles differences in impedance between different earth materials. Continuous reflections are typically interpreted as horizons representing stratal surfaces, whereas discontinuities are interpreted to represent fault displacements or unconformities. Many efforts have been made to automate fault tracking based on reflection discontinuities. Examples are algorithms such as semblance, which is a continuity measurement (Marfurt et al., 1998), variance, a discontinuity measurement (Randen et al., 2001) and most recently an extraction method based on fault surface computation and extraction (Hale, 2013). Despite the advancements made in autopicking algorithms, not all discontinuities are caused by faults. Reflection terminations can be caused by stratigraphic features such as unconformities or by imaging artifacts (Herron, 2000). Furthermore, subsurface structures maybe invisible or mis-positioned on imaged sections (Lawton and Isaac, 2001). As a result, seismic interpretation often requires validation tools to properly understand the true subsurface structure and generate better prospects.

4.3 Kinematic Structural Forward Modeling of Hanging-wall Rollovers

Kinematic balanced forward models can provide geologically reasonable solutions to seismic images by extrapolating known data (e.g. well-imaged shallow seismic reflectors) into ambiguous data (e.g. poorly-imaged deep seismic reflections). Specifically, in extensional settings, where normal faults dominate the Earth's crust, inclined simple shear modeling can predict a distinct relationship between a fault shape and its hanging-wall deformation. This

relationship has been analyzed by physical modeling (e.g. Cloos, 1968; McClay and Ellis, 1987) and quantitative studies (e.g. Gibbs, 1983; White, 1986; Rowan and Kligfield, 1989; Groshong, 1989; Dula, 1992; Nunns, 1991; Xiao and Suppe, 1992). Dula (1991) compared different algorithms of kinematic modeling showing the inclined-shear model to be the most realistic. Xiao and Suppe (1992) further explained the concept of how the geometry of a deformed hanging wall is controlled by the shape of the fault.

Hanging-wall rollover is a type of fault-bend fold, generated by bending of hanging-wall blocks during movement along fault bends (i.e. nonplanar faults) (Suppe, 1985). Rollover is sometimes referred to in the literature as reverse drag and typically considered an important location of hydrocarbon accumulation (Suppe, 1985). The concepts of the rollover define how hanging-wall strata deform along active axial surfaces by coulomb shear collapse (e.g. Xiao and Suppe, 1992).

4.3.1 Coulomb Shear Collapse

In extensional tectonic regimes, the hanging-wall block of a planar fault subsides with a displacement vector parallel to the fault surface. In the case of a non-planar fault consisting of two fault segments or more, the hanging-wall block is moved by different displacement vectors during slip. If the hanging-wall block was purely rigid, a void would be created between the hanging-wall and footwall-wall blocks due movement along the lower fault segment below the fault bend (e.g. Hamblin 1965, Xiao and Suppe, 1992) (Figure 4-2b). However, in reality, beds overlaying this void would collapse due to gravitational forces and instantaneously fill the void (Figure 4-1d). This collapse occurs in the Coulomb shear direction, known the Coulomb collapse (Suppe 1985 and Xiao and Suppe, 1994), which is dipping 65-70° without the impact of

compaction (Xiao and Suppe, 1989). Collapsing hanging-wall beds deform and rollover due to shearing along *active axial surfaces* (Figure 4-2c, d). The active axial shear surfaces form at fault bends and are fixed at depth to the footwall cutoffs of those bends. Collapsing hanging-wall beds create secondary normal faults parallel to the active axial surfaces and these faults are usually visible on seismic images.

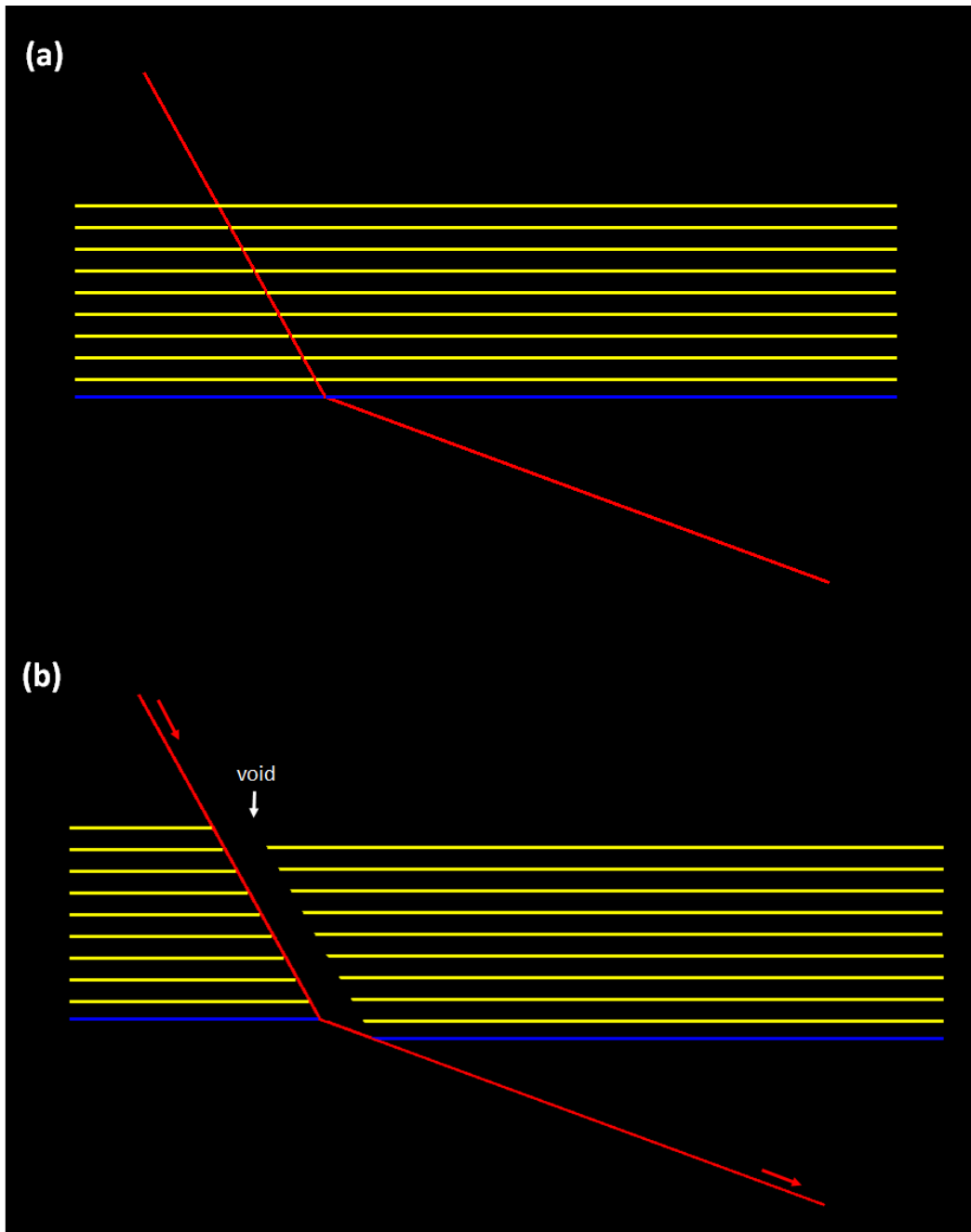**Figure 4-1: A movement over a concave-upward fault bend causes hanging-wall strata to collapse instantaneously along an active axial surface to fill a void created by extension. (a) Pre-faulting state (b) Void created by extension (c) The active axial surface is pinned at the FWC of the fault bend (d) Deformed beds (grey) after passing through the active axial surface.**
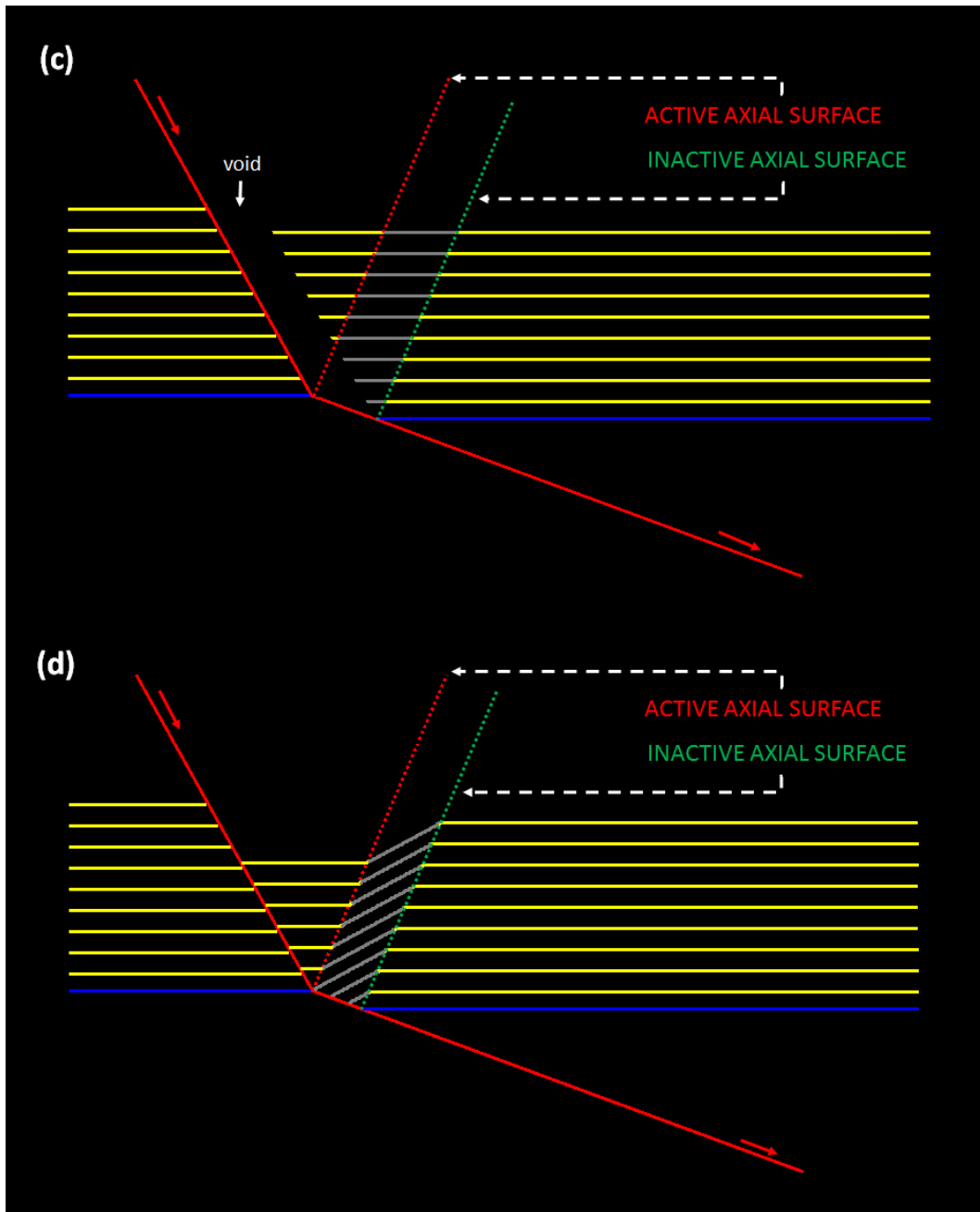
Figure 4-1: (continued)

4.3.2 Deformations along Concave and Convex Fault Bends

To illustrate the deformation mechanism along axial shear surfaces, we model a normal fault with a single concave-upward fault bend (Figure 4-2). In this case, an associated active shear axial surface forms at the fault bend at which hanging-wall beds collapse antithetically. The position of the active antithetic axial surface remains fixed at the footwall cutoff of the concave-upward fault bend (e.g. blue horizon footwall cutoff in Figure 4-2). As hanging-wall beds in the upper fault segment move over the fault bend due to slip, they deform as a result of passing through the active antithetic shear axial surface. Deformed beds fold around the active shear axial surface (i.e. rollover) and dip toward the fault surface, resulting in a graben-like structure next to the lower fault segment (grey beds in Figure 4-2).

Figure 4-2: (a)-(e) Sequential stages of deformation over a concave-upward fault bend. Grey lines indicate deformed hanging-wall beds within a kink band.

Figure 4-2: (continued)

In the case of a convex-upward fault bend (figure 4-3), an associated active shear axis forms at the fault-bend, at which hanging-wall beds collapse synthetically. Figure 4-3 shows a synthetic active shear axis modeled in a single-bend fault. Hanging-wall beds in the lower fault segment (i.e. below the bend before faulting) remain undeformed since they do not pass through the active shear axis. When layers move over a convex-upward fault-bend (Figure 4-4), the

position of the active synthetic axis remains fixed at the footwall cutoff of the fault bend (e.g. the blue horizon footwall cutoff in figure 4-3), and beds passing over that fault bend collapse synthetically along the active shear axis causing the beds to dip away from the fault.

The boundary between the deformed and undeformed beds in the lower fault segment defines the position of an *inactive axial surface*. This inactive axial surface remains parallel to the active axial surface in all stages of deformation. In an undeformed state (i.e. prior to faulting), active and inactive axial surfaces are aligned in the same position at the fault bend (Figures 4-3a and 4-4a). The inactive shear axial surface terminates in the hanging-wall cutoff at the fault bend prior to slip and moves with the hanging-wall block along the fault surface during slip (e.g. blue horizon hanging-wall cutoff at fault bend in Figures 4-3 and 4-4).
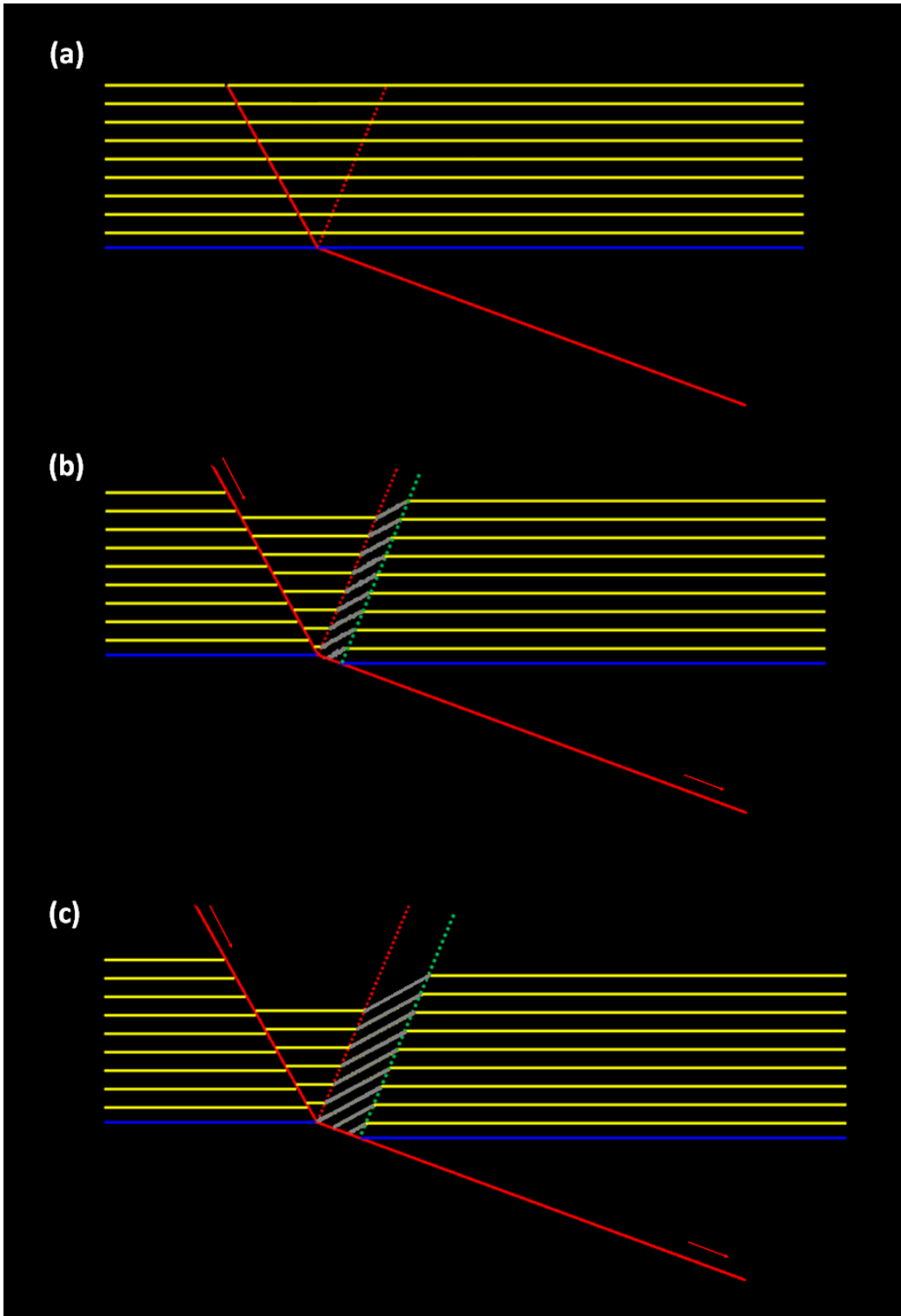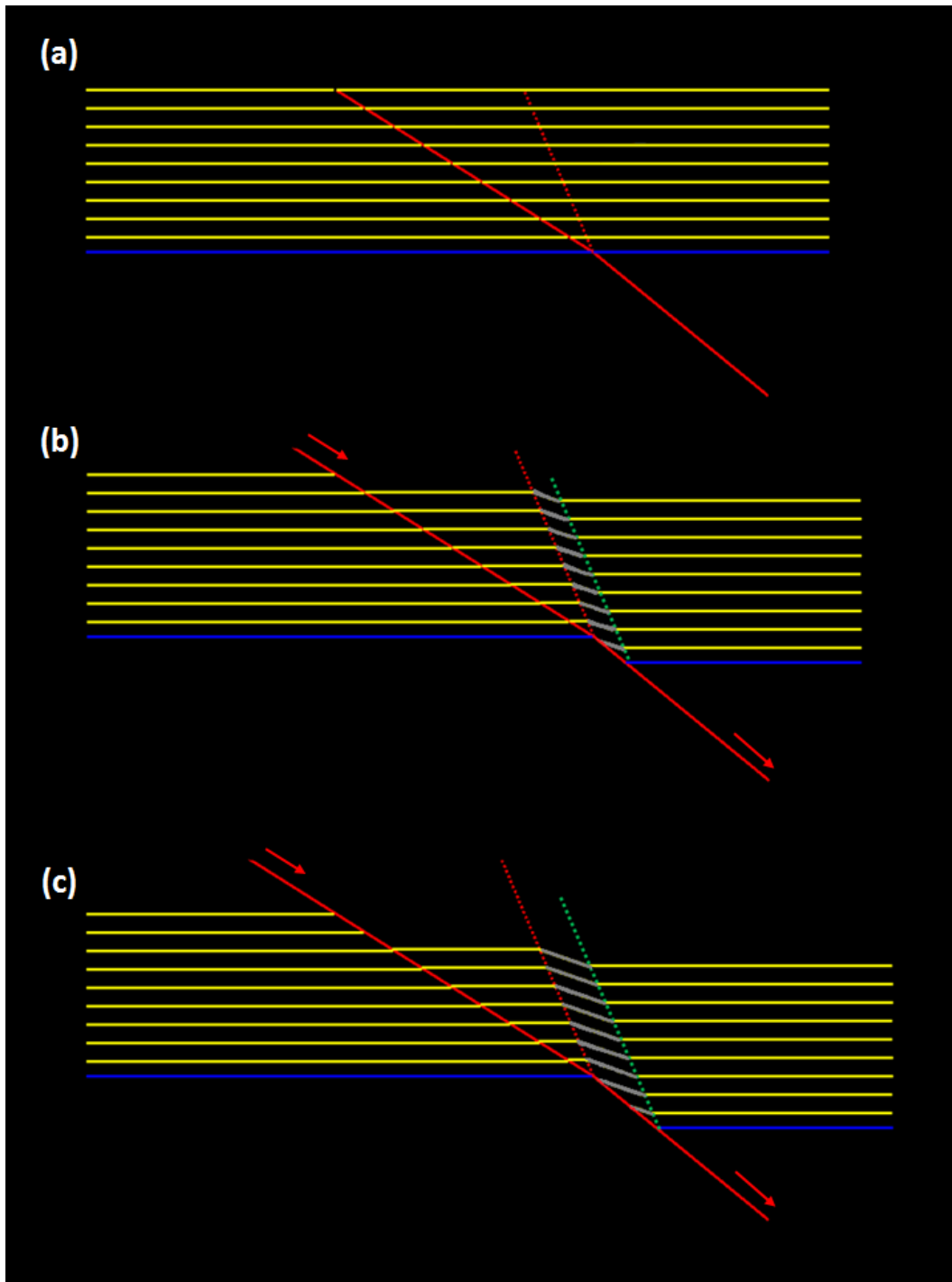
Figure 4-3: (a)-(e) Sequential stages of deformation over a convex-upward fault bend. Grey lines indicate deformed hanging-wall beds within a kink band.
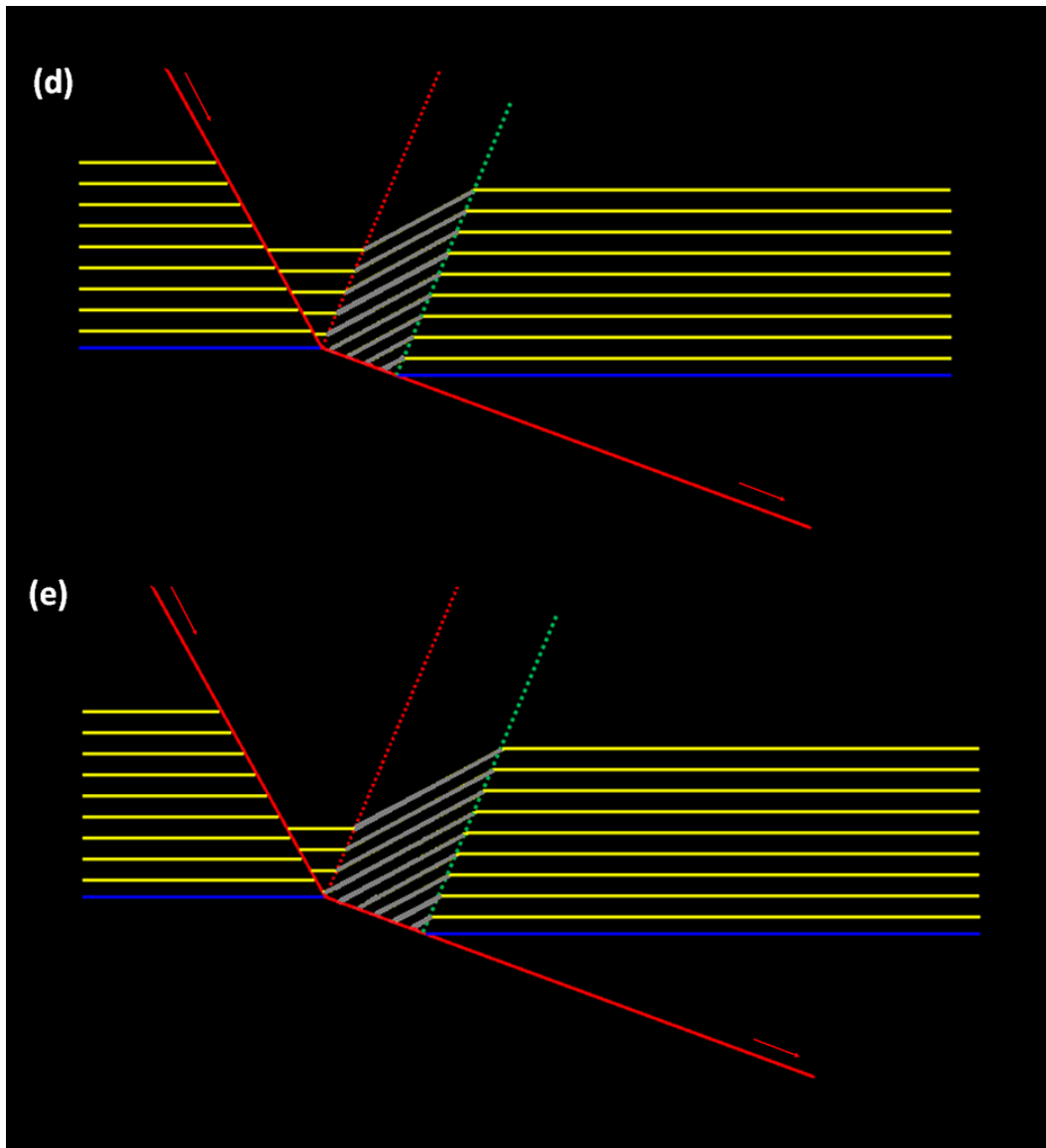
Figure 4-3: (continued)

4.3.3 Deformation zone

The active and inactive shear axial surfaces form together a *kink band* which

encompasses a deformation zone. Suppe (1985) defines this kink band as a discrete zone within

which the beds have been deformed and rotated relative to their geometry outside this zone. The

axial surfaces bounding this deformation zone are called *kink-band boundaries*.

The geometry of kink bands are defined by two angles (Suppe, 1985). The first is the

external kink angle (γ) between the active axial surface and the undeformed beds (i.e. beds that

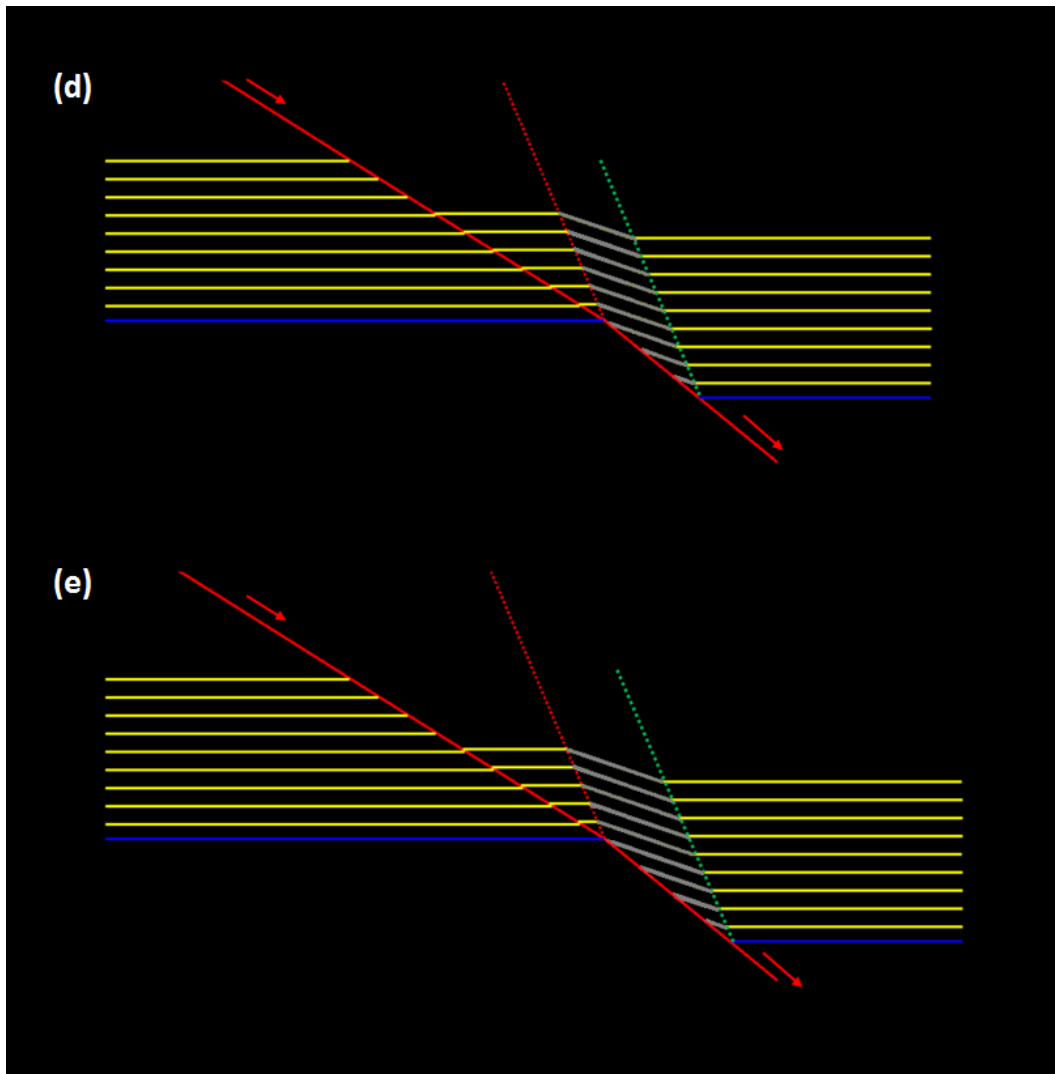have not passed through the active axial surface). The second angle is the *internal kink angle* (γ_k)

between the deformed layers within the kink band and the active axial surface., the possible

value for the external kink angle (γ) ranges between 0° to 90° and for the internal kink angle (γ_k)

ranges between 0° and 180°. However, in real Earth structures, Suppe (1985) states that the most

common values for the external kink angle (γ) is between 50° and 65°, whereas the internal kink

angle (γ_k) is typically between 75° and 85°.

The width of this deformation zone within the kink band is proportional to the fault slip

(i.e. the distance between the active and inactive axial surfaces equals the slip along the fault

surface). As slip increases, the deformation zone widens. All deformed beds, which passed

through the active axial surface, are contained within this zone. As hanging-wall layers slip along

the fault surface, new accommodation space is created above subsiding hanging-wall allowing

new sediments to be deposited.

4.3.4 Syn-tectonic Deposition

Deposition during faulting creates growth strata (Figure 4-4). Stratigraphic thicknesses in

the downthrown hanging-wall beds increase in growth faults (i.e. during syn-depostional

processes). The model shows growth beds (white horizons in Figure 4-4) are thickest in the

graben-like structure above the steepest fault segment. Similar to pre-growth beds, growth

deposits start to collapse and deform resulting in a monoclinal rollover as they pass through the

active shear axis, which remains stationary throughout all stages of deformation. In contrast,

growth sediments that did not pass through the active shear axis remain undeformed (i.e.

77

deposited to the right of the active shear axis or in the footwall). The position of the inactive

axial surface varies within the growth section depending on the expansion ratio, which is directly

determined by sedimentation and slip rates (Xiao and Suppe, 1992; Spang and Dorobek, 1998).

As a result, the dip of the surface connecting the active and inactive axial surfaces varies as the

expansion rates of beds change. This connecting surface is called *growth axial surface* (purple

dashed line in figure 4-4) and is created when the syn-depostional sedimentation rate exceeds the

slip rate; i.e. accommodation space above pre-growth beds is overfilled (Spang and Dorobek,

1998). The growth axial surface along with the fault and the two shear axial surfaces define a

deformation zone within which all deformed beds are contained. Growth axial surfaces can

sometimes be interpreted on seismic sections at the upward terminations of secondary antithetic

and synthetic faults in the hanging wall (e.g. Shaw et al., 1997; Spang and Dorobek, 1998). For a

given fault shape, the dip of growth axial surface is directly proportional to the amount of

sedimentation and inversely proportional to the slip and expansion rate. More specifically, the

growth axial surface can develop a curvature that is concave-up with increasing overfill

sedimentation rate and convex-up with decreasing overfill sedimentation rate. The growth axial

surface in figure 4-4 (purple dashed-line) is straight because it was modeled at a constant slip-to-

sedimentation rate. More on growth axial surfaces is discussed by Xiao and Suppe (1992), Shaw

et al. (1997), and Spang and Dorobek (1998).

Coarser sediments tend to be deposited in the graben-like structure above the steeper fault

segment, while growth sediments deposited within the rollover tend to thin toward the crest of

the rollover (i.e. near the growth axial surface) (Xiao and Suppe, 1992; Shaw et al. 1997). A

potential hydrocarbon trap may exist after a growth structure is developed. Therefore, the

interpretation of the growth axial surface is important in predicting targeted stratigraphic traps as

well as mapping facies changes (Tearpock and Bischke, 2002). In addition, a potential

hydrocarbon trap may exist after a growth structure is developed. Therefore, the interpretation of

the growth axial surfaces is also important in prospect generation as hydrocarbon traps do not

exist before the growth structure is developed (Tearpock and Bischke, 2002).
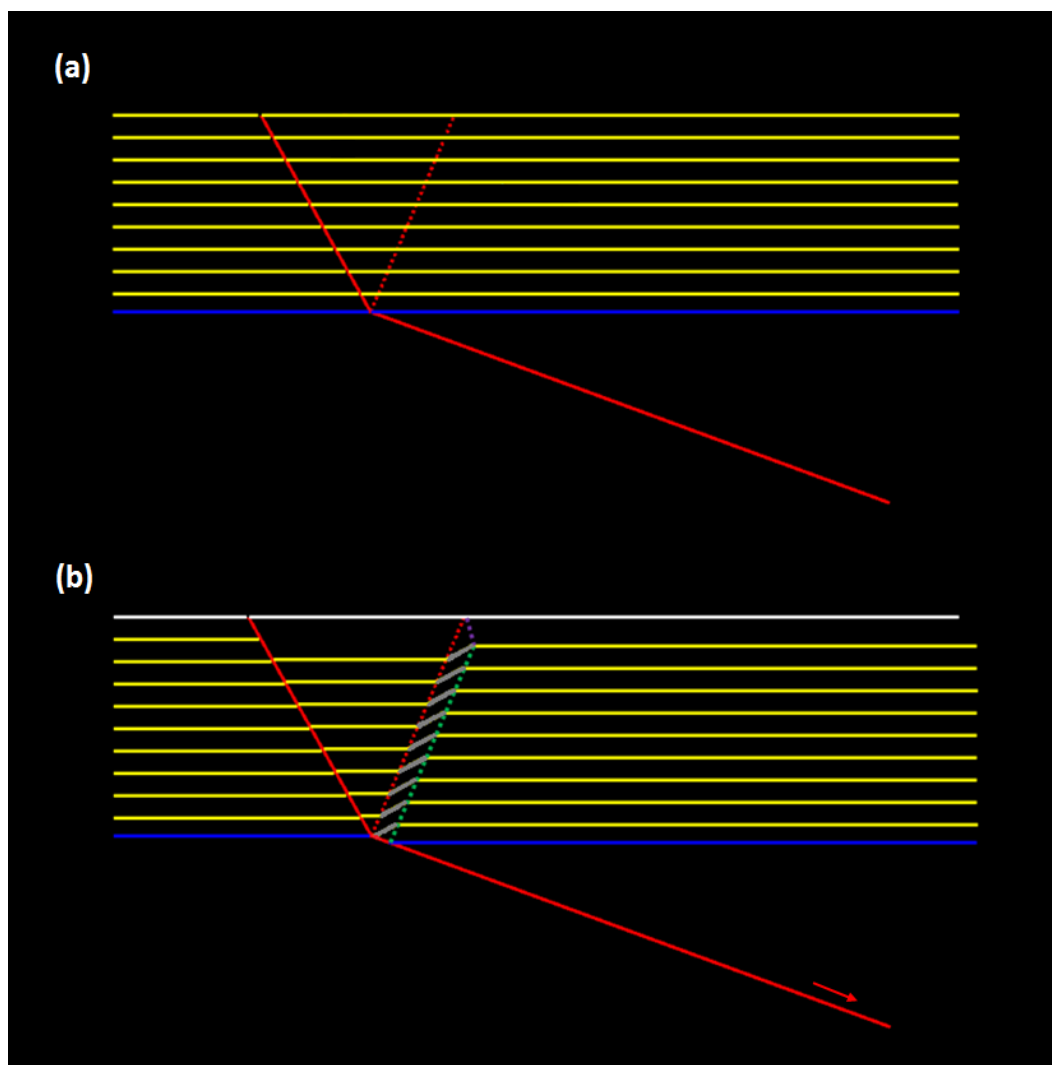

Figure 4-4: (a)-(d) Sequential stages of deformation of syntectonic deposition over a concave bend. White horizons indicate growth sediments. Grey lines indicate deformed hanging-wall beds within a kink band.

Figure 4-4: (continued)

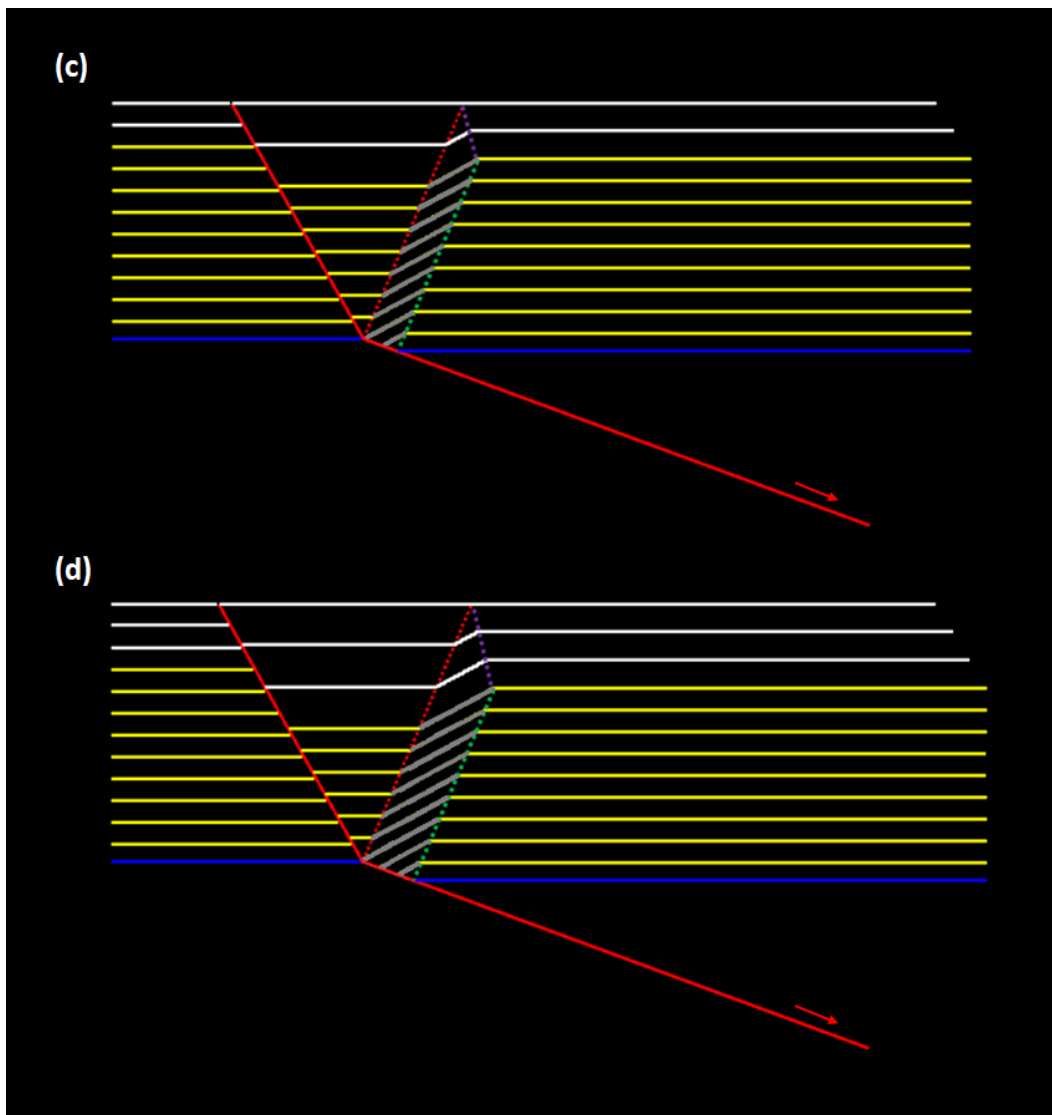### *4.3.5 Shear Angles*

Another factor affecting the deformation is the shear angles at which beds collapse. The

shear angle is the acute angle between the vertical and the inclined shear axis (White et al.,

1986). The collapse angle is determined from the dip of secondary faults. Figures 4-5 shows the

sensitivity of the deformed beds geometries to shear angles at a concave-upward fault bend. For

an antithetic shear axis, the model shows the dip of deformed hanging-wall beds decreases as the shear angle increases. In contrast, the dip of deformed hanging-wall beds increases as the shear angle increases for a synthetic shear axis.
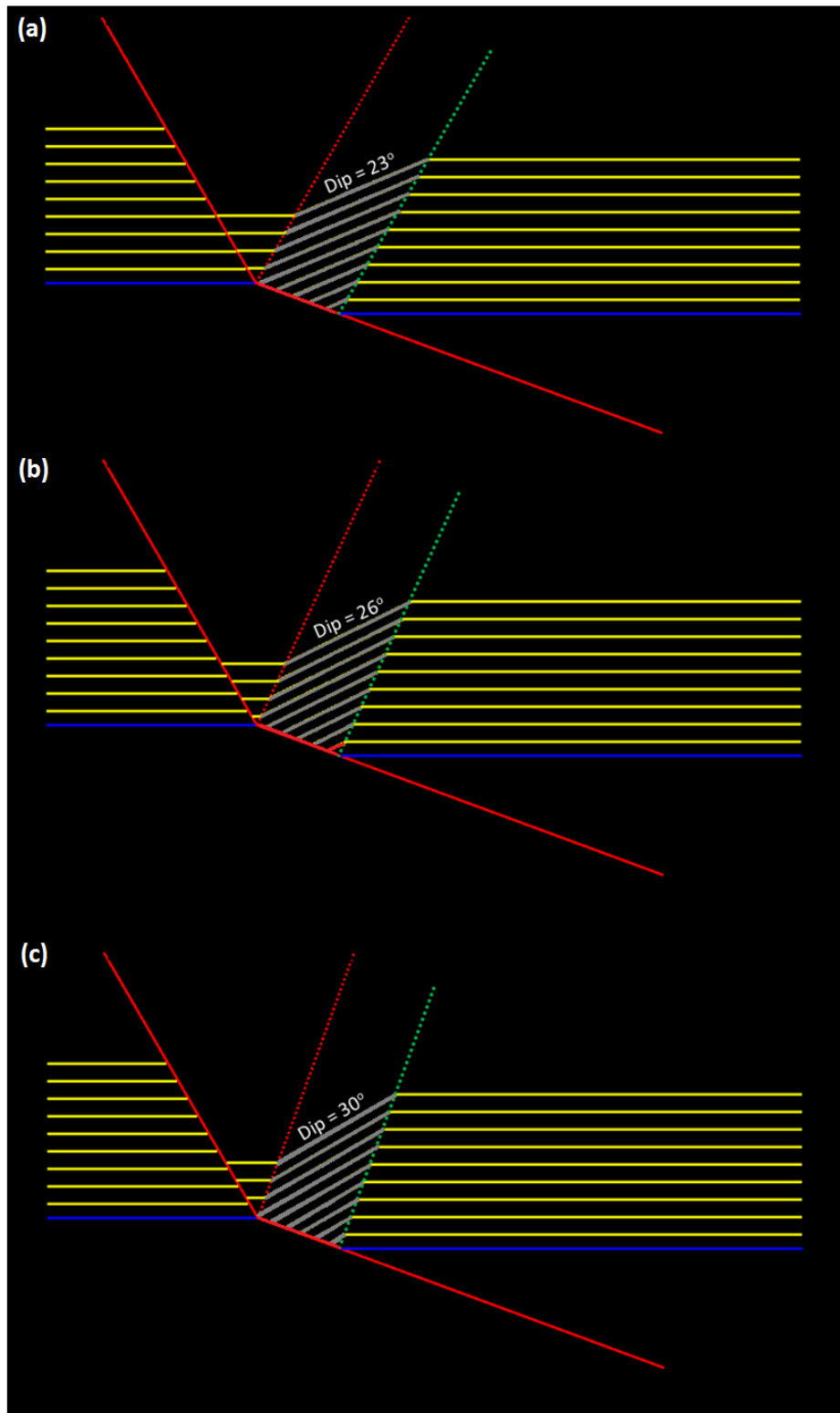
Figure 4-5: Sensitivity to changes in antithetic shear angles: a) 30º b) 25º c) 20º d) 15º e) 10º
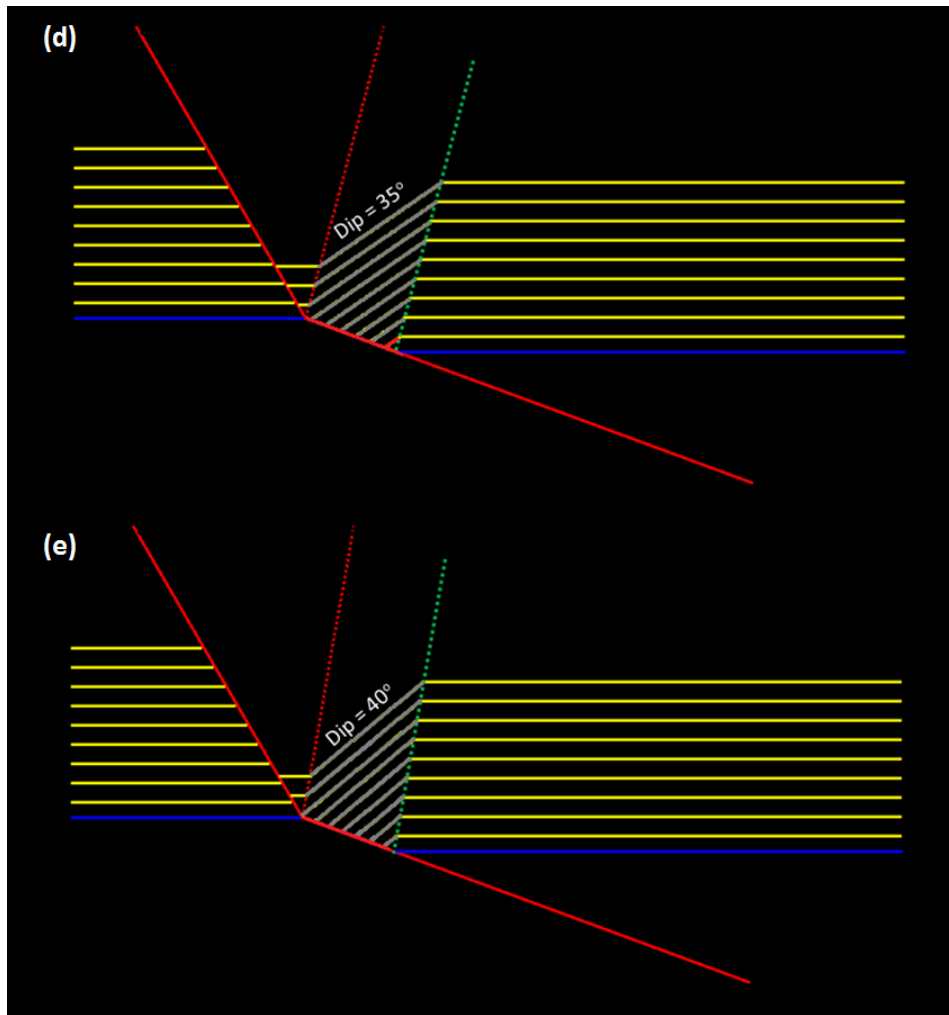
Figure 4-5: (continued)

Modeling based on the rollover geometry and Coulomb collapse concepts can be applied in two ways (e.g. Xiao and Suppe, 1992; Shaw et al., 1997; Groshong, 2006). The first method is when the fault shape is known, the rollover shape in the hanging wall can be predicted. The second method is when the rollover shape is known, the fault shape can be estimated at depth. The second method can be applied using seismic images by determining the hanging-wall and footwall cutoffs in an interpreted horizon along with the rollover shape from within that horizon.

In the next section, we use the second method to create kinematic forward models to predict the shape of Oaonui Fault at depth from seismic data.

4.4 Modeling Active Oaonui Fault Southwest Taranaki Peninsula

The concepts of extensional fault-bend folding, discussed in the previous sections, are very practical for assisting in seismic interpretation. We constructed kinematic forward models based on these concepts to solve for ambiguities in our seismic interpretation of the Oaonui Fault (as discussed in chapter 3). The models are used to predict the geometry of the fault in deeper poorly-imaged seismic reflections based on the hanging-wall rollover structures in the shallower well-imaged reflections.

We modeled the Oaonui Fault from vertical sections in the Te Kiri 3D seismic survey to investigate the fault's geometry at depth (below 2.4 seconds TWT). Structural interpretation of this survey showed north-east trending normal faults dominating the shallow reflections which can be easily observed by tracing alignments of amplitude terminations on time slices or converted depth slices. These observations of amplitude terminations indicate the geometry of the fault surface in the strike direction. Computed volumetric attributes (e.g. based on semblance and variance algorithms) were helpful in delineating the shallow fault surfaces in the survey, but not in the deeper poorly imaged seismic sections (Chapter 3).

The Oaonui Fault exhibits listric characteristics with its thickening hanging-wall blocks tilting toward the fault surface. The listric-like shape implies that the fault's dip continues to decrease gradually until it flattens out at depth. However, the exact fault shape is difficult to trace at deep reflections below about 2.6 seconds (TWT).

The Oaonui Fault was previously interpreted by Townsend et al. (2010) as one of the main active faults in Taranaki Peninsula. However, Townsend et al. (2010) does not show an interpretation of the fault's geometry below 3 seconds reflection TWT.

As explained in the previous sections, deformations are mostly the result of collapsing hanging-wall beds along active axial surfaces associated with the fault bends. We model the Oaonui fault by incorporating our interpretation of the fault bends along with the dip angles of active axial surfaces which are indicated by secondary faults.

Kinematic forward models based on seismic images must be constructed on sections parallel to the dominant dip direction. Therefore, we used vertical sections from Te Kiri 3D seismic survey that are perpendicular to the interpreted strike direction of the Oaonui Fault to construct the kinematic forward models in this study.

Figure 4-6a is a time migrated seismic section parallel to the dip of Oaonui Fault which is shown in red in the middle of the section. We model the Oaonui Fault based on knowledge of its shape at the well-imaged shallow reflections and horizon cutoffs at the fault surface. The interpreted horizons are of Early Pliocene (green) and Late Miocene (Blue) (Figure 4-6). The brighter green and blue horizons in Figure 4-6 indicate the interpreted horizons of the observed beds geometry in the seismic reflections in the section. Secondary antithetic and synthetic faults are observed in the hanging wall of the fault to indicate the dip domain and orientation of the active shear axial surfaces as well as the shear angles. The fault shape is therefore modeled by series of fault bends; concave-upward bends at deep terminations of antithetic faults and convex-upward bends at deep terminations of synthetic faults with the fault. Adjusting the shape of the modeled fault changes the geometry of the modeled hanging-wall beds (darker green and blue) . The modeled hanging-wall beds (darker green and blue) in Figure 4-6 are matched with the

interpreted seismic horizons (brighter green and blue) to validate the model and confirm the fault's shape.

We also modeled different scenarios for the fault geometry at the poor deep reflections in the section to verify our model-based seismic interpretation. One of the modeled scenarios is a listric shape that flattens out at shallower reflections above about 3.2 seconds (TWT). We examined each scenario by varying the fault shape at depth while trying to match the modeled hanging-wall horizons with the ones interpreted from the seismic sections (Figure 4-7). A mismatch between the modeled and observed horizons indicates an incorrect fault geometry.

4.5 Results and Discussion

The modeled geometry of Oaonui Fault adequately resembles the well-imaged seismic reflections of the interpreted shallow structure. The models suggest that the deformations in the hanging-wall structure were mainly controlled by movements along the underlying Oaonui Fault surface. The bends in Oaonui Fault were constructed to match the interpreted fault trace and. The fault trace below 3 seconds (TWT) is not clearly visible, and therefore the fault bends were inferred by secondary faults.

Some of the antithetic faults observed on the seismic section do not connect to their associated fault bends. Instead, these antithetic faults terminate downward at the position of a major synthetic fault associated with an active axial surface originating at a convex bend in the modeled fault. This case is observed in many growth faults (Tearpock and Bischke, 2002). Nevertheless, the dip domain of these antithetic faults can be used to construct concave bend for in the modeled fault. The dips of secondary faults observed on the seismic sections are generally

86

63-68 degrees indicating shear angles (i.e. Coulomb failure angle of about 22-27 degrees measured from the normal to horizontal beds.

The orientation of dipping beds in the seismic section indicates the type of fault bend at which deformation occurred. Deformation along an antithetic active axial surface is associated with slip over a concave-upward fault bend, resulting in beds dipping toward the modeled fault surface. Conversely, deformation along a synthetic active axial surface is associated with a convex-upward fault bend, causing beds to dip away from the modeled fault surface (i.e. in the same dip direction as the modeled fault). Moreover, some of the deformed hanging-wall beds may have passed through both antithetic and synthetic active axial surfaces resulting in an apparent undeformed horizontal orientation.

The model shows a ramp-and-flat geometry of the Oaonui Fault which offsets the basement at depth of about 6 km (about 3.3 seconds TWT).

We modeled different shapes for the Oaonui Fault at depth to validate our interpretation. One of the examined scenarios is that flattens out above the basement. This model shows a mismatch between the modeled shallow horizons (dark green and blue) and interpreted horizons (brighter green and blue) in the seismic section. We therefore conclude this geometry to be invalid for the interpreted fault.

The structural orientations of the fault and hanging-wall blocks appear to be consistent throughout the 3D seismic survey. We modeled consecutive normal-to-strike lines to map the surface of the fault.

Deformation in the subsurface is affected by different variables, including the fault shape and its total slip, sedimentation rate relative to the slip, and the direction of hanging-wall collapse along shear axes, and compaction. Our models consider all these variables except for

compaction. Although compaction can alter the fault shape and its associated hanging-wall deformation, Xiao and Suppe (1992) concluded that except for uncommon conditions, the effect of compaction can be neglected when modeling in the compacted state (i.e. seismic sections).
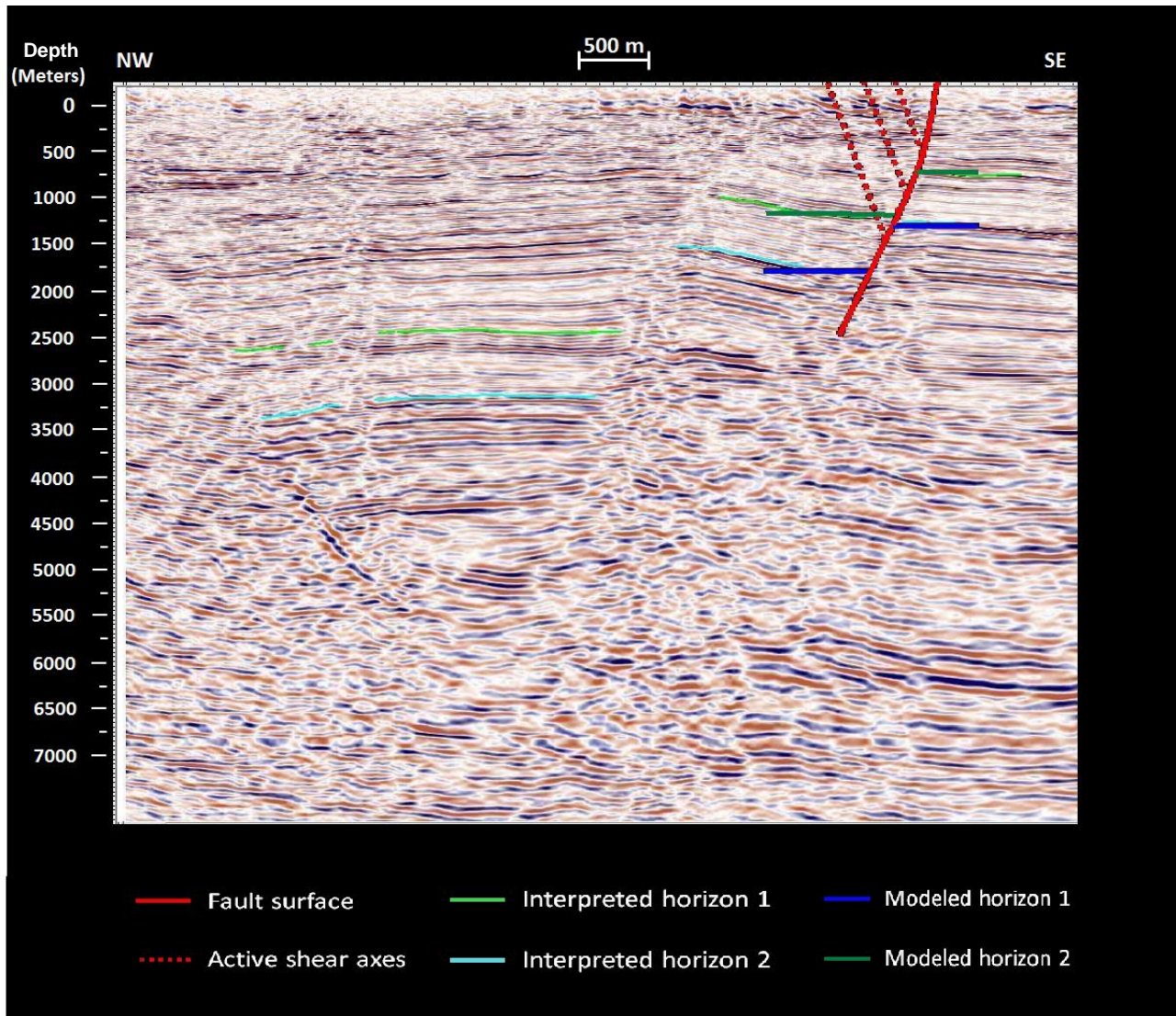

Figure 4-6: Kinematic forward modeling for fault prediction on a depth converted seismic section. Light green and blue are interpreted seismic horizons. Dark green and blue are modeled horizons. The interpreted major fault shape is shown in red (solid line). The dashed red lines indicate the dip domain of secondary faults at fault bends
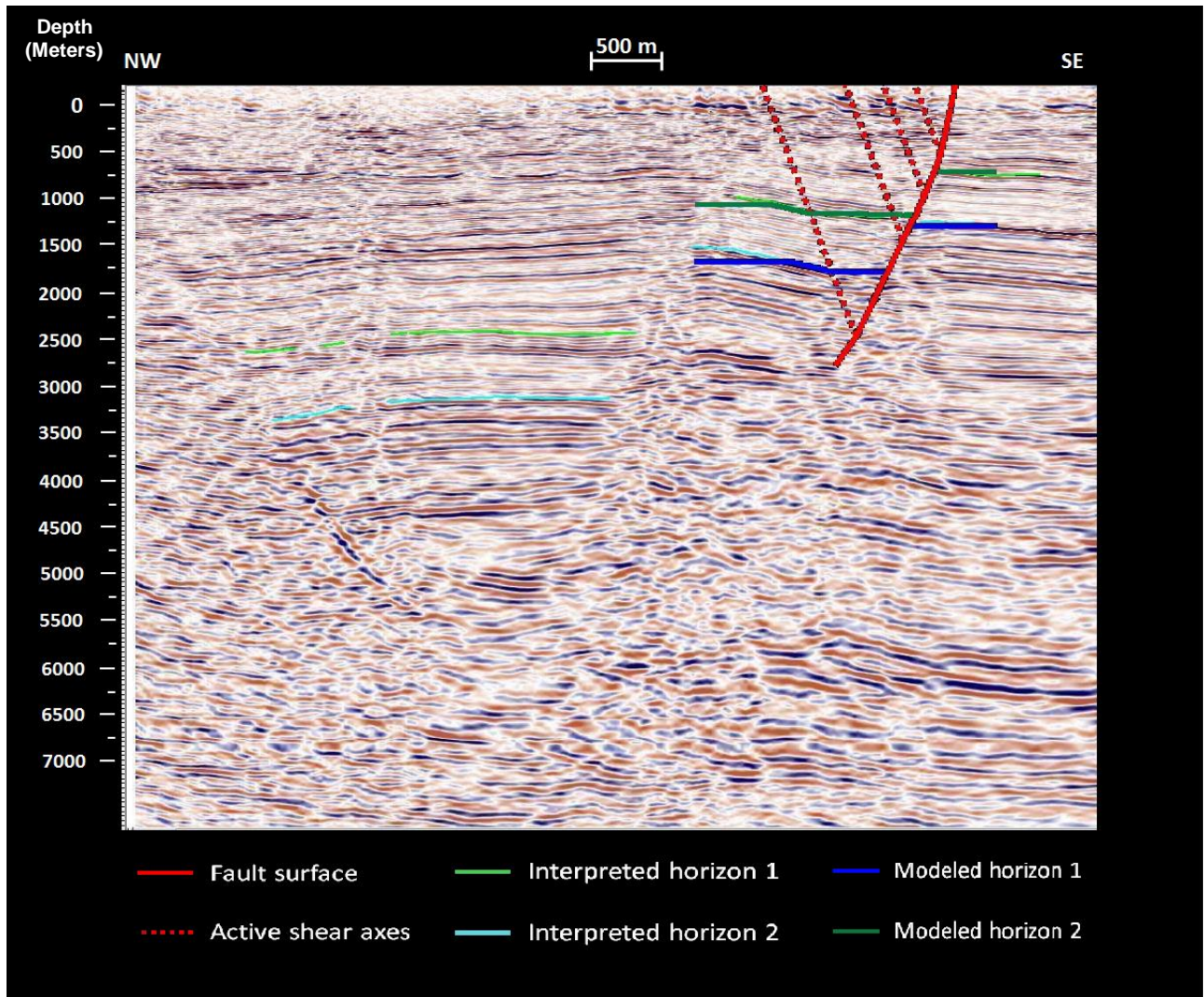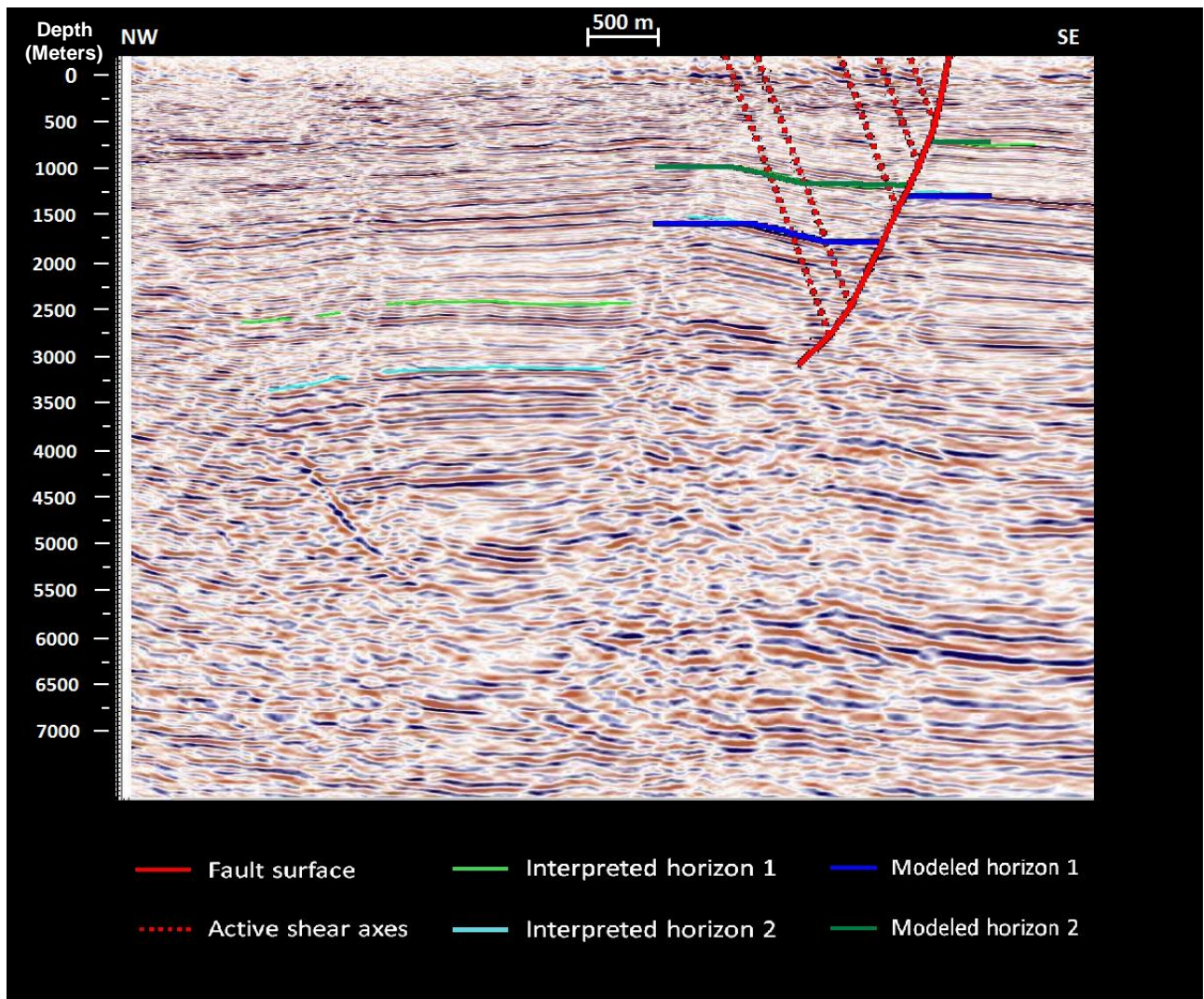
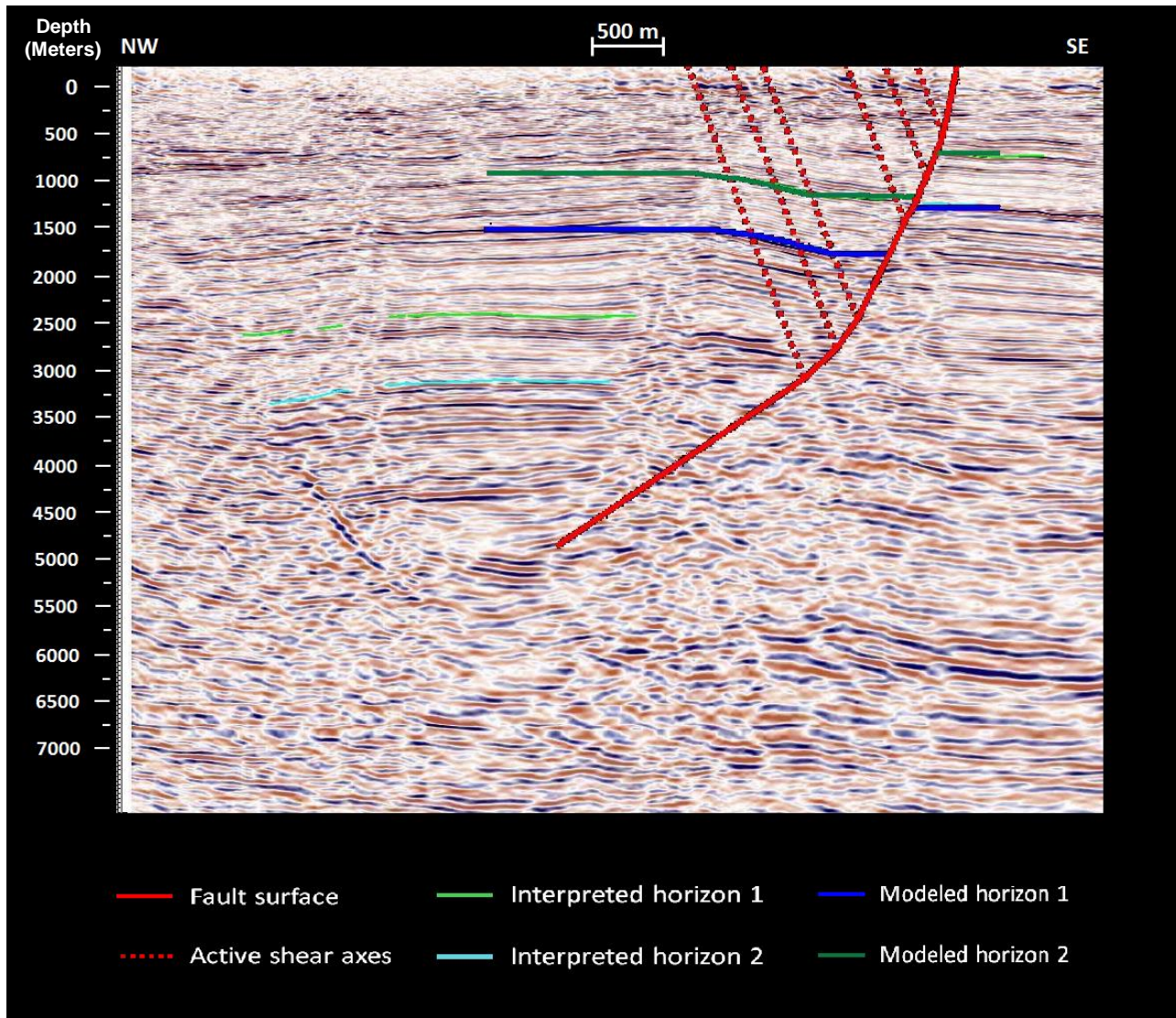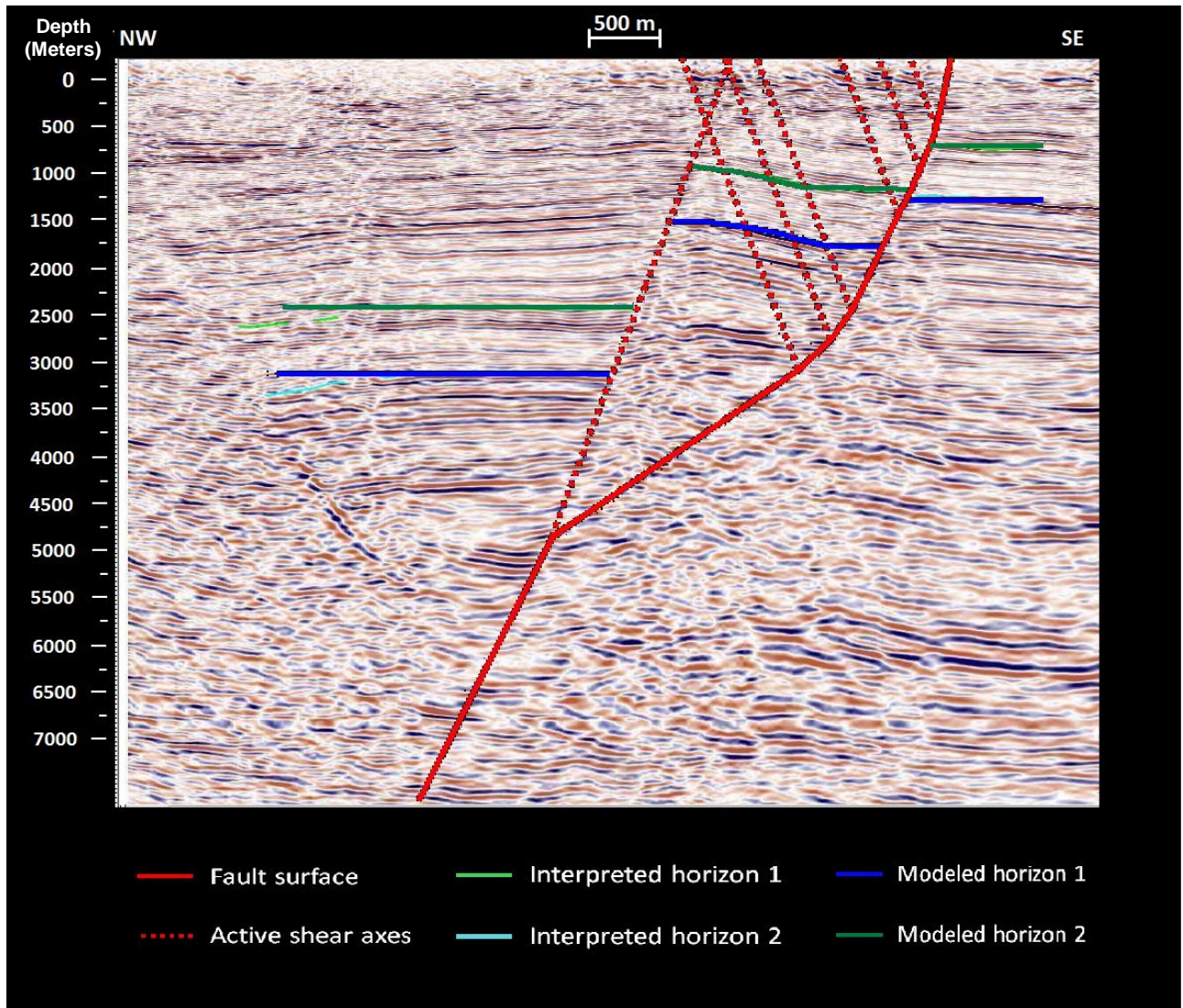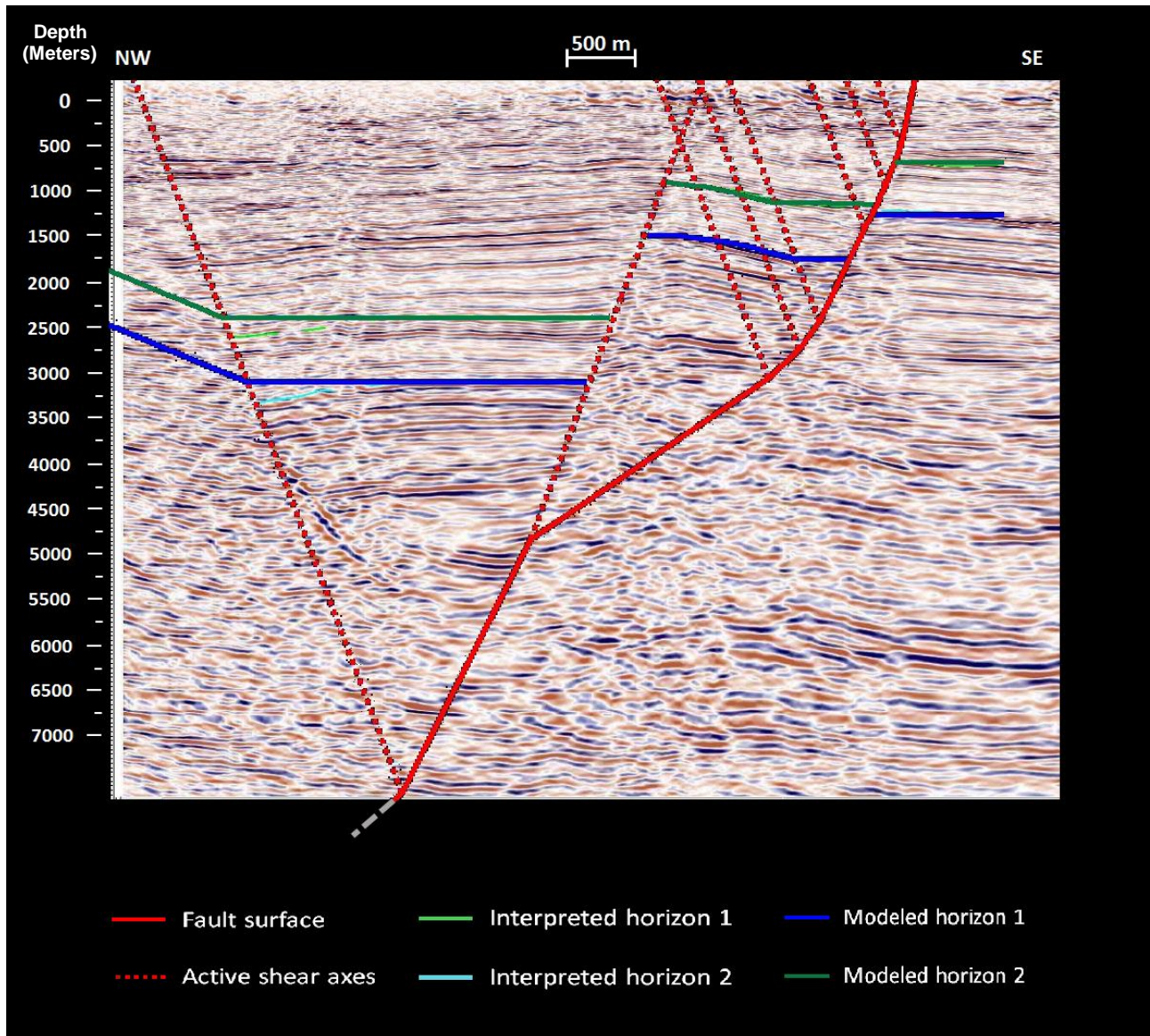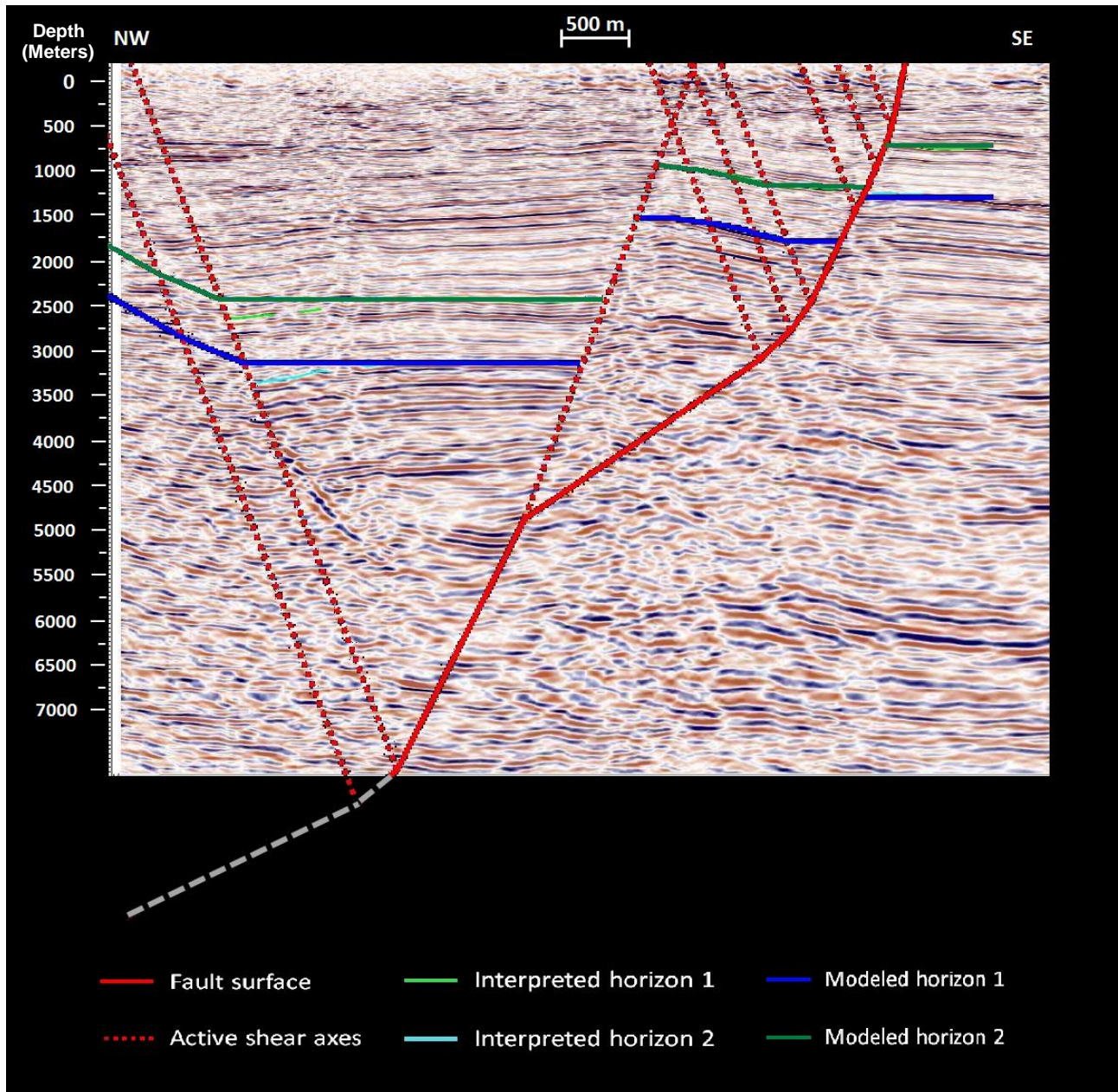**Figure 4-6: (continued)**

Figure 4-6: (continued)

Figure 4-6: (continued)

Figure 4-6: (continued)

Figure 4-6: (continued)

Figure 4-6: (continued)
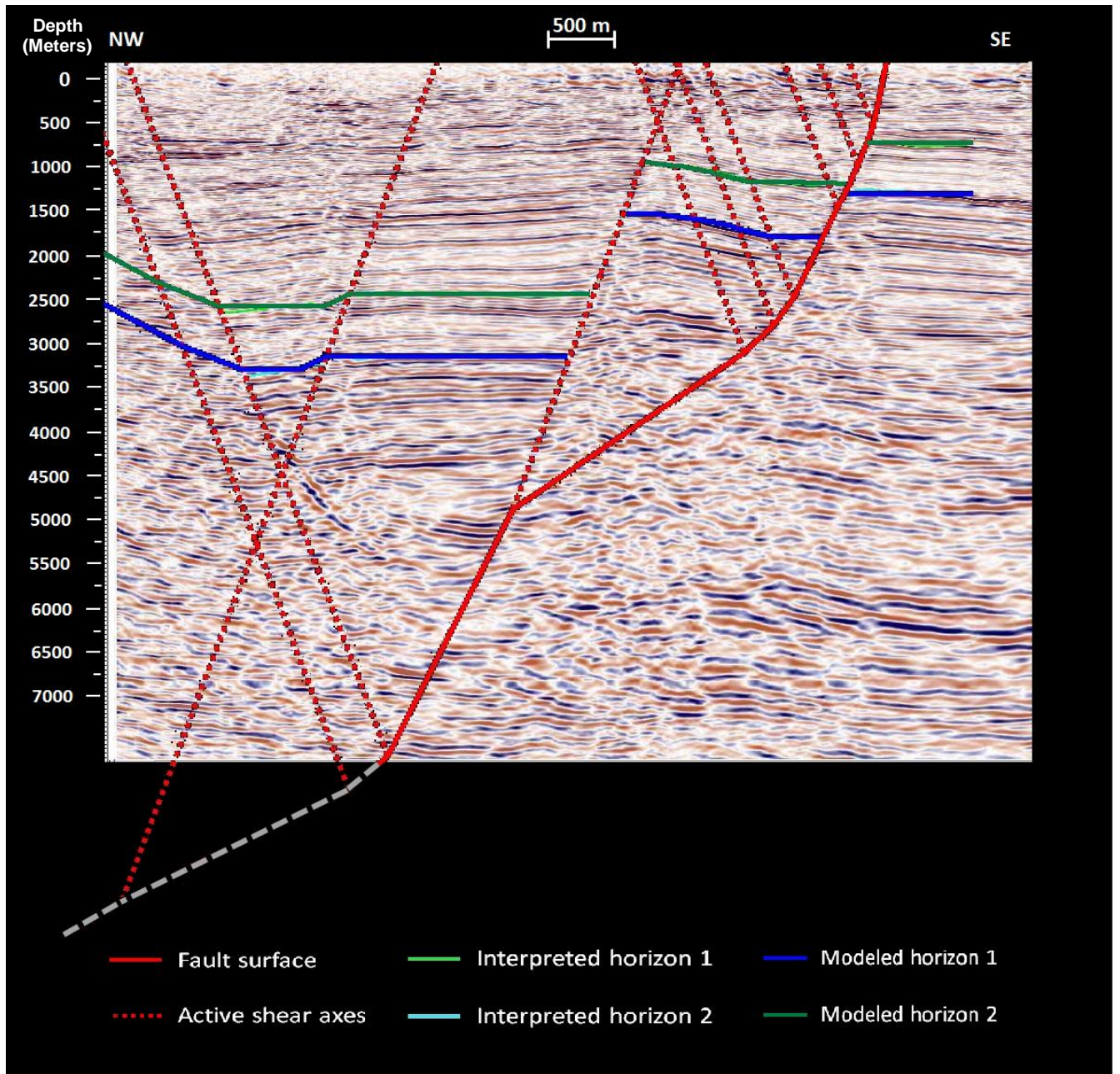
Figure 4-6: (continued)
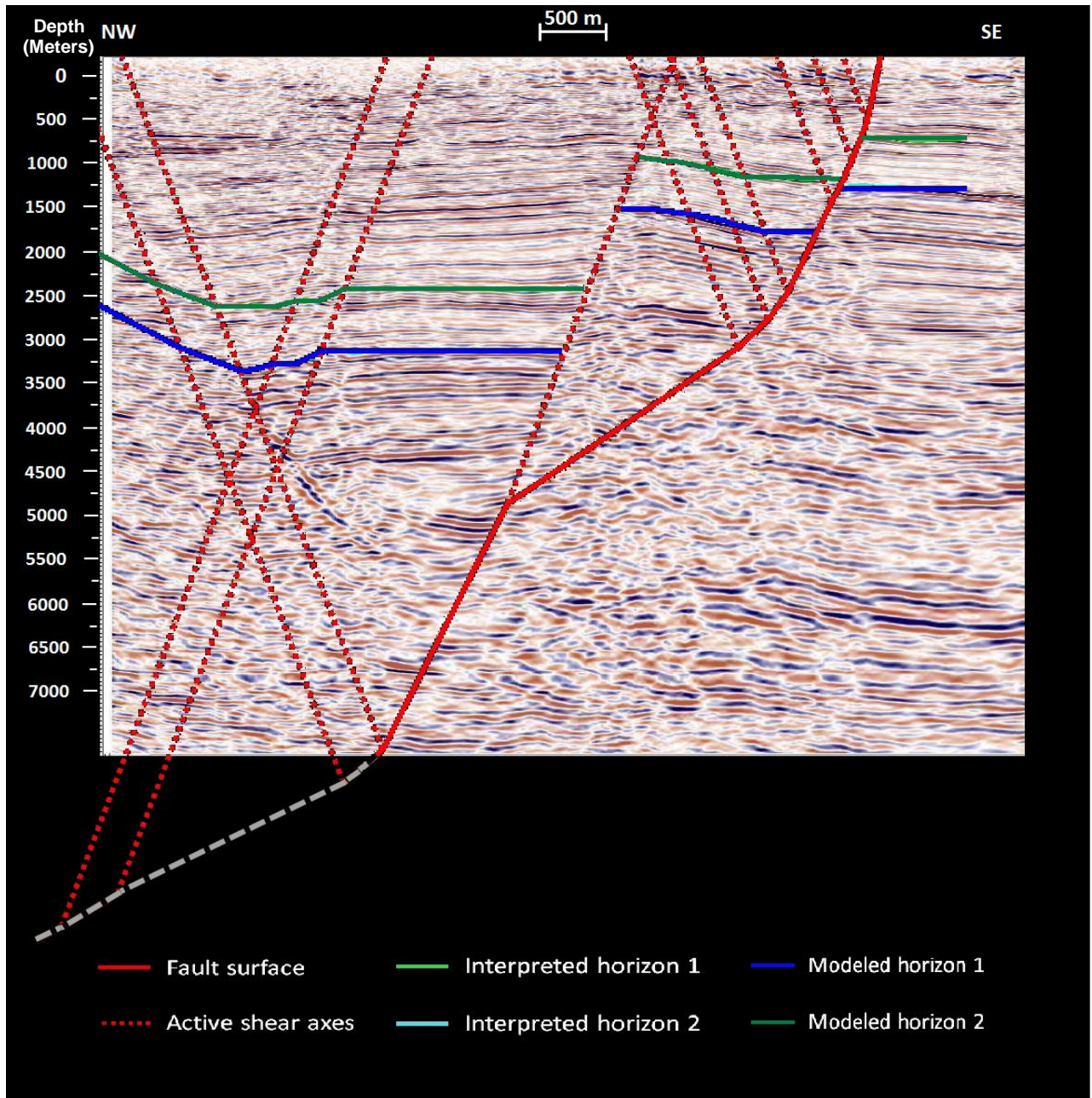
Figure 4-6: (continued)
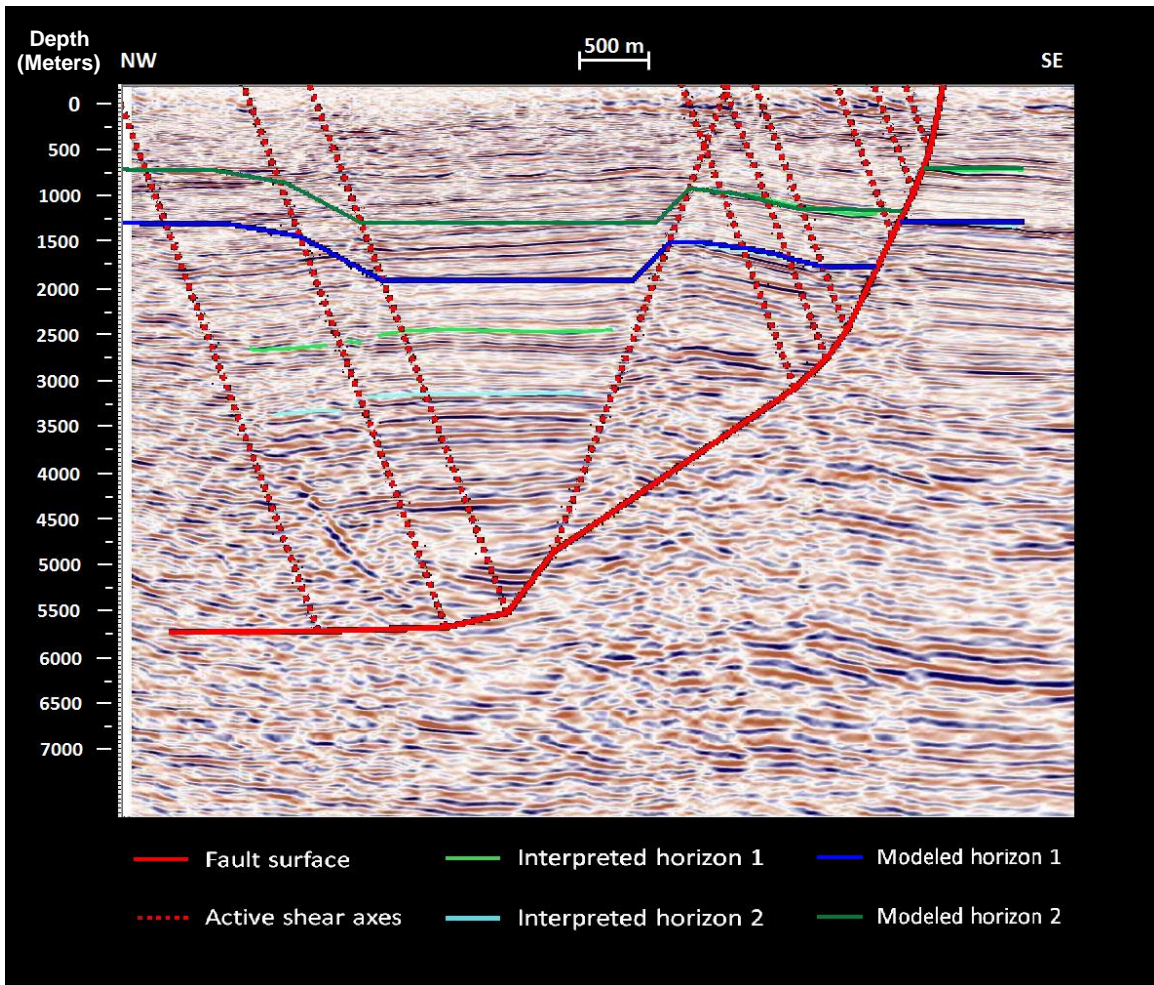
Figure 4-7: Incorrect model showing deformation caused by a listric fault

4.6 Summary and Conclusions

Kinematic forward models using inclined-shear method can describe the unique relationship between fault shape and hanging-wall deformation during extension. We modeled rollover geometries with different fault bends, sedimentation and slip ratios, and shear angles. Our kinematic forward models were constructed to predict the Oaonui Fault deep shape from our interpretation of Te Kiri 3D seismic survey in the Taranaki Basin, where the fault is not easily

interpretable at depth. The model suggests that the structure of the Oaonui Fault is a ramp-and-

flat geometry which cuts through the basement at depth of about 6 km (about 3.3 seconds TWT).

Chapter Five: Conclusions

In this thesis, a major fault that is considered to be active in Taranaki Peninsula was studied from a 3D seismic reflection volume. Seismic images from the 3D volume reveal the complex subsurface structure which relates to the tectonic activities and deformation history in the region since the mid-Cretaceous. North- to north-east trending faults are clearly imaged by the shallow reflections in the volume. The resolution and quality of the seismic images deteriorate with depth where faults geometries are not clearly visible.

This thesis also addresses observations of amplitude anomalies and incoherent reflections within vertical zones along normal faults. The anomalies observed in the seismic images are likely to be the result of gas migrating upsequence along permeable normal faults. This conclusion is supported be similar observations of gas leakage in nearby gas fields in the basin. Seismic attribute analysis can detect the gas presence and delineate the gas distribution in the survey. Knowledge of geologic history of the region along with the lack of flower structures in the interpreted seismic volume indicate that deformations associated with faults are mainly due to dip-slip rather than strike-slip movements. Therefore, the loss of seismic image across faults' cutoffs, is the result of gas presence rather than distributed strain caused by strike-slip movement.

In order to evaluate the gas presence and its origin along faults, it is necessary to understand the geometry of faults at depth and whether they are in contact with the proven reservoir in the region. In this thesis, the geometry of the major fault in the seismic volume was modeled using kinematic forward models that are based on the inclined-shear method. The models predicted the fault's deep shape based on the shape of deformation in the fault's hanging

wall. This thesis concludes, based on the constructed models, that the major fault in the survey is

a ramp-and-flat geometry which cuts through the basement at about 6 km depth.

References

Al-Dossary, S. and K. J. Marfurt, 2006, 3D volumetric multispectral estimates of reflector curvature and rotation: Geophysics, 71, P41–51.

Alshuhail, A. A., Lawton, D. C., and Chabot, L., 2008, Pembina Cardium CO2 monitoring project: timelapse seismic analysis: CREWES Research Report, 20.

Anderson, A. L., and L. D. Hampton, 1980a, Acoustics of gas-bearing sediments: 1. Background: Journal of the Acoustical Society of America, 67, 1865–1889.

Bjørkum, P. A., Walderhaug, O. and Nadeau, P. H., 1998, Physical constraints on hydrocarbon leakage and trapping revisited: EAGE Petroleum Geoscience, 4, 237-239.

Brown, A. R., 2011, Interpretation of Three-Dimension Seismic Data: The American Association of Petroleum Geologists and the Society of Exploration Geophysicists.

Chopra, S., and Marfurt, K. J., 2007, Seismic attributes for prospect identification and reservoir characterization: Society of Exploration Geophysicists, Tulsa, OK.

Cloos, E., 1968, Experimental analysis of Gulf Coast fracture patterns: AAPG Bulletin, v. 52, 420-444.

Gibbs, A. D., 1983, Balanced cross-section construction from seismic sections in areas of extensional tectonics: Journal of Structural Geology, v. 5, p. 1-39.

Davis, G. H., Reynolds, S. J., and Charles F. K., 2012, Structural Geology of Rocks and Regions: John Wiley & Sons, Inc., Hoboken, NJ.

Dissen, V. R., Barrell, D., Litchfield, N., Villamor, P., Quigley, M., King, A., Furlong, K., Begg, J., Townsend, D., Mackenzie, H., Stahl, T., Noble, D., Duffy, B., Bilderback, E., Claridge, J., Klahn, A., Jongens, R., Cox, S., Langridge, R., Ries, W., Dhakal, R., Smith, A., Horblow, S., Nicol, R., Pedley, K., Henham, H., Hunter, R., Zajac, A., Mote, T., 2011, Surface rupture displacement on the Greendale Fault during the Mw 7.1 Darfield (Canterbury) earthquake, New Zealand, and its impact on man-made structures, Auckland, New Zealand: Ninth Pacific Conference on Earthquake Engineering: Building an Earthquake-Resilient Society, 14-16 Apr 2011.

Dula Jr, W. F., 1991, Geometric Models of Listric Normal Faults and Rollover Folds (1); AAPG Bulletin, 75(10), 1609-1625.

Fossen, H., 2010, Structural geology: Cambridge University Press, Cambridge, U.K.

Gibbs, A. D., 1983, Balanced cross-section construction from seismic sections in areas of extensional tectonics: Journal of Structural Geology, v. 5, p. 1-39.

Hale, D., 2013, Methods to compute fault images, extract fault surfaces, and estimate fault throws from 3D seismic images: Geophysics, v. 78, No. 2, O33-O43.

Herron, D. A., 2011, First steps in seismic interpretation: Geophysical monograph series, no. 16.

Herron, D. A., 2000, Pitfalls in seismic interpretation: Depth migration artifacts: The Leading Edge, v. 19, No. 9, 1016-1017.

Løseth, H., M. Gading, and L. Wensaas, 2009, Hydrocarbon leakage interpreted on seismic data: Marine and Petroleum Geology, v. 26, no. 7, 1304–1319.

King, P.R. 1991. Physiographic maps of the Taranaki Basin - Late Cretaceous to Recent. New Zealand Geological Survey Report G155.

King, P.R., Naish, T.R., Thrasher, G.P. 1991. Structural cross sections and selected palinspastic reconstructions of the Taranaki Basin, New Zealand. New Zealand Geological Survey report G150.

King, P. R., and Thrasher, G. P., 1996, Cretaceous Cenozoic geology and petroleum systems of the Taranaki Basin, New Zealand (Vol. 2). Institute of Geological & Nuclear Sciences.

Lindsey, J. P., 1989, The Fresnel zone and its interpretive significance: The Leading Edge, 10, 33–39.

Lawton, D. C., Bertram, M. B., Hall, K. W., Bertram, K. L., and Pettinga, J., 2013, Imaging Unknown Faults in Christchurch, New Zealand, after a M6. 2 Earthquake. In 75th EAGE Conference & Exhibition incorporating SPE EUROPEC 2013.

Lawton, D. C., Bertram M. B., Margrave, G. F. and Gallant, E. V., 2006, Comparisons between data recorded by several 3-component coil geophones and a MEMS sensor at the Violet Grove monitor seismic survey: CREWES Research Report, 18.

Lines, L. R., and Newrick, R. T., 2004, Fundamentals of geophysical interpretation: Society of Exploration Geophysicists, Tulsa, OK.

Marfurt, K., R. Kirlin, S. Farmer, and M. Bahorich, 1998, 3-D seismic attributes using a semblance-based coherency algorithm: Geophysics, 63, 1150–1165.

Mavko, G., Mukerji, T., and Dvorkin, J., 2003, The Rock Physics Handbook, 51 p. Cambridge University Press, Cambridge, U.K.

McClay, K. R., & Ellis, P. G., 1987, Geometries of extensional fault systems developed in model experiments; Geology, 15(4), 341-344.

Meldahl, P., R. Heggland, B. Bril, and P. de Groot, 2001, Identifying faults and gas chimneys using multiattributes and neural networks: Leading Edge, v. 20, no. 5, p. 474–482

Mouslopoulou, V., Nicol, A., Walsh, J. J., Begg, J. G., Townsend, D. B., & Hristopulos, D. T. , 2012, Fault-slip accumulation in an active rift over thousands to millions of years and the importance of paleoearthquake sampling: Journal of Structural Geology, 36, 71-80.

Nodder, S. D., 1993, Neotectonics of the offshore Cape Egmont fault zone, Taranaki basin, New Zealand: New Zealand Journal of Geology and Geophysics, 36(2), 167-184.

Nunns, A. G., 1991, Structural Restoration of Seismic and Geologic Sections in Extensional Regimes (1); AAPG Bulletin, 75(2), 278-297.

NZP&M, 2013, New Zealand Petroleum Basins: New Zealand Petroleum & Minerals.

Sheriff, R., 1980, Nomogram for Fresnel zone calculation: Geophysics, 45, 968– 972.

Sheriff, R. E., 2002, Encyclopedic dictionary of exploration geophysics, 4th ed.: SEG Geophysical Reference Series no. 1.

Suggate, R.P., Stevens, G.R., Te Punga, M.T. (eds), 1978, The geology of New Zealand:New Zealand Geological Survey, Department of Scientific and Industrial Research, Wellington.

Thrasher, G. P., 1990b, Tectonics of the Taranaki Rift. In 1989 New Zealand Oil Exploration Conference proceedings: 124–133. Ministry of Commerce, Wellington.

Thrasher, G.P. 1990b. Tectonics of the Taranaki Rift. In 1989 New Zealand Oil Exploration Conference proceedings: 124–133. Ministry of Commerce, Wellington.

Townsend, D., Nicol, A., Mouslopoulou, V., Begg, J. G., Beetham, R. D., Clark, D., ... & Walsh, J. J. (2010). Palaeoearthquake histories across a normal fault system in the southwest Taranaki Peninsula, New Zealand. New Zealand Journal of Geology and Geophysics, 53(4), 375-394.

Quigley, M., P. Villamor, K. Furlong, J. Beavan, R. Van Dissen, N. Litchfield, T. Stahl, B. Duffy, E. Bilderback, D. Noble, D. Barrell, R. Jongens, and S. Cox, 2010, Previously unknown fault shakes New Zealand's South Island: EOS Transactions, AGU, 91, 469–471.

Shaw, J. H., Hook, S. C., & Sitohang, E. P., 1997, Extensional fault-bend folding and synrift deposition: An example from the Central Sumatra Basin; Indonesia. AAPG bulletin, 81, 367-379.

Spang, J. H., & Dorobek, S. L., 1998, Using Antithetic Normal Faults to Map Growth Axial Surfaces.

Taner, M. T. , 2001, Seismic Attributes: CSEG Recorder, 48-56.

Taner, M. T., 2002, System for estimating the locations of shaley subsurface formations., U.S. Patent No. 6,487,502. 2

Voggenreiter, W.R. 1993. Structure and evolution of the Kapuni Anticline, Taranaki Basin, New Zealand: evidence from the Kapuni 3D seismic survey. New Zealand journal of geology and geophysics 36: 77–94.

White, N. J., Jackson, J. A., and Mckenzie, D. P., 1986, The relationship between the geometry of normal faults and that of the sedmentary layers in their hanging walls: Journal of Structure

Geology, 8(8), 897-909.

Widess, M. B., 1973, How thin is a thin bed?: Geophysics, 38(6), 1176-1180.

Xiao, H., & Suppe, J., 1992, Origin of Rollover (1): AAPG Bulletin, 76(4), 509-529.

Yilmaz, Öz, 2001, Seismic data analysis: Society of Exploration Geophysicists, Tulsa.